Università degli Studi di Napoli *Federico II*

Università di Camerino

Consiglio Nazionale delle Ricerche

DOTTORATO DI RICERCA IN QUANTUM TECHNOLOGIES

Ciclo XXXIV

Coordinatore: prof. Francesco Tafuri

Transport and proximity effect in ferromagnetic insulator Josephson junctions: a lattice Green's function approach

Settore Scientifico Disciplinare FIS/03

Dottorando
Martina Minutillo

Tutore
Dott. Procolo Lucignano

Anni 2018/2021

Contents

Introduction

In nature, generally, we can recognize two possible levels at which a physical phenomenon can manifest itself: firstly, at the macroscopic scale, where the observer's eye can more or less directly perceive it, and secondly from a microscopic point of view. This second level, although much more challenging to deal with, provides the elements to describe the mechanisms underlying macroscopic phenomena. Superconductivity and ferromagnetism are both examples of phenomena where the macroscopic behavior is a clear manifestation of the quantum mechanical nature of the state characterizing the system. They both correspond to ordered phases with a spontaneously broken symmetry, however there is a fundamental difference between these two states. Indeed, while according to the Bardeen, Cooper, and Schrieffer (BCS) model [1–3] the usual singlet superconductivity favors the arrangement of electrons in Cooper pairs with opposite spins, the ferromagnetic exchange field tends to align the spins of the pairs, thus destroying the latter. These competing mechanisms lead to the so-called *paramagnetic* pair breaking effect [4–12].
After the advent of the BCS theory in 1957 it became evident that, due to their conflicting nature, the interplay between superconductivity and ferromagnetism could hardly be observed in bulk systems. However, the study of hybrid structures consisting of superconducting and non-superconducting elements in contact with each other, started a few years later [13,14], provided the evidence that a sort of coexistence of these two primary macroscopic quantum phenomena may be realized in layered superconductor/ferromagnet (S/F) structures [15–19]. In this context, it was immediately evident that the interplay between these two quantum processes could have paved the way for the study of a series of new physical phenomena until then considered quite exotic.
Recently, the growing appeal in quantum technologies and their employment for the realization of new innovative devices, has renovated the interest in the so called *proximity effect* arising at interfaces between superconducting and normal materials characterizing such heterostructures and in the coherence mechanisms occurring on a mesoscopic scale, which have been theoretically and experimentally more extensively studied [15, 17, 19–25].
Proximitized S/F systems, which allow to artificially reproduce the coexis-

tence of superconductivity and ferromagnetism, offer a unique opportunity to study and analyze the effects of their interplay. The exchange field, inducing pair breaking for the Cooper pairs, produces additional oscillations of the superconducting order parameter induced in the F region, in analogy with the so-called FFLO state [26, 27]. Among the consequences of the presence of the magnetization at the interface of the superconductor we can mention that the Josephson effect in SFS junctions is modified and can exhibit two different states, denoted as 0 and π [15,17,19,28], depending on the thickness (length) of the ferromagnetic barrier and on the magnitude of the exchange field [29–35]. Interest in such an effect began to grow when it was shown that these peculiar features may be exploited to design superconducting circuits and quantum computing devices [36–40].

Furthermore, the observation of interaction between conventional superconductivity and ferromagnetism in S/F heterostructures led to another key discovery: the existence of unconventional superconducting correlations in a triplet state [15, 17, 19, 41–43]. In particular, it has been shown that if the exchange field is homogeneous, the superconducting condensate consists of only two components: the usual singlet one $(|\uparrow\downarrow - \downarrow\uparrow\rangle)$ and the triplet component $(|\uparrow\downarrow + \downarrow\uparrow\rangle)$ with total zero spin projection with respect to the magnetization axis of the F layer [15, 19]. However, these superconducting correlations are short-ranged because, due to the paramagnetic pair-breaking effect, the exchange field tends to align the spins of Cooper pairs, thus destroying them. This implies that the Cooper pairs can survive in the ferromagnet only within a small region close to the interface. Thus, for obvious reasons, this short-range proximity effect results to be not particularly appealing for the development of applications.

Nevertheless, the scenario described above is only part of the story because, under particular conditions, it is possible to observe the formation of spin-triplet long-range pairing correlations. These latter, are no longer affected by the exchange-energy breaking and can survive longer inside the ferromagnet, since the singlet Cooper pairs can be converted into the triplet state in which the spins are aligned parallel, namely $|\uparrow\uparrow\rangle$ or $|\downarrow\downarrow\rangle$. Specifically, it is now known that these equal spin-triplet correlations are triggered by the presence of inhomogeneous magnetization or spin-mixing effects occurring at interfaces [21, 44–47]. The theoretical prediction of this long-range proximity effect was subsequently also accompanied by experimental confirmations from various groups [48–55]. The main purpose of the research in this field is the creation and control of such long-range superconducting triplet correlations in hybrid structures with the ultimate goal of using polarized spin supercurrents for the development of new types of devices that combine the features of superconductivity and spintronics. Therefore, the comprehension of the physics that underpins the triplet generation process is of fundamental interest.

Motivation and outline of the thesis

Although the special features of SFS junctions have been extensively studied [15, 17, 19, 47, 56, 57], much less is known when the ferromagnetic layer is insulating. This strongly motivated us to focus on these kinds of systems, presenting, in this thesis, an analysis of the proximity effect and transport phenomena occurring in ferromagnetic insulator Josephson junctions (SFIS JJs). One remarkable feature to consider is that, even if SFIS junctions have similar properties to SFS systems, they exhibit a reduced quasiparticle current, which is responsible for the intrinsic dissipation due to the coupling with the environment [58, 59], affecting the dynamic properties of the junction and representing one of the drawbacks of SFS JJs based devices. On the contrary, due to the insulating nature of the ferromagnetic barrier, SFIS JJs exhibit longer decoherence times when implemented in quantum circuits, placing such systems in an interesting perspective for the realization of low-dissipative devices [60–65].
These advantageous features explain the growing strong interest in SFIS junctions, giving rise to several theoretical and experimental studies conducted on these systems [62, 63, 66–69].
In this work, we examine an unconventional kind of proximity effect due to the interplay between superconductivity and the combined presence of the exchange field, spin-orbit coupling (SOC), and nonmagnetic impurities in the FI barrier. The analysis of such systems requires a clear understanding of mechanisms underlying the modifications of the superconducting state properties near the S/FI interface, offering a rich scenario of phenomena that make these devices both experimentally and theoretically very attractive.
As of today, JJs constitute one of the elementary building blocks in quantum electronics field; conventional (non-ferromagnetic) JJs are able to carry a dissipationless current $I(\phi) = I_c \sin\phi$, which is defined by the critical current I_c and the phase difference ϕ between the wave functions describing the superconducting electrodes [70, 71]. These are called 0 JJs, since here the ground state occurs at $\phi = 0$, for $I_c > 0$. When the barrier is a ferromagnet, the current-phase relation may be shifted by π to $I\,(\phi) = |I_c| \sin\,(\phi + \pi) = -|I_c| \sin\,(\phi)$ [15, 17, 19, 28]. These junctions, to which corresponds a negative critical current $I_c < 0$, are called π junctions.
In particular, for applications, there is a strong demand for the π junctions, which are considered to be very promising ingredients to engineer spintronics and quantum computing devices.
As an example, phase controllable 0-π junctions have immediate applications in cryogenic memory [72–75], opening up new possibilities for superconducting circuit elements. Furthermore, there are other possible implementations that benefit from the use of fixed-phase π JJs [64, 76, 77], as their integration in quantum circuits for the realization of superconducting qubits, quite promising in view of the increased robustness against noise and electromag-

netic interference induced by magnetic field sources and a more compact and simple design, opening the way to scalable devices [39, 40, 78–81].
Mindful of these encouraging perspectives, various works demonstrated the possibility of realizing π junctions also in SFIS JJs [69, 82], getting the benefits deriving from the insulating regime of the ferromagnetic barrier.
It is in this promising scenario offered by π JJs that the first part of the work developed in this thesis is placed. We present, in fact, a theoretical study focused on the search for possible alternative ways to control the realization and switching of 0 and π states in SFIS JJs. In particular, here we show that the state of a SFIS JJ can be toggled between 0 and π by using SOC and nonmagnetic impurities as driving elements to switch between these two phases. The main strength of our procedure consists in the possibility of controlling the occurrence of 0-π transitions in SFIS JJs, through a direct action on the thermal behavior of the critical current, $I_c(T)$, rather than resorting to traditional and well-known ways, such as the tuning of the exchange field of the barrier to drive the 0-π switching [68], that requires experimental procedures not so easily manageable.
Secondly, in this work, we focus on another peculiar characteristic, which allows us to analyze the singular properties of these systems from a different point of viewing: we examine the presence and possible coexistence of spin-singlet and triplet pairing correlations induced in the FI barrier. This second theme is becoming especially relevant since the recent experimental achievements on NbN/GdN/NbN JJs, in which evidence of spin-triplet transport has been reported [57, 67, 83, 84]. The valuable property of this triplet component of the superconducting condensate is that it may create highly spin-polarized dissipationless supercurrents, which can be exploited for the emerging field of superconducting spintronics [47, 48, 85–88].
In particular, in the experimental systems studied in Ref. [67], to which we will apply the theoretical model described in this thesis, the hallmark of spin-triplet superconductivity seems to be expressed through a peculiar behavior of the critical current as a function of temperature. Hence, in our analysis, the simulated $I_c(T)$ will be the benchmark for the comparison with the experimental data, allowing us to give a more precise interpretation of the spin-triplet nature of transport properties characterizing these devices and, at the same time, highlighting the usefulness, in this framework, of obtaining information about transport phenomena in the considered system directly by looking at an experimentally accessible quantity such as the critical current.
In this thesis, we use a two-dimensional (2D) Bogolioubov de Gennes (BdG) tight-binding model [68, 89–91] to describe SFIS JJ. The proximity effect in such junctions has widely been investigated with quasiclassical approaches (i.e., Eilenberger equations [15, 17, 19, 92, 93]), which are particularly suitable for systems whose dimensions significantly exceeds the Fermi wavelength λ_f and the coherence length ξ_f [93].
Otherwise, here, we study tunnel SFIS JJs in the limit of the short junction

regime, by using an exact solution of the Gor'kov equation. This approach results to be appropriate, considering that the transport properties of the system vary considerably when the barrier length changes over a few lattice sites, i.e. the Josephson current experiences an exponential decay while gradually one moves away from the S/F interface. In contrast to the quasiclassical methods, our approach provides a description of the systems on the scale of the lattice site instead of the coherence length. This model is well-suited to evaluate site-by-site the current and the superconducting correlation functions and, thus, to obtain the proximity effects between two different regions.
In particular, the transport properties of the JJ (i.e. the Josephson current and the induced pairing correlation functions) are derived from the Green's function (GF) of the barrier, obtained by using the numerical calculation method based on the recursive Green's function (RGF) technique [89–91,94]. The RGF method is a powerful tool to compute transport properties in these kinds of systems, composed of two leads and a central device. It is very reliable and computationally efficient, and allows for the inclusion of several disorder mechanisms at the microscopic level (such as lattice defects and irregularities), as well as provides the possibility to deal with finite temperature issues.
The outline of the thesis is then as follows.

We begin the ***Chapter 1*** by making a brief recall of the FFLO state, which is a relevant example of coexistence of superconductivity and ferromagnetism. Then we will proceed by introducing some fundamental key concepts about the general features of proximity effect starting from S/N case to arrive at S/F systems, pointing out the main differences and peculiarities. Among these, we mention the characteristic damped oscillating behavior of the Cooper pair wave function in the F layer which leads us to the definition of the 0 and π states in SFS JJs. In the last part of this chapter, we will discuss the possibility of inducing long-range triplet pairing correlations and on the spin-orbit coupling as possible trigger process of these latter. We will conclude this section by mentioning that it is possible to study the transport properties of such systems by using the Green's functions formalism and, finally, by discussing the symmetry properties of superconducting pairings.

The ***Chapter 2*** is voted to the presentation of the theoretical framework used in this thesis. In particular, the first part describes in a general way the calculation method known as recursive Green's function (RGF) technique, employed to study the transport properties of SFIS JJs.
The RGF technique allows us to calculate the GF of the barrier, from which we derive all the physically relevant quantities of the system under analysis, reducing the computational cost with respect to the traditional direct inversion of the corresponding matrix Hamiltonian of the system.

Then, we present the theoretical 2D tight-binding model used to describe our system and how to apply the RGF calculation technique in our situation.

In ***Chapter 3*** we theoretically study the Josephson effect in SFIS JJs by using the numerical calculation method based on the RGF technique presented in Chapter 2, where the junction is described by the 2D BdG tight-binding model. In particular, we analyze the role of SOC and nonmagnetic impurities and recognize these two ingredients as key mechanisms to drive the 0-π transition in such devices. By calculating the critical current as a function of temperature $I_c(T)$ and the corresponding current-phase relation (CPR) $I(\phi)$ in the presence of impurities and SOC, we find that while SOC tends to bring the system toward the 0 state, the impurities, contrary, encourage it to turn toward the π state.

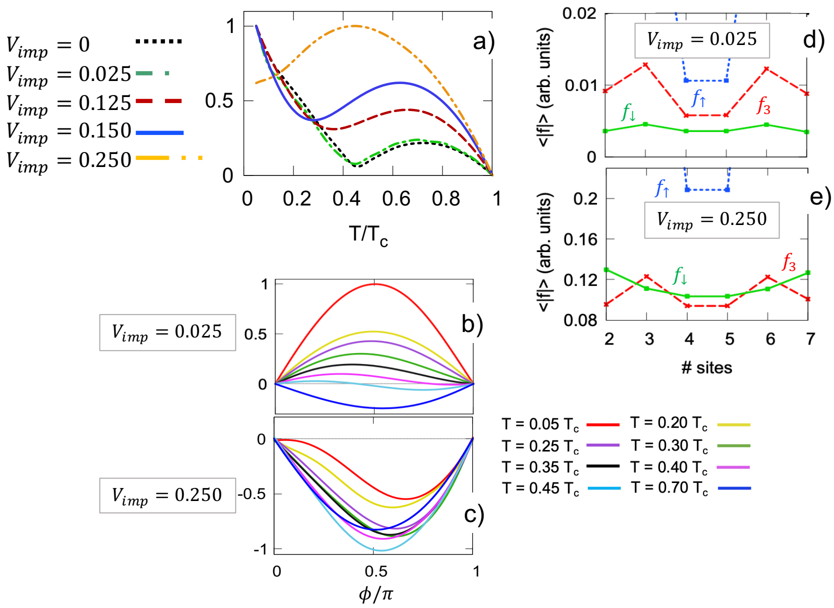

Figure 1: Summary of the main results of *Chapter 3*. $I_c(T)$ of SFIS JJ in the presence of lattice impurities and SOC, for different values of impurity potential V_{imp} (a). Calculated CPRs (b, c) showing the switching from 0-π to π regime, by increasing the lattice disorder. (d) and (e): enhancement of the s-wave spin-triplet correlations, due to increasing the disorder; f_3 is the opposite-spin triplet, $f_\uparrow$ and $f_\downarrow$ are the equal-spin triplets with up and down projection on the quantization axis (z), respectively.

We show that the compresence of these two competing effects modifies the $I_c(T)$ behavior when increasing the lattice disorder (whose representative pa-

rameter in the theoretical model is V_{imp}): keeping the SOC strength fixed, we pass from an $I_c(T)$ curve characterized by the typical cusp-minimum which signals the 0-π transition temperature, obtained in both the clean and quasi-clean situations (Fig.1 (a) black and green curves), to curves in which this minimum is gradually widened, until it is completely no longer visible, when increasing the disorder strength in the FI barrier (Fig.1 (a) red, blue, and orange curves). This corresponds to switch from a JJ exhibiting a 0-π transition to a totally π junction, as can be noticed by looking at the corresponding calculated CPR in Figs.1 (b) and (c)).
To complete our analysis, we also study the pairing correlations arising in these systems. In particular, we observe an enhanced contribution of the induced spin-triplet superconductivity when increasing the nonmagnetic disorder, as illustrated in Figs.1 (d) and (e). For this reason, we recognize these tunable SFIS JJs as good candidates to host unconventional superconducting pairing mechanisms and the source of sizable spin-triplet superconductivity.

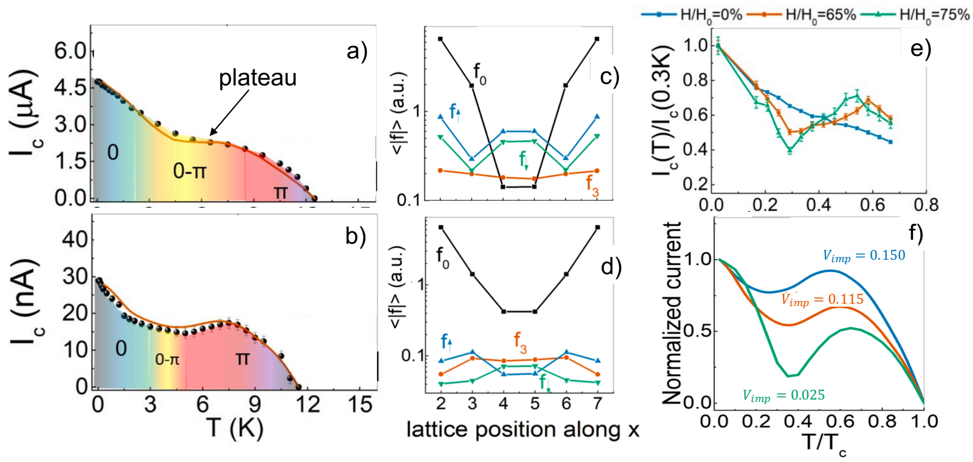

Figure 2: Summary of the main results of *Chapter 4*. Comparison between experimental (black points) and simulated (red line) $I_c(T)$, illustrating the plateau-like behavior (a) and a non-monotonic curve (b) characterized by a non-zero local minimum, pointing toward the 0-π transition. In (c) and (d) the corresponding calculated s-wave correlation functions are shown: f_0 is the spin-singlet, f_3 is the opposite-spin triplet and $f_\uparrow$ ($f_\downarrow$) is the equal-spin triplet with up (down) projection on the quantization axis (z); all the pairing components are reported on a log-scale. (e) Effect of the application of an external magnetic field H on the experimental junctions; (f) analogy with the simulations obtained by varying the impurities strength V_{imp}.

In ***Chapter 4*** we apply the theoretical 2D tight-binding model described in the previous chapters to real NbN-GdN-NbN junctions, experimentally investigated in a previous work studying the critical current I_c as a function of temperature T [67].
In this chapter, we focus on studying the induced pairing correlations in these devices, and their possible connection with the $I_c(T)$ behavior.
In particular, we show that an unconventional $I_c(T)$ behavior turns out to be the signature for the coexistence of spin-singlet and spin-triplet superconductivity in SFIS junctions, where the respective weight can be analyzed and parameterized in terms of nonmagnetic disorder and SOC parameters. We model the $I_c(T)$ curves in the whole temperature range, along with the corresponding current-phase relation (CPR) as a function of the temperature T. Specifically, we find that, when the $I_c(T)$ curve exhibits a region in which the I_c is constant over a wide range of temperatures, i.e. it shows a peculiar *plateau* (see Fig.2 (a)), the competition between the singlet and triplet pairing amplitudes becomes significant, showing an undoubtedly not negligible contribution of the equal-spin triplet correlations $f_\uparrow$ and $f_\downarrow$ (Fig.2 (c)). On the contrary, the more the $I_c(T)$ exhibits a behavior approaching the 0-π regime, presenting a more pronounced local minimum in the $I_c(T)$ curve (Fig.2 (b)), the lower is the relative weight of such equal-spin triplet components in the corresponding junctions (Fig.2 (d)).
Furthermore, to deepen the analysis of the peculiar transport properties characterizing these systems, we present a study on the analogy observed between the response of the experimental samples to the application of an external weak magnetic field H (Fig.2 (e))), and the role of SOC and impurities in the theoretical model (Fig.2 (f))). In our investigation, we find that the position in temperature of the minimum of the $I_c(T)$ curve represents an important benchmark relating the 0-π transition induced by the applied magnetic field in the experimental systems, to the combined effect of impurities, exchange field fluctuations and spin-orbit coupling in the simulations. Therefore, this analysis joining together the results of the $I_c(T)$ measurements with the outcomes of the microscopic modeling approach, provides the possibility to describe the combined effect of magnetic inhomogeneities and disorder in complex barriers, an assay which can be extended to a variety of hybrid types of JJs.

Chapter 1

Interplay between ferromagnetism and superconductivity

After the advent of the BCS theory by Bardeen, Cooper, and Schrieffer (1957), it became evident that superconductivity in the singlet state could be destroyed by an exchange mechanism [4–12]. Even though singlet superconductivity and ferromagnetism appear to be mutually exclusive effects due to the antagonistic nature of these two states of matter, their coexistence may be easily achieved in layered superconductor/ferromagnet (S/F) systems [15–19]. In this context, the *proximity effect* artificially allows for the coexistence of superconductivity and ferromagnetism, and offers a unique opportunity to study their interplay. In fact, in such S/F structures, the Cooper pairs can leak out of the superconductor, inducing superconducting correlations in the adjacent ferromagnetic layer over characteristic length scales near the interface [15,47]. For this reason, S/F hybrid structures present rich physics, which makes them both experimentally and theoretically attractive. This chapter aims to introduce the basics of the proximity effect, starting from the superconductor/normal metal (S/N) case, to point out the main differences with respect to S/F structures, on which the discussion will focus. One of the main peculiarities of such proximitized S/F systems is that the Cooper pair wave function extending from S to F exhibits a damped oscillatory behavior [15,20,47]. This results in many new effects, which we discuss in this thesis, as a non-monotonic dependence of the critical temperature T_c of S/F structures on the F layer thickness [95–102], up to the realization of the so called π state in superconductor/ferromagnet/superconductor Josephson junctions (SFS JJs) [30,31,33,56].
We will begin this chapter by making a brief reference to the superconducting phase predicted by Larkin and Ovchinnikov [27] and Fulde and Ferrell [26] in 1964 (the FFLO state), since S/F systems are in some ways analogous to

such nonuniform superconducting state, as the physical picture of the proximity effect can be also explained in terms of the FFLO state.
At this stage, we will not use a heavy mathematical formulation to explain these primary concepts which, however, deserve a brief overview to better contextualize the work described in this thesis. A more in-depth discussion on the theoretical framework used for the description of the systems analyzed in this work will be presented in Chapter 2.

1.1 Superconductivity interacting with ferromagnetism: the FFLO state

The coexistence between superconductivity and ferromagnetism can be observed in the vicinity of the interface linking a conventional superconductor with a ferromagnet in S/F bilayers, leading to a strong analogy between the so called *FFLO state* and the oscillatory-like proximity effect occurring in such S/F systems, which we will discuss later. For this reason, a brief recall of this peculiar state seems appropriate.
In 1964, Fulde and Ferrell [26] and Larkin and Ovchinnikov [27], independently of each other, theoretically predicted an unconventional nonuniform superconducting phase in superconductors under the influence of a strong uniform magnetic field. This novel superconducting phase is known as FFLO state. Generally, an applied magnetic field damages superconductivity in two distinct ways: orbital and paramagnetic pair-breaking effects. The relative importance of these two effects in the suppression of superconductivity is determined by the so-called Maki parameter $\alpha_M = \sqrt{2}H_{c2}^{O}/H_{c2}^{P}$ [12], where H_{c2}^{O} and H_{c2}^{P} are the upper critical fields for the orbital and spin pair-breaking mechanism, respectively. However, a large orbital effect is always detrimental to the FFLO state [103] and it was shown that the FFLO states may emerge only if $\alpha_M > 1$, when the orbital effect is weak or absent, and the Zeeman effect dominates, special situations which have been analyzed and studied by various experimental and theoretical works [104–109].
In view of this, in the following discussion, we will consider only the pure Pauli limit, corresponding to the limiting case of infinitely large Maki parameter, in which the uniform magnetic field acts only on the spins of the electrons and all orbital effects are neglected.
The FFLO state is identified by finite center-of-mass momentum in the Cooper pair, causing the superconducting order parameter to oscillate in real space. The mechanism at the base of the FFLO state formation is the different splitting of the Fermi momenta of spin-up and spin-down electrons, due to the presence of the Zeeman field. In the FFLO state electrons with opposite spin orientation can only stay bound if the Cooper pairs have finite center-of-mass momenta $\mathbf{Q}$, leading to the formation of a new pairing state $(\mathbf{k}\uparrow, -\mathbf{k}+\mathbf{Q}\downarrow)$, instead of the ordinary BCS one $(\mathbf{k}\uparrow, -\mathbf{k}\downarrow)$, as illustrated

in Fig.1.1.
The finite wave vector $\mathbf{Q}$ in the FFLO state gives rise to spatial symmetry breaking, resulting in a superconducting order parameter oscillating in space. Fulde and Ferrell suggested an order parameter of the form [104]

$$\Delta(\mathbf{r}) = \Delta_1 e^{i\mathbf{Q}\cdot\mathbf{r}} \,, \tag{1.1}$$

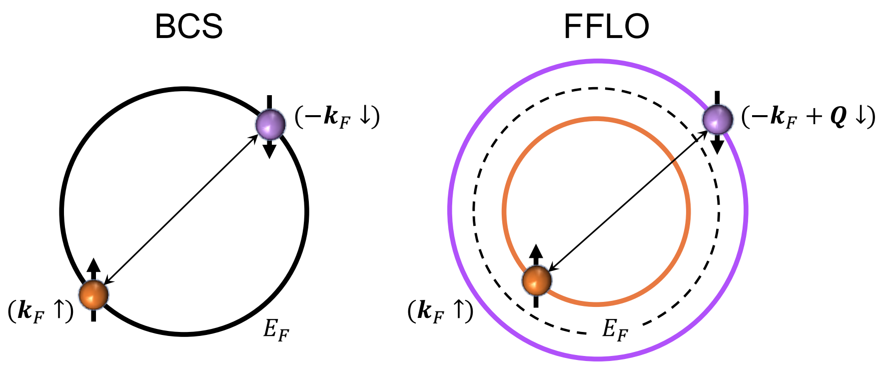

Figure 1.1: Schematic representation of the Cooper pair formation in the BCS (left) and FFLO (right) states. On the right, the energy of spin-up and spin-down electrons is shifted by the exchange field. Here, due to Zeeman splitting, the Fermi surfaces for electrons with spin up and down are represented, respectively, by the orange and violet circle.

where the amplitude of the superconducting order parameter is homogeneous, but the phase changes in real space over position $\mathbf{r}$. However, the two solutions $e^{\pm i\mathbf{Q}\cdot\mathbf{r}}$ represent degenerate superconducting states for a given $\mathbf{Q}$. This degeneracy can be lifted by considering linear combinations of $e^{\pm i\mathbf{Q}\cdot\mathbf{r}}$, that is the state originally proposed by Larkin and Ovchinnikov [104]

$$\Delta(\mathbf{r}) = \Delta_1 \left(e^{i\mathbf{Q}\cdot\mathbf{r}} + e^{-i\mathbf{Q}\cdot\mathbf{r}} \right) = 2\Delta_1 \cos\left(\mathbf{Q}\cdot\mathbf{r}\right) \,. \tag{1.2}$$

Generally, the order parameter is characterized by more than two equivalent $\mathbf{Q}$ wave vectors, then it can be expressed by a linear combination of terms with different Cooper pair momenta, as [47, 104]

$$\Delta_{FFLO}(\mathbf{r}) = \sum_{\nu} \Delta_\nu e^{i\mathbf{Q}_\nu\cdot\mathbf{r}} \,, \tag{1.3}$$

where ν denotes the number of equivalent $\mathbf{Q}$-vectors.
The occurrence of the FFLO state requires very stringent conditions on the superconducting materials; in addition to a weaker orbital pair breaking effect with respect to the Zeeman splitting, so that superconductivity survives up to the Pauli limit, the superconductor must be in the clean limit because it is known today that the FFLO state is very sensitive to disorder [110, 111]. Very few superconductors fulfill these necessary conditions for the FFLO state, justifying why it is rather difficult to observe such a phase in superconductors. Interesting candidates are quasi-2D superconductors when magnetic field is applied parallel to the superconducting planes. The theoretical treatment of these kinds of systems has been developed in different relevant works [107, 112–114].
In conclusion, here we wanted to highlight that, as we will see in the next sections, the same physics is at the origin of the oscillatory-like proximity effect near S/F interfaces, where the induced FFLO-like state leads to oscillation in space of the pair amplitude in the ferromagnetic region, resulting in many interesting phenomena observed in these systems (e.g. 0-π transitions) [15].

1.2 Proximity effect

Let us now discuss what happens when a superconductor S is placed in contact with a normal metal N. In this case, it is possible to observe that the superconductor modifies the behavior of the electrons in the normal region. Indeed, the adjacent metal starts exhibiting superconducting properties near the interface, induced over mesoscopic distances governed by the normal coherence length $\xi_N = v_F/2\pi T$ for a perfect (clean) N layer (or $\xi_N = \sqrt{D/2\pi T}$ in the dirty case, where D is the diffusion constant of the normal metal). The leakage of the Cooper pairs from S into N is called *proximity effect*. A sketch of the behavior of the induced superconducting order parameter at an S/N interface is shown in Fig.1.3 (a). At the same time, on the superconductor side, in the vicinity of the interface, the order parameter is depleted within a region equal to the coherence length of the superconductor $\xi_S = v_{Fs}/2\pi T_c$ (or $\xi_S = \sqrt{D_S/2\pi T_c}$ in dirty regime); this phenomenon is known as inverse proximity effect [15].
The proximity effect in S/N structures can be explained on a microscopic level through the Andreev reflection process [115–118], which plays a primary role for the understanding of quantum transport properties of S/N systems. Let us consider an electron of energy ϵ from the normal metal propagating toward the superconductor, as illustrated in Fig.1.2 (a). The normal metal that is next to the superconductor has electrons filled up to the Fermi level. Electrons in the N part with an excitation energy below the superconducting gap ($\epsilon < \Delta$) cannot cross the interface, since no single-particle states are available in the superconductor below the gap. Thus, electrons can pass

from N to S only if their energy ϵ exceeds the superconducting gap Δ above the Fermi level. However, another interesting scenario is possible. In 1964 the Russian physicist Alexander F. Andreev [115] showed that an electron with energy lower than the superconducting gap can cross the interface and then be reflected as a hole (see Fig.1.2 (a)), experiencing the so called *Andreev reflection*. The corresponding charge $2e$ is transferred throughout the interface and becomes a Cooper pair on the superconducting side. This scenario also works for the opposite situation, namely when an incident hole from the N side is reflected as an electron, breaking a Cooper pair in the superconductor and transferring the charge $2e$ across the interface and into the normal metal. The Andreev reflection process conserves energy, spin and (approximately, when $\Delta \ll E_F$) momentum.

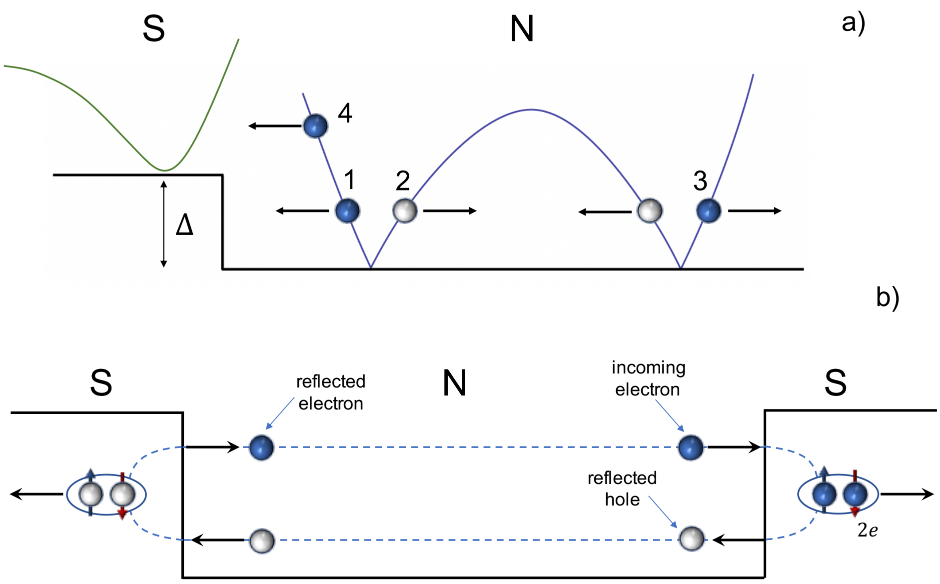

Figure 1.2: (a): Schematic representation of the Andreev reflection at S/N interface. The curves represent the electrons (blue balls) and holes (white balls) dispersion at the Fermi surface; the arrows indicate the direction of propagation. Contrary to electron 1, electron 4 can directly enter the superconductor, since $\epsilon > \Delta$. However, 1 can either be reflected as electron (3), or Andreev-reflected as a hole (2) with opposite velocity; simultaneously a Cooper pair is created in S. (b) Andreev bound states in SNS system.

Then, the essence of the proximity effect can be summarized as follows: the Andreev reflection induces a coherent superposition of electron and hole in

N, thus creating superconducting correlations in the normal metal. Hence, the coherence length basically measures the distance from the interface up to which the phases of the induced superconducting correlations stay coherent. Additionally, Andreev bound states appear and generate a Josephson effect when the metallic layer is interposed between two superconductors (SNS junctions, as in Fig.1.2 (b)), producing a flowing Josephson current through the system [117, 119–122].

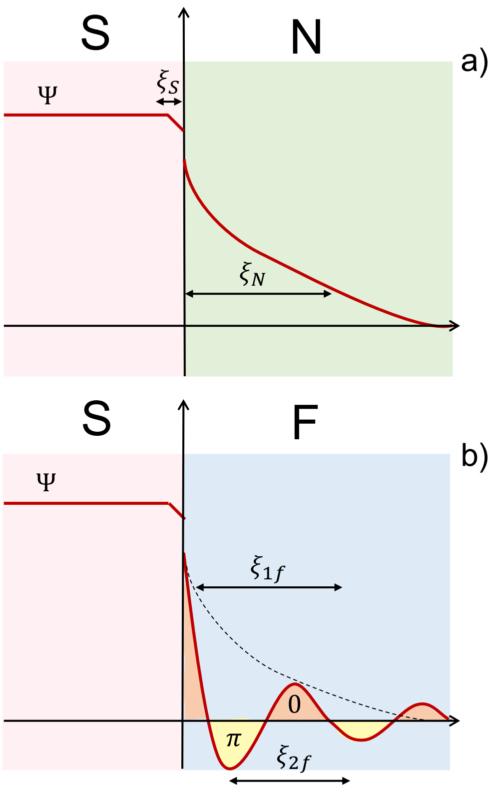

Figure 1.3: Schematic picture of proximity effect which shows the behavior of the superconducting order parameter Ψ at (a) S/N and (b) S/F interfaces.

1.2.1 Features of the proximity effect in the presence of ferromagnetism

At this point, it is legitimate to ask how the proximity effect changes if a ferromagnet is placed next to the superconductor, instead of a normal metal. Superconducting correlations induced in a ferromagnet differ qualitatively from those in S/N proximitized systems. In this context, the proximity effect offers not only the possibility to investigate on the quantum transport

properties in these systems from a microscopic point of view, but it also represents a unique opportunity to study the interplay between ferromagnetism and superconductivity.
The BCS theory, which well describes conventional superconductors, tells us that a Cooper pair consists of two electrons with opposite spins and momenta. The Cooper pairs leaking from the S side toward an adjacent ferromagnet F by proximity effect, feel the exchange interaction which acts on the spin of electrons forming the pair, producing a Zeeman-split of spin-up and spin-down bands. Thus, on the one hand, since the two spin bands are not equally populated due to the exchange splitting, the Andreev scattering is partially suppressed, inasmuch as an incoming electron can not enter the condensate if there is no partner of exactly opposite spin and momentum at given excitation energy, as schematically illustrated in Fig.1.4. Consequently, this makes the formation of Cooper pairs less efficient. Secondly, by forcing the spins to be parallel, the exchange field destroys the phase correlation between the spin-up and spin-down electrons of a singlet pair, suppressing the superconducting correlations over a coherence length scale shorter than that characterizing the normal layer.

What happens is that the exchange interaction energetically favors one spin direction; in particular, the spin-up electron decreases its energy by the ferromagnetic exchange energy h, while the spin-down electron increases it by the same amount. Because the total energy is conserved, to compensate this potential energy variation, spin-up electron increases its kinetic energy while the spin-down electron decreases it.

As a consequence, the Cooper pair acquires a center of mass momentum $Q = 2h/v_F$ [15,20,47] that produces an oscillation in space of superconducting pair amplitude in F. A qualitative picture of this effect has been provided by Demler, Arnold, and Beasley [20], schematically illustrated in Fig.1.5.
Then, considering the case of F layer with homogeneous magnetization, and supposing for simplicity the one-dimensional situation, at a distance x from the S/F interface the initial singlet state $\left(1/\sqrt{2}\right)(|\uparrow\downarrow\rangle - |\downarrow\uparrow\rangle) \equiv |S=0, S_z=0\rangle$ (where S is the total spin of the pair and S_z its projection on the z-axis) obtains a phase multiplier $\exp(\pm iQx)$, depending on the orientation of the electron spin:

$$\begin{aligned} |00\rangle = \left(1/\sqrt{2}\right)(|\uparrow\downarrow\rangle - |\downarrow\uparrow\rangle) \longrightarrow |\Psi\rangle &= \left(1/\sqrt{2}\right)\left(|\uparrow\downarrow\rangle e^{iQx} - |\downarrow\uparrow\rangle e^{-iQx}\right) \\ &= \left(1/\sqrt{2}\right)(|\uparrow\downarrow\rangle - |\downarrow\uparrow\rangle)\cos(Qx) + i\left(1/\sqrt{2}\right)(|\uparrow\downarrow\rangle + |\downarrow\uparrow\rangle)\sin(Qx) \ . \end{aligned} \tag{1.4}$$

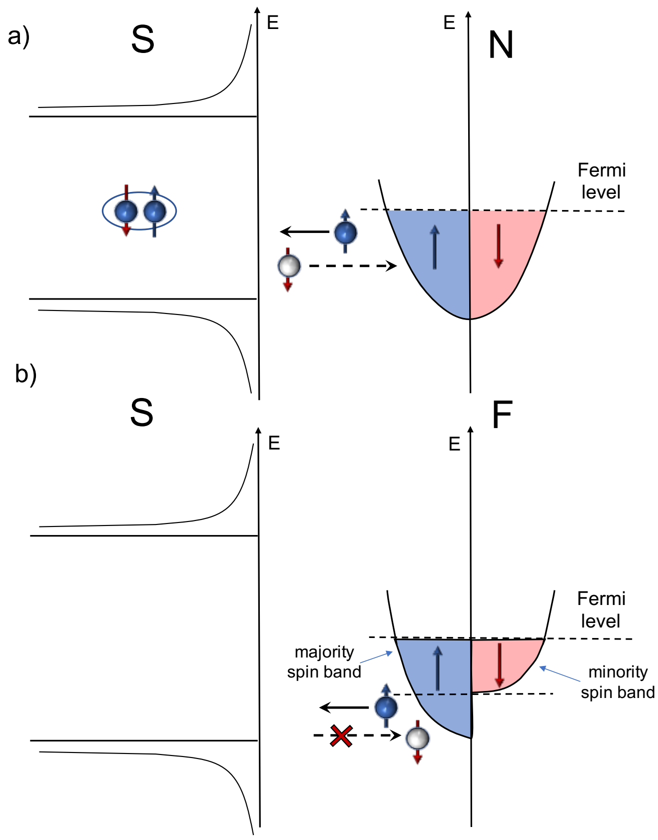

Figure 1.4: Schematic representation of differences between Andreev reflection at the S/N (a) and S/F interface (b). In the case of S/N interface (a), the spin bands are equally populated, implying that the incoming spin-up electron is reflected as a spin-down hole for any $\epsilon < E_F$, and meanwhile, a Cooper pair is created in the superconductor. In (b) it is shown that, in S/F systems, when no spin-down states are available at certain energies due to exchange splitting of spin bands, the Andreev reflection of the incoming spin-up electron may be suppressed and the Cooper pair in S is not created.

In the above equation, we can notice the analogy with the oscillating in space FFLO state described previously and defined by Eq.(1.3).
Thus, the second-line in Eq.(1.4) can be decomposed into a spin singlet and a spin triplet $\left(1/\sqrt{2}\right)(|\uparrow\downarrow\rangle + |\downarrow\uparrow\rangle) \equiv |S=1, S_z=0\rangle$ pairing state

$$|\Psi\rangle = \cos\left(Qx\right)|00\rangle + i\sin\left(Qx\right)|10\rangle \ . \tag{1.5}$$

Eq.(1.5) shows that the zero triplet component $|10\rangle$ appears automatically in any S/F system due to the different phase shifts acquired by the spin-up and

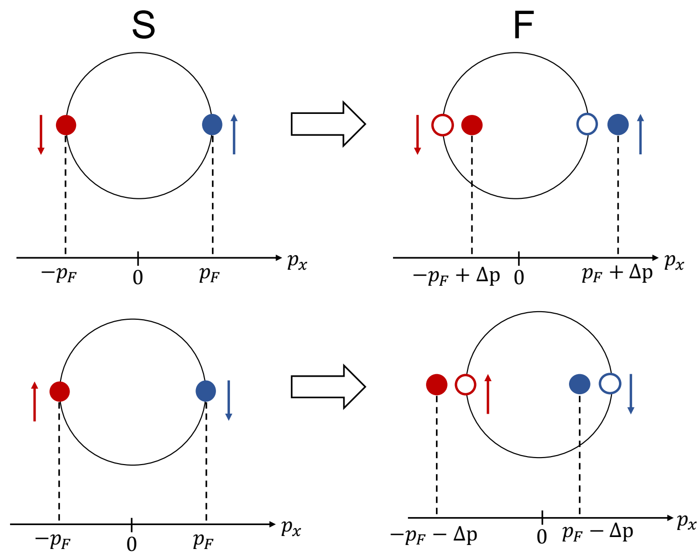

Figure 1.5: Picture of proximity effect in S/F system: Cooper pair going from S to F acquires a momentum $\pm 2\Delta p = Q = 2h/v_F$ (Adapted from [20]).

spin-down electrons as they propagate in F [47]. Even though this is not a rigorous calculation, this superposition of singlet and triplet amplitudes explains the oscillatory behavior of the Cooper pair wave function in the F layer.
However, in S/F bilayers such oscillation in space of the Cooper pair wave function is not the only characteristics of the penetration of the superconducting correlations in the ferromagnet; in fact, the Cooper pair wave function appears also modulated by an exponential decay with the distance from the interface. As for the S/N case, also for S/F systems there is a quantitative difference between the decay lengths of clean and diffusive ferromagnets. The microscopic treatment of this issue is described within the framework of the quasiclassical theory of superconductivity by the Eilenberger (clean regime) and Usadel (dirty regime) equations [15, 17]. In the dirty limit it can be derived that the effective coherence length in a ferromagnet is a complex function $\xi_f = \xi_{1f} + i\xi_{2f}$, with the consequence that the decay and oscillation of the superconducting order parameter in F are respectively described by the length scales $\xi_{(1,2)f} = \sqrt{\frac{D}{\left[h^2+(\pi T)^2\right]^{1/2} \pm \pi T}}$ [30], where $D = v_F \ell/3$ is the diffusion constant depending on the Fermi velocity v_F and the mean free path ℓ in the F layer [123, 124]. Then, the Cooper pair wave function takes the form

$$\Psi \sim \exp\left(-\frac{x}{\xi_{f1}}\right) \cos\left(\frac{x}{\xi_{f2}}\right) . \tag{1.6}$$

In particular, in real ferromagnets (i.e. classical ferromagnets as Fe, Co, Ni) the exchange field is large compared with the superconducting critical temperature ($h \gg T_c$) and one can find that $\xi_{1f} = \xi_{2f}$ exactly coincide, leading to a unique characteristic length scale defined by $\xi_f = \sqrt{\dfrac{D}{h}}$.
On the other hand, in the case of a clean ferromagnet, the characteristic decay and oscillation lengths of the superconducting correlations are not coinciding. As directly follows from the Eilenberger equations [15, 17], the coherence length is still a complex function but here the decay and oscillating lengths are respectively defined as $\xi_{1f} = v_F/2\pi T$ and $\xi_{2f} = v_F/2h$. In this case, the Cooper pair wave function takes the form [15]

$$\Psi \sim \frac{1}{x} \exp\left(-\frac{x}{\xi_{1f}}\right) \sin\left(\frac{x}{\xi_{2f}}\right) . \tag{1.7}$$

The schematic behavior of the superconducting order parameter at S/F interfaces is depicted in Fig.1.3 (b).

1.2.2 Oscillatory behavior of T_c in S/F systems

In S/F bilayers and multilayers, the oscillatory behavior of the superconducting order parameter induced in ferromagnets may lead to a non-monotonic dependence of the superconducting transition temperature T_c on the F layer length (d_F) (Fig.1.6(a)). Indeed, when this latter is smaller than the oscillating length, i.e. $d_F \ll \xi_{2f}$, the Cooper pair wave function in F changes slightly and is similar to the superconducting order parameter in the adjacent S layer. This corresponds to a zero phase in the wave function describing the superconducting order parameter in the S layer in S/F multilayer structures, and we call this state the "0" phase (Fig.1.6(b)). On the other hand, when $d_F \sim \xi_{2f}$ the Cooper pair wave function may cross the zero at the center of the F layer and change the sign, producing a π shift of the phase of the superconducting order parameter in the neighboring S layer; we call this state the "π" phase (Fig.1.6(c)). Then, by increasing the F layer thickness, it is possible to induce subsequent switching between 0 and π phases, leading to a non-monotonic dependence of the critical temperature on the F layer thickness $T_c\,(d_F)$. This oscillatory-type dependence of $T_c\,(d_F)$ was first theoretically predicted [95, 96] and then also experimentally observed [97–102]. However, experiments on $T_c(d_F)$ behavior in S/F systems were not initially so conclusive; indeed, although the non-monotonic oscillation behavior of $T_c(d_F)$ was eperimentally observed in various works, negative results was also reported [126, 127]. Furthermore, in the original theory of the proximity effect proposed by Buzdin et al. [95, 96] itself, the transitions between 0 and π phases in S/F bilayers are considered not possible in the presence of a

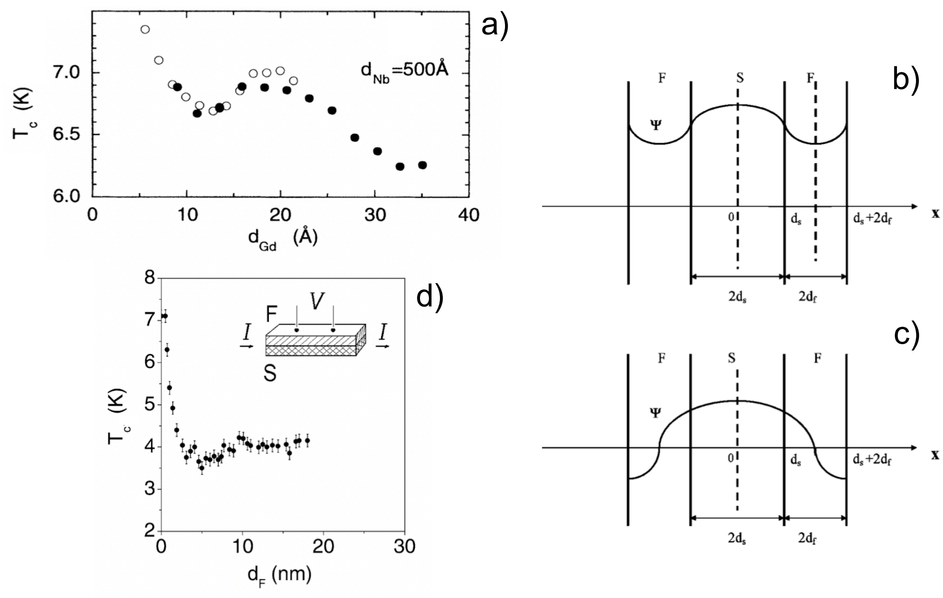

Figure 1.6: (a): Experimental data reported in [97] showing the oscillation of T_c of Nb/Gd multilayers vs thickness of Gd layer d_{Gd} for a fixed value of Nb layer. Schematic representation of the behavior of the Cooper pair wave function in the 0 phase (b) and π phase (c) The x axis is chosen perpendicular to the planes of the S and F layers with thicknesses $2d_s$ and $2d_f$, respectively. The Cooper pair wave function in the π phase vanishes at the center of the F layers and $\Psi(x)$ is antisymmetric toward the center of the F layer [15]. (d): Critical temperature of $Nb/Cu_{0.43}Ni_{0.57}$ bilayer as a function of the F layer thickness [125].

single S layer. All these issues led to a lack of agreement between theory and experiments, revealing the different and sometimes controversial behavior of $T_c(d_F)$ in the various structures. In light of this, for the interpretation of both theoretical and experimental results, other mechanisms have been suggested to take into account, as the interference between the normal quasiparticle reflection at the free boundary of F layer and Andreev reflection at S/F interface [22,125,128,129], due to the comparability between d_F and ξ_{2f} in such systems; the effect of a finite interface transparency [127], spin-flip scattering [20,130], and others.

1.2.3 Formation of the π state

The fact that, as we have seen in the previous section, in S/F multilayers transitions from 0 to π phase may occur, has an interesting implication. Indeed, this allows us to extend the discussion to the case of ferromagnetic Josephson junctions (SFS JJ), thus providing the possibility to have an equi-

librium phase difference between the two superconducting electrodes not only of zero but, under particular circumstances, also of π.
Then, it is natural to call these latter junctions π JJs, to distinguish them from the conventional 0 JJs.
This effect was predicted in 1977 by Bulaevskii et al. [112] who discussed the tunneling through a JJs with an insulating barrier in the presence of magnetic impurities.

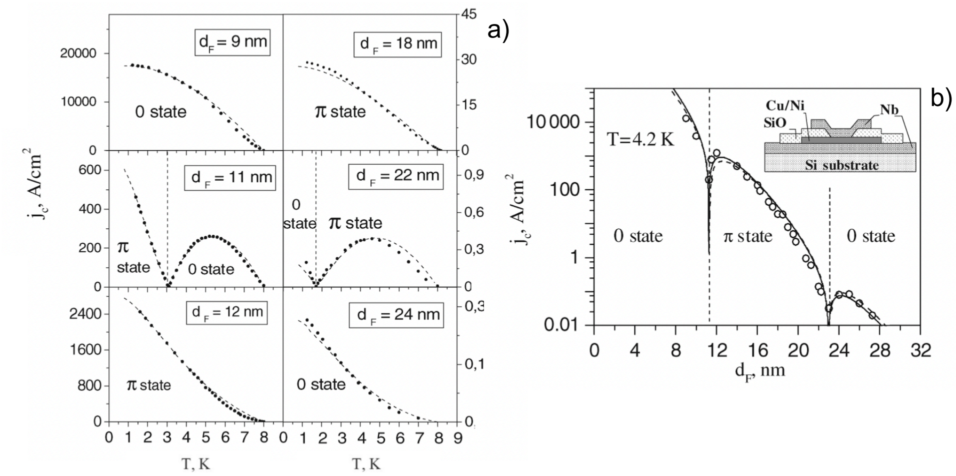

Figure 1.7: (a): Temperature dependence of the critical current density $j_c(T)$ for $Nb/Cu_{0.47}Ni_{0.53}/Nb$ junctions for various d_F. In the middle panels, the cusp indicates the temperature-driven π-0 and 0-π transitions. (b): $j_c(d_F)$ dependence for $Nb/Cu_{0.47}Ni_{0.53}/Nb$ junctions at $T = 4.2K$ [31].

The supercurrent flowing across a JJ is usually described by the sinusoidal current-phase relation $I(\phi) = I_c \sin\phi$, where I_c is the Josephson critical current and ϕ is the superconducting phase difference across the junction. Correspondingly, the associated Josephson energy reads: $E_J = \dfrac{\Phi_0 I_c}{2\pi}(1 - \cos\phi)$ [70,71], where Φ_0 is the superconducting flux quantum. For conventional JJs (0 JJs), $I_c > 0$ and the minimum energy is achieved at $\phi = 0$. Conversely, for the π junction, the critical current is negative $(I_c < 0)$ and $\phi = \pi$ corresponds to the ground state energy. In this case, the current-phase relation is modified to: $I(\phi) = |I_c| \sin(\phi + \pi) = -|I_c| \sin(\phi)$, in terms of the magnitude of the critical current $|I_c|$.
Then, the transition from the 0 to the π state results in a sign change of the critical current. For this reason, measurements of the I_c in SFS JJs may be adequate to reveal the 0-π transition. Indeed the temperature dependence

of the oscillation length of the superconducting order parameter in the F layer is also the origin of the anomalous behavior of the critical current I_c as a function of temperature, as can be seen in Fig.1.7(a)), where the 0-π crossover is identified by the presence of a peculiar cusp in the $I_c(T)$ curve at the transition temperature.
In this respect, the first unambiguous experimental confirmation of the 0-π transition in SFS JJs via critical current measurements was provided by Ryazanov and coworkers [30, 31], and subsequently these results have been confirmed in other experimental works [32]. Later works have also studied oscillations induced by a variation of the F layer thickness d_F. Indeed, these systems exhibit a non-monotonic behavior of the critical current I_c as a function of d_F, where the vanishing of I_c signals the transition from the 0 to the π state (Fig.1.7(b)). The current through a SFS JJ was first calculated by Buzdin et al. [33, 56], who evaluated the critical current as a function of the F layer thickness d_F for different transparencies at the left and right S/F interfaces, by solving the Usadel equations in the dirty limit near the transition temperature T_c. In particular they found the expression for the critical current as a function of d_F in the limits of completely and low transparent interfaces. They also calculated the $I_c(d_F)$ behavior in a more realistic situation, closer to real experimental systems, considering one S/F boundary with a low transparency interface while the other interface quite transparent, generalizing the results for the case of superconducting electrodes with different gaps and diffusion constants. Then, several other experiments confirmed the theoretical predictions [34, 35, 131].
We will not derive in detail the appearance of the π state in SFS junctions, for which a complete theoretical description is provided within the quasi-classical formalism [15, 17, 56]. However, as discussed in the next chapters, we will draw attention to the role that π and $0-\pi$ junctions may have in different scenarios, due to their applicability as architectural elements for the improvement of nanostructures and the realization of new types of devices.

1.3 Long-range proximity effect

In any S/F system, when the magnetization in the F layer is homogeneous, triplet correlations between electrons of opposite spins are created (Eq.(1.5)). In particular, these opposite spin-triplet correlations, together with the spin singlet ones, get dephased by the presence of the exchange field and are suppressed with distance from S/F interface, on a length scale given by h/Δ in the clean regime, and exponentially in diffusive structures on the length scale $\xi_f = \sqrt{D/h}$, where h is the ferromagnetic exchange energy. For this reason, they are called short-range pairing correlations.
However, the possible scenarios offered by S/F systems are not limited to a such short range proximity. In the first decade of the 2000s, several the-

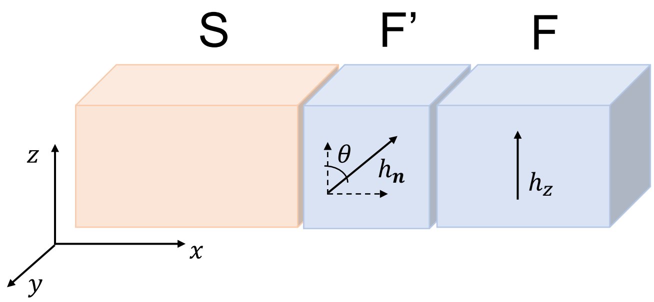

Figure 1.8: SF′F trilayer considered for the explanation of LRTC formation. The two ferromagnetic layers have different orientation of their magnetization: F′ is magnetized along an axis in the x-z plane at an angle θ measured from the z-axis, while F is magnetized along the z-axis.

oretical works predicted the appearance of spin-triplet pair correlations in S/F systems in the presence of magnetic inhomogeneities as, for example, non-collinear magnetizations in different parts of ferromagnetic multilayers structures [21, 44–47]. In particular, such superconducting pairing correlations, characterized by triplet amplitudes with a spin projection $S_z = \pm 1$ on the quantization axis of the ferromagnet, are called *equal-spin* correlations ($|11\rangle = |\uparrow\uparrow\rangle$, $|1-1\rangle = |\downarrow\downarrow\rangle$). For this reason, they are not subject to the exchange field in F, because both electrons of the pair have the same spin. Hence, they may persist over long distances in F and decay in ferromagnet on the same length scale as in normal metals ξ_N, thus, giving rise to a long-range proximity effect. This latter, was subsequently also observed experimentally by various groups [48–55].

To give an explanation of how such long-range spin-triplet components can be obtained, let us consider adding a second ferromagnetic layer (F′) to the structure (i.e. SF′F trilayer illustrated in Fig.1.8), whose magnetization axis is non-collinear with that of the first one (F). In particular, we suppose that F′ is magnetized along an axis in the x-z plane at an angle θ measured from the z-axis in spin space, and F is magnetized along the z-axis. As we have seen in Eq.(1.5), when the singlet Cooper pair leaks in F′, it transforms as a mixture of singlet and opposite-spin triplet amplitudes, where $|00\rangle_\theta = \left(\frac{1}{\sqrt{2}}\right)(|\swarrow\nearrow\rangle - |\nearrow\swarrow\rangle)$ and $|10\rangle_\theta = \left(\frac{1}{\sqrt{2}}\right)(|\swarrow\nearrow\rangle + |\nearrow\swarrow\rangle)$ are the states projected onto the spin quantization axis in F′, defined by the versor $\mathbf{n} = \cos(\theta)\mathbf{e}_z + \sin(\theta)\mathbf{e}_x$. Then, the superconducting correlations further leak in F where the magnetization is along the z-axis, thus we project the pairing states on $\mathbf{e}_z$, by using the following transformation formulas for basis vectors [47]

$$\begin{aligned}|\nearrow\rangle &= \cos\left(\frac{\theta}{2}\right)|\uparrow\rangle + \sin\left(\frac{\theta}{2}\right)|\downarrow\rangle \\ |\swarrow\rangle &= \cos\left(\frac{\theta}{2}\right)|\downarrow\rangle - \sin\left(\frac{\theta}{2}\right)|\uparrow\rangle\,.\end{aligned} \tag{1.8}$$

These projected states can be used to obtain the following transformation for pair amplitudes

$$|00\rangle_\theta \longrightarrow |00\rangle \tag{1.9}$$

$$|10\rangle_\theta \longrightarrow \cos(\theta)\,|10\rangle - \left(\frac{1}{\sqrt{2}}\right)\sin(\theta)\,[|\uparrow\uparrow\rangle - |\downarrow\downarrow\rangle]\ ,$$

finding that while the singlet state $|00\rangle_\theta$ is invariant under a rotation in spin space since it has a zero total spin ($S = 0$), the zero projection triplet state in the rotated θ-basis $|10\rangle_\theta$ produces a non-zero projection triplet state with aligned spins in the z-basis ($|\uparrow\uparrow\rangle$ and $|\downarrow\downarrow\rangle$ terms in (1.9)). Thus, F$'$ creates opposite spin triplet pairs in the θ-basis which will be equal spin triplets in F, when viewed with respect to the z-axis.
Therefore, by susbtituting Eqs.(1.9) in Eq.(1.5) we obtain the final state $|\Psi\rangle$ in the rotated spin frame

$$|\Psi\rangle = \cos(Qx)\,|00\rangle + i\sin(Qx)\left\{\cos(\theta)\,|10\rangle - \left(\frac{1}{\sqrt{2}}\right)\sin(\theta)\,[|\uparrow\uparrow\rangle - |\downarrow\downarrow\rangle]\right\}. \tag{1.10}$$

Thus, magnetic inhomogeneities mix singlet and triplet pair components at interfaces and create long-range triplet correlations (LRTC) in ferromagnetic proximitized structures. This is realizable, non only by considering two ferromagnetic layers with misaligned magnetic fields, as mentioned here, but also, for example, in the presence of magnetic domain walls near the interfaces on a length scale given by the magnetic length [15, 21], or interfaces with magnetic disorder [42, 132]. Another option is given by a single ferromagnet with a nonhomogenous exchange field [133], or a time-varying exchange field [134]. Finally, as we will discuss in the next paragraph, there exist theoretical proposals to use SOC as a substitute for inhomogeneous magnetization to generate LRTC in such systems, since spin-orbit interaction leads to a mixing of the spin channels.

1.3.1 Spin-orbit coupling as a source of long-range superconducting pairings

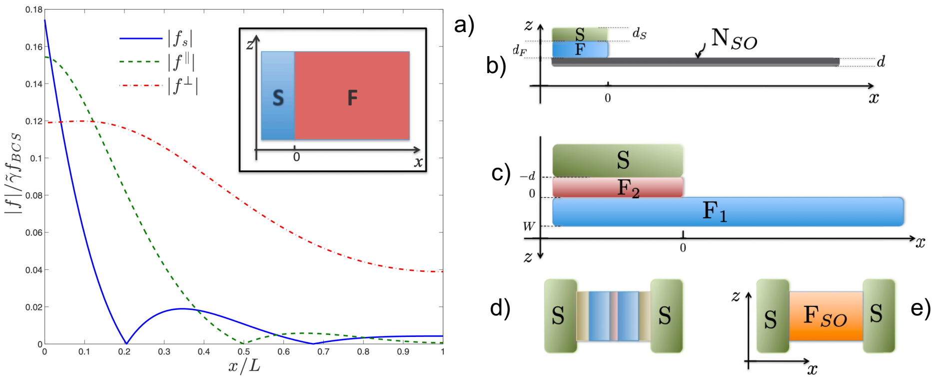

Figure 1.9: (a): Spatial dependence of all pairing amplitudes for the S/F system shown in the inset. f_s and $f^{\parallel}$ are the zero-spin singlet and triplet components, while $f^{\perp}$ is the triplet long-range component. The exchange field in F is homogeneous and points in the z direction, while a fully isotropic SOC is assumed in F (from [135]). In (b-e) are shown the different geometries discussed in [135].

As we have seen, the presence of magnetic inhomogeneities creates equal-spin triplet pairing correlations with non-zero spin projection with respect to the magnetization axis of the ferromagnetic layer.
However, this is not the only way to obtain such LRTC, as various works illustrated that, in the clean regime [136–139], spin-orbit coupling (SOC) is an alternative source of the LRTC besides the magnetic inhomogeneities studied in the past. Furthermore, Bergeret and Tokatly [135, 140] showed that SOC of Rashba [141] and Dresselhaus [142] type satisfies the condition of all triplet projections also in the diffusive (dirty) limit.
Physically, the generation of long-range pairing correlations can be viewed as a rotation of the triplet component of the superconducting condensate in S/F hybrid structures in the presence of SOC, leading to components $f^{\perp}$ perpendicular to the original one (as illustrated in Fig.1.9 (a)), which restore the long-range decay behavior of the induced Cooper pair wave function.
By using the quasiclassical equations including the effect of the spin-orbit field, they predicted the appearance of LRTC in a variety of diffusive hybrid S/F structures in which SOC is present (Figs.1.9 (b-e)). Furthermore, discussing the condition for the singlet-triplet conversion, they also demonstrated the equivalence in the creation of LRTC of the role played by the inhomogeneous magnetization, and SOC under the presence of an homogeneous exchange field. In particular, this analogy provides a useful tool for designing experimental setups and studying novel combinations of materials for the manipulation of the triplet component in hybrid superconducting structures, suggesting a possible way to control the spin in S/F heterostructures in the presence of SOC, particularly attractive for the development of

new technological devices in the field of spintronics.
In particular, in this thesis, this last-mentioned appealing purpose encouraged us to focus our study on ferromagnetic-insulator Josephson junctions (SFIS JJs) characterized by an intrinsic SOC as a generator of long-range supercurrents, besides regarding SOC as a useful tool for driving the evolution of the $I_c(T)$ of SFIS JJs from 0-π to 0 regime, as we will see in detail in Chapter 3.

1.4 The Green's functions formalism to describe transport properties of hybrid systems

In order to efficiently describe transport phenomena and, therefore, the motion of electrons and holes in such hybrid heterostructures, in this work we choose to use the formalism based on Green's functions (GFs). The formulation of the BCS theory in terms of GFs derived by Gor'kov [149] represents an efficient way to study proximity systems. As a matter of fact, GFs include the proper information allowing to directly obtain from them the relevant physical quantities of interest, such as currents and density of states [94, 150]. Since the superconducting state somehow mixes electrons and holes, such Green's functions not only describe these latter but, more generally, by introducing the Nambu (particle-hole) space and spin space, also quasiparticles and spin correlations can be depicted. Then, it is natural to introduce two-component field operators in real space, called *Nambu* operators [120]

$$\Psi\left(\boldsymbol{r}\right)=\begin{pmatrix}\psi_{\uparrow}\left(\boldsymbol{r}\right)\\ \psi_{\downarrow}^{\dagger}\left(\boldsymbol{r}\right)\end{pmatrix},\ \Psi^{\dagger}\left(\boldsymbol{r}\right)=\begin{pmatrix}\psi_{\uparrow}^{\dagger}\left(\boldsymbol{r}\right), & \psi_{\downarrow}\left(\boldsymbol{r}\right)\end{pmatrix}, \tag{1.11}$$

where $\Psi\left(\boldsymbol{r}\right)$ annihilates electron at position $\mathbf{r}$, whereas $\Psi^{\dagger}\left(\boldsymbol{r}\right)$ creates electron at position $\mathbf{r}$. At this point, we can define the *Nambu-Gor'kov Green's function*

$$\check{G}\left(\boldsymbol{r},t,\boldsymbol{r'},t'\right)=-i\langle\mathcal{T}(\Psi\left(\boldsymbol{r},t\right)\Psi^{\dagger}\left(\boldsymbol{r'},t'\right))\rangle \tag{1.12}$$

where $\mathcal{T}$ is the time-ordering operator and the brackets $\langle\ \rangle$ denote the thermal average $\langle O\rangle=Tr\left(e^{-H/(k_BT)}O\right)$ (where H is the Hamiltonian of the system).
The GF in Eq.(1.12) takes the form of a 2×2 matrix in the particle-hole (Nambu) space:

$$\check{G}\left(\boldsymbol{r},t,\boldsymbol{r'},t'\right)=\begin{bmatrix}G_1 & F_1\\ -F_2 & G_2\end{bmatrix} \tag{1.13}$$

where its elements are respectively

$$G_1 = G_{\uparrow\uparrow}\left(\boldsymbol{r}, t, \boldsymbol{r'}, t'\right) = -i\langle\mathcal{T}\left(\psi_\uparrow\left(\boldsymbol{r}, t\right)\psi_\uparrow^\dagger\left(\boldsymbol{r'}, t'\right)\right)\rangle, \tag{1.14}$$

$$G_2 = G_{\downarrow\downarrow}^\dagger\left(\boldsymbol{r}, t, \boldsymbol{r'}, t'\right) = -i\langle\mathcal{T}\left(\psi_\downarrow^\dagger\left(\boldsymbol{r}, t\right)\psi_\downarrow\left(\boldsymbol{r'}, t'\right)\right)\rangle, \tag{1.15}$$

$$F_1 = F_{\uparrow\downarrow}\left(\boldsymbol{r}, t, \boldsymbol{r'}, t'\right) = -i\langle\mathcal{T}\left(\psi_\uparrow\left(\boldsymbol{r}, t\right)\psi_\downarrow\left(\boldsymbol{r'}, t'\right)\right)\rangle, \tag{1.16}$$

$$F_2 = F_{\downarrow\uparrow}\left(\boldsymbol{r}, t, \boldsymbol{r'}, t'\right) = -i\langle\mathcal{T}\left(\psi_\downarrow^\dagger\left(\boldsymbol{r}, t\right)\psi_\uparrow^\dagger\left(\boldsymbol{r'}, t'\right)\right)\rangle. \tag{1.17}$$

The diagonal elements of $\check{G}$ matrix in Eq.(1.13), G and $G^\dagger$, represent respectively the particle-particle and the hole-hole propagator and they are called *normal Green's functions*. The off-diagonal elements F and $F^\dagger$, instead, represent respectively the particle-hole and the hole-particle propagators and they are called *anomalous Green's functions*. Hence, the anomalous GFs describe the superconducting condensate, thus the pairing correlations.
In the presence of exchange field or other interactions that provide spin mixing effects, e.g. spin-orbit coupling, the GFs G and F in the Nambu-Gor'kov matrix (Eq.1.13)) become non trivial 2×2 matrices in the spin space (that we indicate as $\hat{G}$ and $\hat{F}$).
In particular, in this thesis, to describe finite temperature properties of considered systems, we will work with Matsubara GFs. The latter can be obtained by passing to immaginary-time through the transformation $t = -i\tau$ [120]. Then, by Fourier transforming, one can obtain the GF G_{ω_n}, where $\omega_n = \pi T(2n + 1)$ are the Matsubara frequencies and T is the temperature.
Therefore, the anomalous GF in Matsubara representation $\hat{F}_{\omega_n}$ can be expressed in terms of the Cooper pairs correlation functions as [90]

$$\hat{F}_{\omega_n}\left(\boldsymbol{r}, \boldsymbol{r}\right) = \sum_{\nu=0}^{3} f_\nu(\boldsymbol{r})\hat{\sigma_\nu} i\hat{\sigma_2} \tag{1.18}$$

where $\hat{\sigma}_\nu$ are the Pauli matrices in the spin space ($\hat{\sigma}_0$ is the 2×2 unit matrix), $f_0 = |00\rangle$ and $f_3 = |10\rangle$ are the amplitudes of singlet and zero-spin triplet component of the Cooper pairs correlations, respectively, while f_1 and f_2 allow to obtain the spin-aligned triplet components $f_{\uparrow\uparrow} = |\uparrow\uparrow\rangle$ and $f_{\downarrow\downarrow} = |\downarrow\downarrow\rangle$. Eq.(1.18) can be written in the matrix form as

$$\hat{F} = \begin{pmatrix} f_{\uparrow\uparrow} & f_{\uparrow\downarrow} \\ f_{\downarrow\uparrow} & f_{\downarrow\downarrow} \end{pmatrix} = \begin{bmatrix} if_2 - f_1 & f_3 + f_0 \\ f_3 - f_0 & if_2 + f_1 \end{bmatrix}, \tag{1.19}$$

where, in the left hand side matrix, the spin aligned components appear as diagonal elements, while the opposite spin components are the off-diagonal ones.
As we will see, Eq.(1.19) will be used in Chapters 3 and 4 to derive the superconducting pairing correlations in the analyzed systems.

1.5 Symmetries of pairing correlations

The wave function of a Cooper pair depends on the position (orbital part), spin, and time (energy or frequency) coordinate of electrons forming the pair. Therefore, it can be found that all the superconducting correlations introduced in the previous section can be classified according to their symmetry properties with respect to all these quantities [41, 47, 143]. As we will see, four different symmetry components exist in S/F heterostructures, that may be comparable in size.
As we said, the pairing correlations in superconductors are described by the anomalous Green's function F, which can be expressed as

$$F_{\alpha\beta,ab}(\mathbf{r}_1,\tau_1,\mathbf{r}_2,\tau_2) = \langle \mathcal{T}_\tau \Psi_{\alpha\,a}(\mathbf{r}_1,\tau_1)\Psi_{\beta\,b}(\mathbf{r}_2,\tau_2)\rangle\,, \tag{1.20}$$

where $\mathcal{T}_\tau$ is the time-ordering operator, $\mathbf{r}_{1,2}$ and $\tau_{1,2}$ are the spatial and imaginary-time (in the Matsubara technique) coordinates of the electrons comprising the Cooper pair, $\{a, b\}$ denote any orbital degree of freedom, while $\{\alpha, \beta\}$ are spin indices of the two fermions in the correlator. The Pauli principle requires that this function is overall odd, thus changing its sign under the exchange of two electrons

$$F_{\alpha\beta,ab}(\mathbf{r}_1,\tau_1,\mathbf{r}_2,\tau_2) = -F_{\beta\alpha,ba}(\mathbf{r}_2,\tau_2,\mathbf{r}_1,\tau_1)\,. \tag{1.21}$$

For homogeneous systems, F depends only on relative coordinates $\mathbf{r} = \mathbf{r}_1 - \mathbf{r}_2$ and $\tau = \tau_1 - \tau_2$ of the electrons forming the pair, therefore it follows:

$$F_{\alpha\beta,ab}(\mathbf{r},\tau) = -F_{\beta\alpha,ba}(-\mathbf{r},-\tau)\,. \tag{1.22}$$

We can see that, in this particular case, it is possible to express the symmetry restrictions on the permutation properties in terms of spin (S), coordinate parity (P^*), orbital index (O), and time coordinate (T^*) permutation operators, respectively as

$$SF_{\alpha\beta,ab}(\mathbf{r},\tau)S^{-1} = F_{\beta\alpha,ab}(\mathbf{r},\tau) \tag{1.23}$$
$$P^*F_{\alpha\beta,ab}(\mathbf{r},\tau)P^{*-1} = F_{\alpha\beta,ab}(-\mathbf{r},\tau) \tag{1.24}$$
$$OF_{\alpha\beta,ab}(\mathbf{r},\tau)O^{-1} = F_{\alpha\beta,ba}(\mathbf{r},\tau) \tag{1.25}$$
$$T^*F_{\alpha\beta,ab}(\mathbf{r},\tau)T^{*-1} = F_{\alpha\beta,ab}(\mathbf{r},-\tau)\,. \tag{1.26}$$

The combined action of these operators is referred to as the *SPOT rule*, leading to the change in sign in Eq.(1.22) which can symbolically be written as: $SP^*OT^* = -1$ [143]. These symmetry permutation rules were pointed out for the first time by Berezinskii in 1974 [144].
By Fourier-transforming the relative coordinates in Eq.(1.22) we get

$$F_{\alpha\beta,ab}(\mathbf{p},\omega_n) = -F_{\beta\alpha,ba}(-\mathbf{p},-\omega_n)\,. \tag{1.27}$$

For inhomogeneous systems this equation holds for each set of center coordinates.
The symmetry constraints in spin, momentum, and Matsubara frequency ($\omega_n = (2n+1)\pi T$), expressed through Eq.(1.27), can be satisfied by four possible superconducting states (see Fig.1.10), exhausting all possibilities compatible with the Fermi statistics and Pauli principle:

- Type A: spin singlet, even frequency, even parity
- Type B: spin singlet, odd frequency, odd parity
- Type C: spin triplet, even frequency, odd parity
- Type D: spin triplet, odd frequency, even parity.

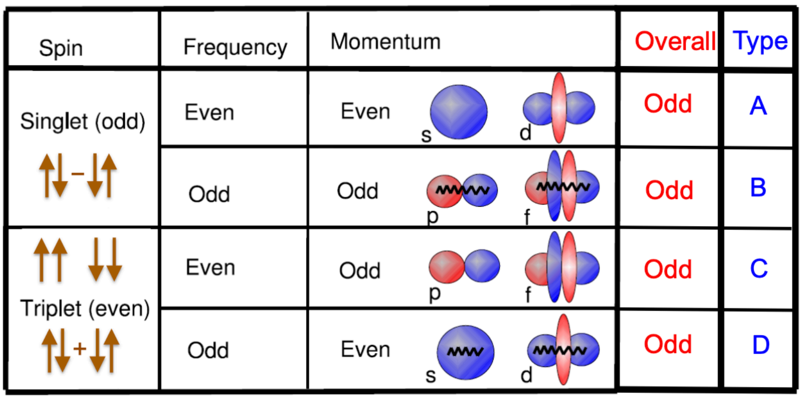

Figure 1.10: Symmetry classification of the pair correlation function; the wavy lines indicate odd-ω states (from [47]).

To better explain this classification, we can notice that the spin part of Eq.(1.27), which is a matrix in spin space, can be divided into singlet and triplet functions as [41]

$$F_{\alpha\beta}(\mathbf{p},\omega_n) = F_s(\mathbf{p},\omega_n)(i\sigma_y)_{\alpha\beta} + \mathbf{F}_t(\mathbf{p},\omega_n)\cdot(\boldsymbol{\sigma} i\sigma_y)_{\alpha\beta}\,, \tag{1.28}$$

where $\boldsymbol{\sigma} = (\sigma_x, \sigma_y, \sigma_z)$ is the vector of the three Pauli matrices.
The singlet part is odd under the spin exchange $\alpha \longleftrightarrow \beta$, while the three triplets are even. Therefore, in order to satisfy the overall odd symmetry nature of the pair correlation function, for the singlet state the wave function is necessarily either symmetric or anti-symmetric in both momentum and frequency. By contrast, in a triplet state, the wave function is either

anti-symmetric in momentum and symmetric in frequency (even-ω) or symmetric in momentum and anti-symmetric in frequency (odd-ω).
In reference to the above symmetry type classification, we can remind that the usual singlet s-wave BCS superconductivity is of type A, while an example of type B was introduced by Balatsky and Abrahams in the case of unconventional superconductors with singlet odd pairing correlations [145,146]; moreover, type C is represented by the spin-triplet p-wave superfluid state formed in ^{3}He [147]. Finally, type D was also considered by Berezinskii in connection with the discovery of the superfluid phase in ^{3}He [144].
The appearance of these different symmetry components of the pairing correlations is subject to the local breaking of peculiar symmetry properties in some spatial regions of the considered systems, e.g. near interfaces, or in the presence of line defects.
In particular, as we will see in the situation analyzed in this thesis, if both spin rotational symmetry and parity are broken, e.g. at an interface between a superconductor and a ferromagnet with SOC, all four types of pair amplitudes are generated at the interface [68, 148].
The possibility of dealing with different unconventional pairing states symmetries continues to be an intriguing field still being explored, especially as regards the presence of odd-ω states, due to their fundamental influence on both the electromagnetic response and spin properties of such systems, that may be relevant for possible technological applications.

Chapter 2

RGF technique and model Hamiltonian

In this thesis, for the description of SFIS JJ we choose to employ a two dimensional (2D) tight-binding lattice model, which is appropriate to evaluate site by site the currents and the induced superconducting pairing correlations due to the proximity effect between different regions.
As anticipated in the previous chapter, the transport properties of the junction are derived by using the Green's functions formalism. Then, the Green's function describing the whole system is obtained by applying the *Recursive Green's function* (RGF) technique [89, 91]. The strong points of the RGF technique are: (i) it does not require the derivation of the boundary conditions at the various interfaces, which, contrary, sometimes is a thorny issue in the quasiclassical approaches; (ii) it entails a reduction of the computational cost of calculation, gaining a factor L^2 (where L is the length of the barrier in number of sites) in efficiency with respect to the direct inversion of corresponding matrix Hamiltonian for the calculation of the barrier GF, from which we can extract the relevant physical quantities of interest; (iii) it turns out to be a suitable approach to effortlessly take into account disorder effects.
The first part of this chapter is voted to the general description of the RGF technique, which can be usefully applied to systems described by lattice models, as the case we analyze in this thesis. Then, we will proceed with the presentation of the 2D tight binding model used to represent SFIS junctions. In this part we will focus on the explanation of the different interactions included in the Hamiltonian of the considered system, such as the presence of SOC and nonmagnetic lattice impurities. Finally, we will pass to the application of the RGF method to our situation, which leads us to the calculation of the GF of the barrier from which we will derive the Josepshon current and the superconducting correlation functions.

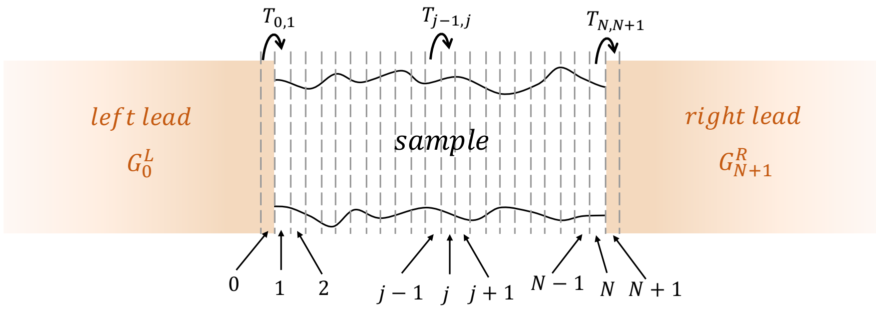

Figure 2.1: Slices division of the system consisting of two leads and one central device (sample). The sample is formed by N different sections. The surface Green's functions of the two leads are indicated with G_0^L and G_{N+1}^R. The perturbation T couples two neighbor sections (adapted from [154]).

2.1 RGF technique

The recursive Green's function (RGF) technique is a well established method firstly introduced in the study of electronic transport in mesoscopic systems [151–153]. Moreover, in the last twenty years this calculation technique has been widely employed to investigate the transport properties of superconducting Josephson junctions (JJs) [89–91]. Indeed, the RGF procedure allows calculating the Green's function of a "central" device when it is connected to two leads. In particular, as we will see, when dealing with a JJ the two leads are the superconducting electrodes and the central device is represented by the barrier.

The RGF method become extremely useful if the device GF cannot be computed from the direct inversion of its Hamiltonian, as, for large systems, the latter calculation procedure may be seriously expensive from a computational point of view.

In this section we will explain and describe the general features of the RGF method. The first step is considering the central device as consisting of different sections, as illustrated in Fig.2.1, whose non-interacting isolated GFs (G^0) can be exactly computed. In order to calculate the interacting GF (G) of each section, we have to consider their interactions with the other subsystems. In this model, the perturbation T connects only nearest neighbor sections. Hence, in this schematic representation of the central device, the section j interacts only with its nearest-neighbors one $j+1$ and $j-1$.

We can calculate the interacting GF of each section by using a *Dyson-like* equation [94, 154]

$$G = G^0 + G^0 T G. \tag{2.1}$$

This picture can be easily applied to systems described by lattice models, as illustrated in Fig.2.2 (a). Here, the basic idea is still to break up the system into independent stripes (labeled by the index j) and then glue them together by the means of the Eq.(2.1), which allows building the full GF slice by slice. Starting from the edge of one lead, using Eq.(2.1), one attaches the first stripe of the central device to the lead by calculating the GF of the connected system: lead + first stripe. At each step another stripe is added to the already connected system, until one reconstructs the whole system: lead-device-lead. In Fig.2.2 (a) the central device is coupled to the left (L) and right (R) edges. Since T connects only the section j with its nearest-neighbors $j+1$ and $j-1$, only the surfaces of the two leads have to be considered. In Fig.2.2 (b) a sketch of the system divided in single transverse stripes is shown.

From now on, we will indicate with $G^0_{j,j}$ the (unperturbed) *bare* GF of the

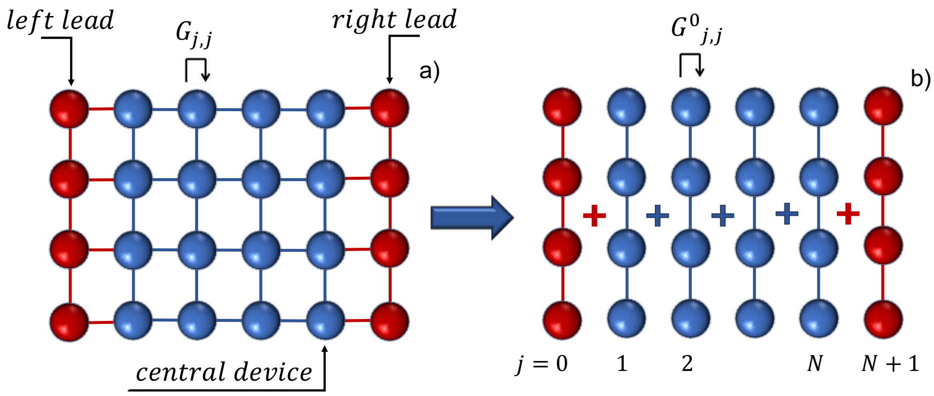

Figure 2.2: (a) Schematic of the system made up of two leads and one central device. In (b) the system divided in single stripes. $G_{j,j}$ is the GF of the j-th stripe when connected to the others, while $G^0_{j,j}$ indicates the *bare* GF of the isolated j-th stripe.

j-th isolated stripe and with $G_{j,j'}$ the interacting GF that couples the j-th stripe with the j'-th one.

Thus, the method requires as input the surface GFs of left and right lead, defined as G^L_0 and G^R_{N+1}, respectively. These GFs are computed separately and before the recurrence procedure.

Since our goal is to connect each stripe to the two leads, the derivation of several intermediate recurrence formulas is needed, before obtaining expressions for the whole device GF. Thus, carrying out the recurrence procedure first from left to right and then from right to left, it is possible to generate two families of GFs, $G^L_{j,j'}$ and $G^R_{j,j'}$, describing interacting GFs connected to the left and right lead, respectively. As final step, these two families are then joined together to obtain the exact full G of the central device.

2.1.1 Left Green's Function

We begin calculating the left GFs. We recall that the rightmost slice of the left lead is denoted by 0. Then, our goal is to obtain $G^L_{0,j}$ and $G^L_{j,j}$ in order to describe electron propagation in the sample when the left lead is taken into account (Fig.2.3).

Therefore, the first step is to incorporate the first slice $j = 1$ to the left

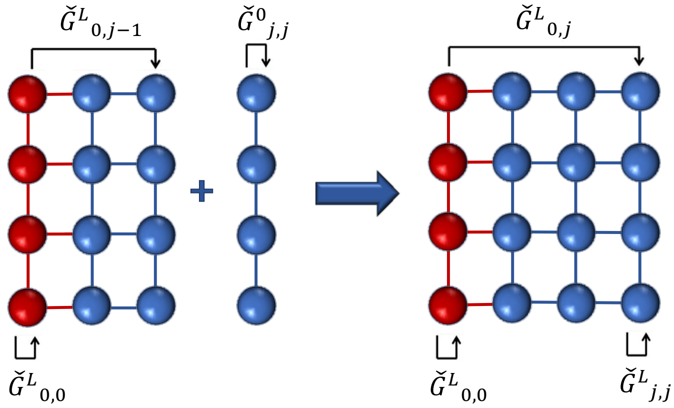

Figure 2.3: Graphical representation of how to attach the stripe j to the left lead. The first $j-1$ stripes are already connected. In order to attach the stripe j, we have to calculate $G^L_{j,j}$ and $G^L_{0,j}$.

lead. In order to simplify the calculations, we define the kets $|j\rangle$ representing the state of the electron in the stripe j.
Thus, by using the Dyson-like Eq.(2.1), we obtain:

$$\begin{gathered}
\langle 1| G^L |1\rangle = \langle 1| G^0 |1\rangle + \langle 1| G^0 T G^L |1\rangle = \\
\langle 1| G^0 |1\rangle + \sum_{j,j'} \langle 1| G^0 |j\rangle \langle j| T |j'\rangle \langle j'| G^L |1\rangle = \\
\langle 1| G^0 |1\rangle + \langle 1| G^0 |1\rangle \langle 1| T |0\rangle \langle 0| G^L |1\rangle
\end{gathered} \tag{2.2}$$

where at the second step we used the completeness relation $\left(\sum_j |j\rangle\langle j| = 1\right)$. Here we exploit the fact that T couples only nearest-neighbors stripes, i.e. $\langle j| T |j'\rangle = T_{j,j'}\delta_{j,j'+1}\delta_{j,j'-1}$.
It is worth to notice that the left GF of the first stripe $G^L_{1,1}$ depends on the GF that connects it to the left lead $G^L_{0,1}$. We again use Eq.(2.1) to obtain

an expression for $G^L_{0,1}$.

$$
\begin{aligned}
\langle 0| G^L |1\rangle = \langle 0| G^0 |1\rangle + \langle 0| G^0 T G^L |1\rangle = \\
\langle 0| G^0 |1\rangle + \sum_{j,j'} \langle 0| G^0 |j\rangle \langle j| T |j'\rangle \langle j'| G^L |1\rangle \\
= \langle 0| G^0 |0\rangle \langle 0| T |1\rangle \langle 1| G^L |1\rangle \; .
\end{aligned}
\tag{2.3}
$$

In the third line of Eq.(2.3) we have taken into account that G^0 is the unperturbed GF of the system divided in isolated stripes, thus it cannot couple two separated stripes together. Hence, the matrix element $\langle 0| G^0 |1\rangle = 0$.
Adopting the more compact notation $\langle j| G^L |j'\rangle = G^L_{j,j'}$, we obtain the following two equations:

$$
G^L_{1,1} = G^0_{1,1} + G^0_{1,1} T_{1,0} G^L_{0,1} \tag{2.4}
$$

$$
G^L_{0,1} = G^L_0 T_{0,1} G^L_{1,1}. \tag{2.5}
$$

Therefore, by substitution, we have:

$$
G^L_{1,1} = G^0_{1,1} + G^0_{1,1} T_{1,0} G^L_0 T_{0,1} G^L_{1,1}, \tag{2.6}
$$

which is a self-consistent equation for the GF of the first stripe connected to the left lead $G^L_{1,1}$.
Then, with some algebra, we get

$$
G^L_{1,1} = \left(I - G^0_{1,1} T_{1,0} G^L_0 T_{0,1} \right)^{-1} G^0_{1,1}, \tag{2.7}
$$

where I is the identity operator. Notice that this GF takes into account the coupling of the first stripe with the left lead, but has no information about the rest of the system or the right lead.
Once calculated $G^L_{1,1}$, we can proceed evaluating the left GF of the second stripe $G^L_{2,2}$, attaching it to the first one, and so on, until we reach the right lead.
At this point, it is desirable to derive a more general recursive formula analog to Eq.(2.7) that is valid for each stripe of the central device.
Assuming that we have just attached the first $j-1$ stripes to the left lead, now we want to connect the j-th stripe to the resulting system.
Applying the Eq.(2.1), we can find a self consistent expression for $G^L_{j,j}$:

$$
\begin{aligned}
G^L_{j,j} = \langle j| G^L |j\rangle = \langle j| G^0 |j\rangle + \langle j| G^0 T G^L |j\rangle = \\
\langle j| G^0 |j\rangle + \langle j| G^0 |j\rangle \langle j| T |j-1\rangle \langle j-1| G^L |j\rangle = \\
G^0_{j,j} + G^0_{j,j} T_{j,j-1} G^L_{j-1,j}
\end{aligned}
$$

where, using again Eq.(2.1), for $G^L_{j-1,j}$ we have

$$G^L_{j-1,j} = \langle j-1|\, G^0 \,|j\rangle + \langle j-1|\, G^0 \,|j-1\rangle \,\langle j-1|\, T \,|j\rangle \,\langle j|\, G^L \,|j\rangle =$$

$$G^0_{j-1,j-1} T_{j-1,j} G^L_{j,j}\,.$$

We notice that $G^0_{j-1,j-1}$ is the GF of $j-1$-th stripe, when connected to the system made up of the left lead and the $j-2$ preceding stripes. Therefore, $G^0_{j-1,j-1} = G^L_{j-1,j-1}$ and it has memory of the $j-2$ steps which led to that point. Thus, we have :

$$G^L_{j,j} = G^0_{j,j} + G^0_{j,j} T_{j,j-1} G^L_{j-1,j-1} T_{j-1,j} G^L_{j,j}. \tag{2.8}$$

Furthermore, we can obtain the generalized recursive formula for the left GF of the j-th stripe:

$$G^L_{j,j} = \left(I - G^0_{j,j} T_{j,j-1} G^L_{j-1,j-1} T_{j-1,j}\right)^{-1} G^0_{j,j}\,. \tag{2.9}$$

The Eq.(2.9) is accompanied by the equation for the GF which connects the surface stripe of the left lead with the j-th stripe of the central device.

$$G^L_{0,j} = G^L_{0,j-1} T_{j-1,j} G^L_{j,j}\,. \tag{2.10}$$

2.1.2 Right Green's Function

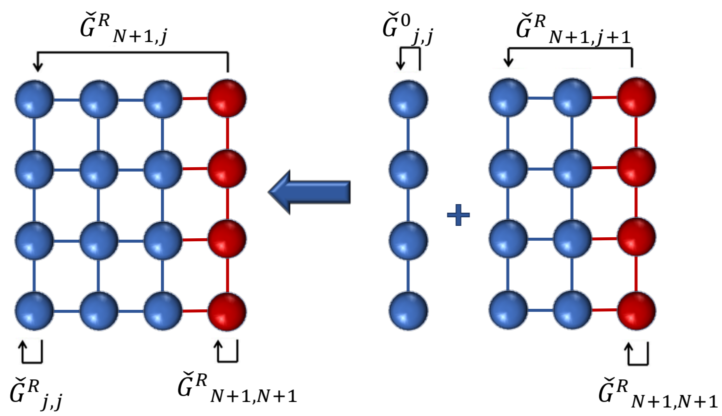

Figure 2.4: Graphical representation of how to attach the stripe j to the right lead. The last $N-j$ stripes are already connected. At this point, we can repeat the same procedure to attach the j-th stripe to the right (R) lead, Fig.2.4. In order to attach the stripe j, we have to calculate $G^R_{j,j}$ and $G^R_{N,j}$.

Similarly to left case, we start connecting the last stripe $j = N$ to the right lead, obtaining the following equations

$$\begin{aligned} G^R_{N,N} &= G^0_{N,N} + G^0_{N,N} T_{N,N+1} G^R_{N+1,N} \\ G^R_{N+1,N} &= G^R_{N+1} T_{N+1,N} G^R_{N,N} \,. \end{aligned} \tag{2.11}$$

Once we have attached the N-th stripe to the lead, we can repeat the procedure $N - j$ times, thus obtaining a recursive expression for right GF of the j-th stripe $G^R_{j,j}$. In this way, it is possible to find for the right GF of the j-th stripe the general self-consistent equations:

$$G^R_{j,j} = \left(I - G^0_{j,j} T_{j,j+1} G^R_{j+1,j+1} T_{j+1,j}\right)^{-1} G^0_{j,j} \tag{2.12}$$

$$G^R_{N+1,j} = G_{N+1,j+1} T_{j+1,j} G^R_{j,j} \tag{2.13}$$

that describe how the j-th stripe is connected to the right lead. It is worth to notice that $G^R_{j,j}$ depends on $G^R_{j+1,j+1}$, which is the GF of the preceding stripe. The latter has memory of all the preceding stripes from the right lead to the $j+2$-th one.

2.1.3 Full Green's Function

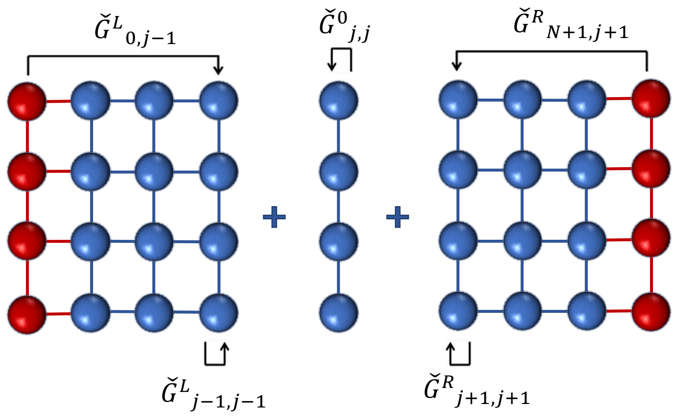

Figure 2.5: Graphical representation of how to attach the left subsystem to the right subsystem through the stripe j. The first $j-1$ stripes and the last $N-j$ stripes are already connected. In order to reconstruct the whole connected system, we have to calculate $G_{j,j}$.

Once we arrived at the j-th stripe both from the left and right leads, we can proceed to obtain the exact full GF of the central device. At this step, we have already computed the left GF of the $j-1$-th stripe ($G^L_{j-1,j-1}$) and the right GF of the $j+1$-th one ($G^R_{j+1,j+1}$). The system is composed by three parts:

- the isolated j-th stripe;
- the subsystem composed by the left lead and the first $j-1$ stripes;
- the subsystem composed by the right lead and the last $N-j$ stripes.

Hence, we have to connect the two parts together through the j-th stripe. In order to calculate the total GF G of the connected system at the j-th stripe, we again use the Eq.(2.1), which we project on the state vector $|j\rangle$ obtaining

$$G_{j,j} = \langle j| G |j\rangle = \langle j| G^0 |j\rangle + \langle j| G^0 T G |j\rangle =$$

$$\langle j| G^{(0)} |j\rangle + \sum_{j',j''} \langle j| G^{(0)} |j'\rangle \langle j'| T |j''\rangle \langle j''| G |j\rangle =$$

$$\langle j| G^0 |j\rangle + \langle j| G^0 |j\rangle \langle j| T |j-1\rangle \langle j-1| G |j\rangle +$$

$$\langle j| G^0 |j\rangle \langle j| T |j+1\rangle \langle j+1| G |j\rangle .$$

Therefore, for $G_{j,j}$ we have:

$$G_{j,j} = G^0_{j,j} + G^0_{j,j} \left(T_{j,j-1} G_{j-1,j} + T_{j,j+1} G_{j,j+1} \right) . \tag{2.14}$$

Following the same procedure, we can obtain a recursive formula even for $G_{j-1,j}$ and $G_{j+1,j}$. Let us do the explicit calculations for $G_{j-1,j}$:

$$\begin{aligned} G_{j-1,j} &= \langle j-1| G^0 |j\rangle + \langle j-1| G^0 T G |j\rangle = \\ &\sum_{j',j''} \langle j-1| G^0 |j'\rangle \langle j'| T |j''\rangle \langle j''| G |j\rangle = \\ &\langle j-1| G^0 |j-1\rangle \langle j-1| T |j\rangle \langle j| G |j\rangle = \\ &G^0_{j-1,j-1} T_{j-1,j} G_{j,j} . \end{aligned} \tag{2.15}$$

For the system considered, we can notice that $G^0_{j-1,j-1} = G^L_{j-1,j-1}$ because the $j-1$-th stripe is connected to the left lead. Thus, we have:

$$G_{j-1,j} = G^L_{j-1,j-1} T_{j-1,j} G_{j,j} . \tag{2.16}$$

An analogue equation is valid for $G_{j+1,j}$:

$$G_{j+1,j} = G^R_{j+1,j+1} T_{j+1,j} G_{j,j}. \tag{2.17}$$

By substitution, we can obtain a self-consistent expression for $G_{j,j}$ depending on $G^L_{j-1,j-1}$ and $G^R_{j+1,j+1}$.

$$G_{j,j} = \left[I - G^0_{j,j} \left(T_{j,j-1} G^L_{j-1,j-1} + T_{j,j+1} G^R_{j+1,j+1} \right) \right]^{-1} G^0_{j,j} \tag{2.18}$$

The Eq.(2.18) is accompanied by the equations that connect the left and right leads with the j-th stripe.

$$G_{0,j} = G^L_{0,j-1} T_{j-1,j} G_{j,j} \tag{2.19}$$

$$G_{N+1,j} = G^R_{N+1,j+1} T_{j+1,j} G_{j,j} \tag{2.20}$$

Note that to carry out the whole recursive algorithm we need to perform $2N$ matrix inversions (N for the left GF and N for the right GF). If W is the number of sites within each stripe of our lattice, the GFs of each stripe are $W \times W$ matrices. Each inversion requires $O(W^3)$ operations. Thus, the complexity of the calculation scales as $N \times W^3$ [154]. In this way, we gain a factor N^2 in efficiency with respect to the direct inversion of the $N \times W$ Hamiltonian matrix of the central device that, instead, scales as $N^3 \times W^3$.

2.2 Tight-binding model Hamiltonian

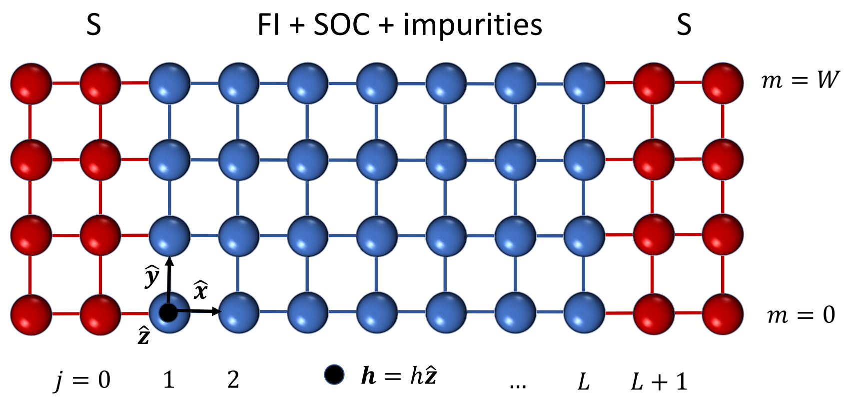

Figure 2.6: Schematic representation of the SFIS junction geometry with a ferromagnetic insulator barrier in the presence of SOC and impurities. The exchange field **h** is taken parallel to the z-axis, thus perpendicular to the junction plane (i.e., the xy-plane).

We start defining the Hamiltonian of the SFIS JJ, modeled by using a two-dimensional lattice, as illustrated in Fig.2.6, where L is the length of the ferromagnetic barrier and W is the width of the junction, expressed in units of lattice sites. Each lattice site position is determined by a couple of indices (j, m). By defining two unit vectors $\mathbf{x}$ and $\mathbf{y}$, we can introduce a vector $\mathbf{r} = j\mathbf{x} + m\mathbf{y}$ which points a lattice site with $j = 0, 1, \ldots, L, L+1$ and $m = 1, \ldots, W$. The Hamiltonian of the junction in the Nambu $\otimes$ spin space is given by

$$\check{\mathcal{H}} = \sum_{\mathbf{r},\mathbf{r}'} \Psi^\dagger(\mathbf{r}) \begin{bmatrix} \hat{H}(\mathbf{r},\mathbf{r}') & \hat{\Delta}(\mathbf{r},\mathbf{r}') \\ -\hat{\Delta}^*(\mathbf{r},\mathbf{r}') & -\hat{H}^*(\mathbf{r},\mathbf{r}') \end{bmatrix} \Psi(\mathbf{r}') \,. \tag{2.21}$$

Although many combinations of particle/hole and spin are possible to express Ψ and exist in the literature, here we choose the following 4-component spinor (and its corresponding Hermitian adjoint)

$$\Psi(\mathbf{r}) = \left[\psi_\uparrow(\mathbf{r}), \psi_\downarrow(\mathbf{r}), \psi_\uparrow^\dagger(\mathbf{r}), \psi_\downarrow^\dagger(\mathbf{r})\right]^T \,, \tag{2.22}$$

where $\psi_\alpha^\dagger(\mathbf{r})$ and $\psi_\alpha(\mathbf{r})$ are the field operators creating/annihilating an electron with spin α at lattice point $\mathbf{r}$. Here, the symbols $\hat{\cdot}$ and $\check{\cdot}$ describe the 2×2 and 4×4 matrices in spin and Nambu$\otimes$spin spaces respectively.
In Eq.(2.21), $\hat{H}$ is the normal-state Hamiltonian of the junction while $\hat{\Delta}$ describes the superconducting pairing potential. The former can be written as $\hat{H} = \hat{H}_s + \hat{H}_{FI}$, with $\hat{H}_s$ and $\hat{H}_{FI}$ referring to the S leads and FI barrier, respectively.
In Fig.2.6, the S regions extend for $j < 1$ and $j > L$. $\hat{H}_s$ consists in a kinetic term (i.e. $\hat{H}_s = \hat{H}_s^K$) that reads:

$$\begin{aligned} \hat{H}_s^K(\mathbf{r},\mathbf{r}') = &\{-t_s\left(\delta_{\mathbf{r},\mathbf{r}'+\mathbf{x}} + \delta_{\mathbf{r}+\mathbf{x},\mathbf{r}'}\right)\hat{\sigma}_0 \\ &- t_s\left(\delta_{\mathbf{r},\mathbf{r}'+\mathbf{y}} + \delta_{\mathbf{r}+\mathbf{y},\mathbf{r}'}\right)\hat{\sigma}_0 \\ &- (4t_s - \mu_s)\,\delta_{\mathbf{r},\mathbf{r}'}\hat{\sigma}_0\} \\ &\times \left[\Theta\left(-j+1\right) + \Theta\left(j - L\right)\right] \end{aligned} \tag{2.23}$$

where t_s and μ_s are the hopping parameter and the chemical potential, respectively, and Θ is the Heaviside step-function, defined as

$$\Theta(j) = \begin{cases} 1 & : j > 1 \\ 0 & : j \leq 0 \,, \end{cases} \tag{2.24}$$

Here and in the followings, we indicate with $\hat{\sigma}_0$ and $\hat{\sigma}_\nu$ $(\nu = 1, 2, 3)$ the unit and the Pauli matrices in the spin space, respectively.

In this work, we take the pairing potential $\hat{\Delta}$ different from zero only in the S leads, which, thus, vanishes inside the F barrier. Here, $\hat{\Delta}$ is of spin-singlet s-wave symmetry and is expressed as

$$\begin{aligned}\hat{\Delta}(\mathbf{r},\mathbf{r}') = {} & \Delta\delta_{\mathbf{r},\mathbf{r}'}\, i\,\hat{\sigma}_2 \\ & \times \left[\Theta\left(-j+1\right)e^{i\phi_L} + \Theta\left(j-L\right)e^{i\phi_R}\right],\end{aligned} \tag{2.25}$$

where $\phi = \phi_L - \phi_R$ defines the phase difference across the junction and ϕ_L (ϕ_R) is the phase in the left (right)-hand side superconductor. In our model, the order parameter Δ is constant in the leads and it is not derived from self-consistent calculations. Further, we assume that there is no disorder in the superconductors.

Let us now consider the ferromagnetic barrier of the junction. It extends from $j = 1$ to $j = L$ and its Hamiltonian consists of four terms

$$\hat{H}_{FI} = \hat{H}_{FI}^{K} + \hat{H}_{FI}^{SOC} + \hat{H}_{FI}^{ex} + \hat{H}_{FI}^{i}\,, \tag{2.26}$$

describing respectively:

- the kinetic part $\hat{H}_{FI}^{K}$, which includes the chemical potential and the tight-binding hopping along x and y directions

$$\begin{aligned}\hat{H}_{FI}^{K}(\mathbf{r},\mathbf{r}') = & \{-t_{FI}\left(\delta_{\mathbf{r},\mathbf{r}'+\mathbf{x}} + \delta_{\mathbf{r}+\mathbf{x},\mathbf{r}'}\right)\hat{\sigma}_0 \\ & - t_{FI}\left(\delta_{\mathbf{r},\mathbf{r}'+\mathbf{y}} + \delta_{\mathbf{r}+\mathbf{y},\mathbf{r}'}\right)\hat{\sigma}_0 \\ & - \left(4t_{FI} - \mu_{FI}\right)\delta_{\mathbf{r},\mathbf{r}'}\hat{\sigma}_0\} \\ & \times \Theta\left(j\right)\Theta\left(L+1-j\right),\end{aligned} \tag{2.27}$$

- the Rashba spin-orbit coupling $\hat{H}_{FI}^{SOC}$

$$\begin{aligned}\hat{H}_{FI}^{SOC}(\mathbf{r},\mathbf{r}') = i\alpha & \left[\left\{\delta_{\mathbf{r},\mathbf{r}'+\mathbf{x}} - \delta_{\mathbf{r}+\mathbf{x},\mathbf{r}'}\right\}\hat{\sigma}_2\right. \\ & \left. - \left\{\delta_{\mathbf{r},\mathbf{r}'+\mathbf{y}} - \delta_{\mathbf{r}+\mathbf{y},\mathbf{r}'}\right\}\hat{\sigma}_1\right]\Theta\left(j\right)\Theta\left(L+1-j\right),\end{aligned} \tag{2.28}$$

- the Zeeman exchange field $\hat{H}_{FI}^{ex}$

$$\hat{H}_{FI}^{ex}(\mathbf{r},\mathbf{r}') = -\mathbf{h}'\cdot\boldsymbol{\sigma}\delta_{\mathbf{r},\mathbf{r}'}\Theta\left(j\right)\Theta\left(L+1-j\right), \tag{2.29}$$

- the on-site random impurity potential $\hat{H}^{i}_{FI}$

$$\hat{H}^{i}_{FI}(\mathbf{r},\mathbf{r}') = v_{\mathbf{r}}\,\hat{\sigma}_0\,\delta_{\mathbf{r},\mathbf{r}'}\Theta\,(j)\,\Theta\,(L+1-j) \quad . \tag{2.30}$$

In the above equations, $\boldsymbol{\sigma}$ is the vector of the Pauli matrices $(\hat{\sigma}_1, \hat{\sigma}_2, \hat{\sigma}_3)$, t_{FI} is the hopping integral among nearest-neighbor lattice sites (in the followings we omit the subscript FI for simplicity, i.e. we take $t_{FI} = t$), μ_{FI} the Fermi energy, α the amplitude of the spin-orbit interaction, $v_{\mathbf{r}}$ the on-site random impurity potential strength, uniformly distributed in the range $-V_{imp} \leq v_{\mathbf{r}} \leq V_{imp}$. Finally, to represent a more realistic scenario in which the magnetization may be nonuniform in the whole barrier, the exchange field is assumed to be slightly disordered and is modeled as $\mathbf{h}' = \mathbf{h} + \delta_{\mathbf{h}}$, where $\delta_{\mathbf{h}}$ are small on-site fluctuations given randomly in the range $-h/10 \leq \delta_{\mathbf{h}} \leq h/10$ (along the $\mathbf{h}$-direction).
Moreover, in this work, since the junction plane coincides with the xy-plane, the exchange field $\mathbf{h}'$ is always taken in the perpendicular direction, $\mathbf{h}' = h'\mathbf{z}$ (along the z-direction).
In our model, the exchange field, the SOC and the impurity potential are defined only inside the ferromagnetic barrier. As we have seen in the previous chapter, the first two effects play a salient role in this discussion. In fact, due to the proximity effect at S/F interface, the presence of uniform exchange field provides the appearance of the short-range zero-spin triplet correlations (i.e. $|\uparrow\downarrow + \downarrow\uparrow\rangle$) in the barrier, while SOC induces spin-mixing effects and enables the LRTC with non-zero projection along the quantization axis of the ferromagnet (i.e. $|\uparrow\uparrow\rangle$, $|\downarrow\downarrow\rangle$). The presence of a random on-site impurity potential is needed if we want to simulate the transport properties of realistic "dirty" junctions. Indeed, these latter often represent a condition closer to real experimental systems.

2.2.1 Transport properties of the SFIS JJ

In this context, all the interesting transport properties of the SFIS JJ, such as the Josephson current flowing through the junction and the induced superconducting correlations, can be derived from the GF of the barrier. Its Matsubara representation is given by $\check{G}_{\omega_n}(\mathbf{r},\mathbf{r}')$, where $\mathbf{r} = j\mathbf{x}+m\mathbf{y}$ and $\mathbf{r}' = j'\mathbf{x}+m'\mathbf{y}$ run over all the possible lattice site indices $j, j' = 0, 1, \ldots, L, L+1$ and $m, m' = 1, \ldots, W$.
The barrier Matsubara GF is, thus, a $4WL\times4WL$ matrix in the Nambu$\otimes$spin space, whose blocks with fixed $(\mathbf{r}, \mathbf{r}')$ can be numerically calculated by solving the Gor'kov equation

$$\left[i\omega_n \hat{\tau}_0 \hat{\sigma}_0 - \sum_{\mathbf{r}_1} \begin{pmatrix} \hat{H}(\mathbf{r}, \mathbf{r}_1) & \hat{\Delta}(\mathbf{r}, \mathbf{r}_1) \\ -\hat{\Delta}^*(\mathbf{r}, \mathbf{r}_1) & -\hat{H}^*(\mathbf{r}, \mathbf{r}_1) \end{pmatrix} \right] \times \check{G}_{\omega_n}(\mathbf{r}_1, \mathbf{r}') = \hat{\tau}_0 \hat{\sigma}_0 \delta(\mathbf{r} - \mathbf{r}'), \tag{2.31}$$

where $\omega_n = (2n+1)\pi T$ is the fermionic Matsubara frequency and T is the temperature. Here and in the followings, $\hat{\tau}_0$ and $\hat{\tau}_\nu$ ($\nu = 1, 2, 3$) are the analogous of the unit and Pauli's matrices in the Nambu space, respectively. In order to get $\check{G}_{\omega_n}(\mathbf{r}, \mathbf{r}')$ we solve the Gor'kov Eq.(2.31) by applying the recursive RGF technique [89–91, 151–153] as described in the previous section. Thus we divide the 2D lattice along the $\mathbf{x}$-direction in transverse stripes, and recursively calculate the GF at each stripe of the barrier, starting from the two superconducting leads (see Appendix A for more details). Since we have L sites in the x-direction and W sites in the y-direction, we will have L stripes whose Hamiltonian and GF will be represented by $4W \times 4W$ matrices.

For this reason, we introduce the GF in Nambu⊗spin space $\check{G}_{j,j}$ of the stripe j along the x-direction inside the barrier. It is a $4W \times 4W$ matrix, where W is the number of lattice sites in each stripe. It can be visualized as a 2×2 block matrix in the Nambu space, where each block consists in a $2W \times 2W$ sub-matrix:

$$\check{G}_{j,j} = \check{G}_{\omega_n}(\mathbf{r}, \mathbf{r}') = \begin{bmatrix} \hat{G}_{\omega_n}(\mathbf{r}, \mathbf{r}') & \hat{F}_{\omega_n}(\mathbf{r}, \mathbf{r}') \\ -\hat{F}^*_{\omega_n}(\mathbf{r}, \mathbf{r}') & -\hat{G}^*_{\omega_n}(\mathbf{r}, \mathbf{r}') \end{bmatrix}, \tag{2.32}$$

where $\mathbf{r} = j\mathbf{x} + m\mathbf{y}$, $\mathbf{r}' = j\mathbf{x} + m'\mathbf{y}$ with j fixed. The off-diagonal terms of the matrix in the right-hand side of Eq.(2.32) are the so-called *anomalous Green's functions* $\hat{F}_{\omega_n}$, that describe the superconducting pair correlations. Notice that, here and in the following expressions, the 'checks' $\check{\ }$ indicate the full $4W \times 4W$ matrices in Nambu⊗spin space, whereas $\hat{\ }$ is used for $2W \times 2W$ matrices in the spin space.

To compute the GF of the whole barrier, we start from the surface GFs of the two superconducting leads S (which we will discuss in more detail in the next section), and recursively calculate the GF $\check{G}_{j,j}$ at each stripe j inside the F barrier by connecting it to the leads with the RGF technique.

The barrier stripes can be connected (to the leads and to each other) by using the hopping matrices $\check{T}^{\pm}$, given by

$$\check{T}^{\pm} = \begin{pmatrix} -t & \mp\alpha & 0 & 0 & \dots \\ \pm\alpha & -t & 0 & 0 & \dots \\ \dots & \dots & \dots & \dots & \dots \\ 0 & 0 & \dots & t & \pm\alpha \\ 0 & 0 & \dots & \mp\alpha & t \end{pmatrix}, \tag{2.33}$$

involving the hopping and spin-orbit coupling along the x-direction. Since we consider nearest-neighbors hopping, only adjacent stripes can be connected by the $\check{T}^{\pm}$ matrices (i.e. the j-th stripe is linked to the $j-1$-th and $j+1$-th).

At this point, we can thus specify the RGF method described in the previous section to our situation. We suppose that the *bare* Matsubara GF of each stripe j can be calculated as follows:

$$\check{G}^{0}_{j,j} = \left[i\omega_n \check{1} - \check{H}^{0}_{j,j} \right]^{-1} , \tag{2.34}$$

where $\check{H}^{0}_{j,j}$ is the Hamiltonian of the stripe, involving only couplings between lattice sites within the same stripe (i.e. $\hat{H}(\mathbf{r}, \mathbf{r}')$ with $\mathbf{r} = j\mathbf{x} + m\mathbf{y}$ and $\mathbf{r}' = j\mathbf{x} + m^{'}\mathbf{y}$ in Eq.(2.21)). Then we have to compute the *interacting* GF of the stripe j, $\check{G}_{j,j}$ in Eq.(2.32), which corresponds to the GF when it is connected to the two leads and to its nearest neighbors (i.e. $j-1$-th and $j+1$-th stripes). We observe that $\check{G}_{j,j}$ can be numerically computed by the means of a *Dyson-like* equation [89, 90, 152], starting from the surface GFs of the superconductors, which are supposed to be known. These latter are defined as $\check{G}^{L}_{0,0}(\omega_n)$ and $\check{G}^{R}_{L+1,L+1}(\omega_n)$ for the left and right S leads (respectively with $j = 0$ and $j = L + 1$ in Fig.2.6), and can be evaluated by applying the calculation method used in [89, 94].
Thus, by following the procedure illustrated in sec.2.1, we can construct $\check{G}_{j,j}$ once the recursive technique is applied both from the left and right directions, by using $\check{G}^{L}_{j,j}$ and $\check{G}^{R}_{j,j}$ which describe the stripe j when it is connected only to the left and right lead, respectively. Therefore, we can rewrite Eqs.(2.9), (2.12) in terms of the Matsubara GFs, obtaining

$$\check{G}^{L}_{j,j} = \left[i\omega_n \check{1} - \check{H}^{0}_{j,j} - \check{T}^{+}\check{G}^{L}_{j-1,j-1}\check{T}^{-} \right]^{-1} , \; 0 \leq j \leq L \tag{2.35}$$

$$\check{G}^{R}_{j,j} = \left[i\omega_n \check{1} - \check{H}^{0}_{j,j} - \check{T}^{-}\check{G}^{R}_{j+1,j+1}\check{T}^{+} \right]^{-1} , \; L+1 \leq j \leq 1 \, . \tag{2.36}$$

The above equations allow to calculate $\check{G}_{j,j}$ in Eq.(2.32), inside the barrier ($1 \leq j \leq L$) by using the formula

$$\check{G}_{j,j} = \left[i\omega_n \check{1} - \check{H}^{0}_{j,j} - \check{T}^{-}\check{G}^{R}_{j+1,j+1}\check{T}^{+} - \check{T}^{+}\check{G}^{L}_{j-1,j-1}\check{T}^{-} \right]^{-1} , \tag{2.37}$$

which is none other than Eq.(2.18) in the Matsubara representation.
Finally, by the relations adapted from Eqs.(2.19) and (2.20), we derive the GFs connecting two adjacent stripes (namely the stripe j with the ones at $j-1$ and $j+1$), $\check{G}_{j,j\pm1} = \check{G}_{\omega_n}(\mathbf{r}, \mathbf{r}' \pm \mathbf{x})$ and $\check{G}_{j\pm1,j} = \check{G}_{\omega_n}(\mathbf{r} \pm \mathbf{x}, \mathbf{r}')$ with $\mathbf{r} = j\mathbf{x} + m\mathbf{y}$, $\mathbf{r}' = j\mathbf{x} + m'\mathbf{y}$

$$\check{G}_{j,j+1} = \check{G}_{j,j}\,\check{T}^{-}_{j,j+1}\,\check{G}^{R}_{j+1,j+1}, \tag{2.38}$$
$$\check{G}_{j+1,j} = \check{G}^{R}_{j+1,j+1}\,\check{T}^{+}_{j+1,j}\,\check{G}_{j,j}, \tag{2.39}$$
$$\check{G}_{j,j-1} = \check{G}_{j,j}\,\check{T}^{+}_{j,j-1}\,\check{G}^{L}_{j-1,j-1}, \tag{2.40}$$
$$\check{G}_{j-1,j} = \check{G}^{L}_{j-1,j-1}\,\check{T}^{-}_{j-1,j}\,\check{G}_{j,j}\,. \tag{2.41}$$

In particular, the Josephson current, at finite temperature and given position j in F, can be computed from Eqs.(2.38) and (2.39), as follows

$$I(j) = -\frac{ie}{2}T\sum_{\omega_n} Tr\left[\hat{\tau}_3\check{T}_+\check{G}_{j,j+1} - \hat{\tau}_3\check{T}_-\check{G}_{j+1,j}\right], \tag{2.42}$$

where Tr stands for the trace over the Nambu⊗spin space. In the above equation, the summation over the Matsubara frequencies is performed. Furthermore, by taking the off-diagonal elements of $\check{G}_{j,j}$ in the right-hand side of Eq.(2.32), $\hat{F}_{\omega_n}(\mathbf{r},\mathbf{r}')$ with $\mathbf{r}=\mathbf{r}'=j\mathbf{x}+m\mathbf{y}$ (with j fixed), we can derive the four pairing components with s-wave symmetry at each stripe j along the $\mathbf{x}$-direction:

$$\frac{1}{W}\sum_{\omega_n}\sum_{m=1}^{W}\hat{F}_{\omega_n}(\mathbf{r},\mathbf{r}) = \sum_{\nu=0}^{3} f_\nu(j)\hat{\sigma}_\nu\; i\;\hat{\sigma}_2\;, \tag{2.43}$$

where f_0 is the spin-singlet component and f_ν with $\nu = 1,2,3$ are the spin-triplet components.

Analogous considerations can be applied to the GFs connecting the j-th stripe with its neighbors $j\pm 1$ (i.e. $\check{G}_{j,j\pm 1}$, $\check{G}_{j\pm 1,j}$, Eqs.(2.38)-(2.41)), from which we can calculate the odd-parity pairing functions:

$$\begin{aligned}\frac{1}{4W}\sum_{\omega_n}\sum_{m=1}^{W}&\hat{F}_{\omega_n}(\mathbf{r}+\mathbf{x},\mathbf{r})+\hat{F}_{\omega_n}(\mathbf{r},\mathbf{r}-\mathbf{x})\\ &-\hat{F}_{\omega_n}(\mathbf{r},\mathbf{r}+\mathbf{x})-\hat{F}_{\omega_n}(\mathbf{r}-\mathbf{x},\mathbf{r}) = \\ &\sum_{\nu=0}^{3} f_\nu\,(j)\,\hat{\sigma}_\nu\; i\;\hat{\sigma}_2\,,\end{aligned} \tag{2.44}$$

that give rise to p-wave superconductivity.

Making explicit the term in right hand side of Eqs.(2.43) (Eq.(2.44)), we can rewrite the s-wave (p-wave) pairing components as

$$\begin{cases} f_0 = \dfrac{f_{\uparrow\downarrow} - f_{\downarrow\uparrow}}{2} \\ \\ f_3 = \dfrac{f_{\uparrow\downarrow} + f_{\downarrow\uparrow}}{2} \\ \\ f_1 = \dfrac{f_{\downarrow\downarrow} - f_{\uparrow\uparrow}}{2} \\ \\ f_2 = \dfrac{f_{\uparrow\uparrow} + f_{\downarrow\downarrow}}{2\,i}, \end{cases} \tag{2.45}$$

from which we extract the standard spin correlation functions, f_0, f_3, $f_\uparrow$ (that is $f_{\uparrow\uparrow}$) and $f_\downarrow$ (that is $f_{\downarrow\downarrow}$).

2.3 Definition of the superconducting surface GFs

As we have mentioned, in order to apply the RGF technique to solve the Gor'kov Eq.(2.31) inside the barrier, we need to know as input GFs the *surface Green's functions* of the superconducting leads. As illustrated in Fig.2.6, in our system the barrier lies in the interval $1 \leq j \leq L$ and the superconducting leads in the intervals $j \leq 0$ and $j \geq L+1$. The left and right edge stripes are located, respectively, at $j = 0$ and $j = L+1$ and are described by the surface GFs $\check{G}_{0,0}(\omega_n)$ and $\check{G}_{L+1,L+1}(\omega_n)$ [89].
Since we assume that the order parameter is uniform and that there is no disorder in the superconductors, we "condense" all the semi-infinite two-dimensional superconducting leads in their edge stripes, thus calculating their surface GFs. In the following, we illustrate how these latter are calculated.
We start by considering the surface GFs of the S leads in the Nambu space, in the absence of exchange field and spin-orbit interaction [89]. Then we will generalize our results to Nambu $\otimes$ spin space when considering the ferromagnetic barrier in the presence of SOC.
Let us indicate with $\check{G}_{k,k'}(\omega_n, 0, 0)$ and $\check{G}_{k,k'}(\omega_n, L+1, L+1)$ the GFs matrices describing the particle propagation between sites k and k', respectively in the left and right superconducting lead stripe, with $k, k' = 1, \ldots, W$. Therefore, by following Ref. [89], the left and right surface GFs have the following structure in the Nambu space

$$G_{(k,k')}\left(\omega_n, 0, 0\right) = \sum_{m=1}^{W} \frac{e^{ip_m^+}}{t\,\Omega_n\left(W+1\right)} \sin\left(q_m k\right) \sin\left(q_m k'\right)$$

$$\times \begin{pmatrix} \Omega_1 & -i\,\Delta \\ -i\,\Delta & \Omega_2 \end{pmatrix}$$

$$- \sum_{m=1}^{W} \frac{e^{-ip_m^-}}{t\,\Omega_n\,(W+1)} \sin(q_m k) \sin\left(q_m k'\right) \tag{2.46}$$

$$\times \begin{pmatrix} \Omega_2 & -i\,\Delta \\ -i\,\Delta & \Omega_1 \end{pmatrix}$$

and

$$G_{(k,k')}\left(\omega_n, L+1, L+1\right) = \sum_{m=1}^{W} \frac{e^{ip_m^+}}{t\,\Omega_n\,(W+1)} \sin(q_m k) \sin\left(q_m k'\right)$$

$$\times \begin{pmatrix} \Omega_1 & -i\,\Delta\,e^{i\phi} \\ -i\,\Delta\,e^{-i\phi} & \Omega_2 \end{pmatrix}$$

$$- \sum_{m=1}^{W} \frac{e^{-ip_m^-}}{t\,\Omega_n\,(W+1)} \sin(q_m k) \sin\left(q_m k'\right) \tag{2.47}$$

$$\times \begin{pmatrix} \Omega_2 & -i\,\Delta\,e^{i\phi} \\ -i\,\Delta\,e^{-i\phi} & \Omega_1 \end{pmatrix},$$

where ϕ is the phase difference between the two superconductors and we have defined

$$\Omega_{1,2} = \mp\Omega_n - \omega_n \tag{2.48}$$

$$\Omega_n = \sqrt{\omega_n^2 + \Delta^2} \tag{2.49}$$

$$q_m = \frac{m\pi}{W+1} \tag{2.50}$$

$$p_m^{\pm} = \arccos\left[-\frac{1}{2t}\left(\mu + 2t\cos q_m \pm i\,\Omega_n\right)\right], \tag{2.51}$$

with the conditions: $\mathrm{Im}\{(p^+)\} > 0$ and $\mathrm{Im}\{(p^-)\} < 0$. Note that q_m are the eigenvalues of the wave number labelling the eigenfunctions along the y-direction (with $m = 1, \ldots, W$), resulting from using the hard-wall boundary conditions in the y-direction [94].

At this point, we can generalize the above equations to the case including the spin-mixing effect due to SOC. Thus, for every couple of indices (k, k') within the S lead stripe, we can obtain the GF matrices in the Nambu $\otimes$ spin space, by considering the following 4×4 matrices substitution in the left and right lead, respectively

$$\check{G}_{k,k'}(\omega_n, 0, 0) \longrightarrow \begin{array}{c c} & \begin{array}{cccc} c_{k\uparrow} & c_{k'\downarrow} & c^\dagger_{k\uparrow} & c^\dagger_{k'\downarrow} \end{array} \\ \begin{array}{c} c^\dagger_{k\uparrow} \\ c^\dagger_{k'\downarrow} \\ c_{k\uparrow} \\ c_{k'\downarrow} \end{array} & \begin{pmatrix} \Omega_1 & 0 & 0 & \Delta \\ 0 & -\Omega_2^* & -\Delta^* & 0 \\ 0 & -\Delta^* & -\Omega_1^* & 0 \\ \Delta & 0 & 0 & \Omega_2 \end{pmatrix} \end{array} \tag{2.52}$$

and

$$\check{G}_{k,k'}(\omega_n, L+1, L+1) \longrightarrow \begin{array}{c c} & \begin{array}{cccc} c_{k\uparrow} & c_{k'\downarrow} & c^\dagger_{k'\uparrow} & c^\dagger_{k'\downarrow} \end{array} \\ \begin{array}{c} c^\dagger_{k\uparrow} \\ c^\dagger_{k'\downarrow} \\ c_{k\uparrow} \\ c_{k'\downarrow} \end{array} & \begin{pmatrix} \Omega_1 & 0 & 0 & \Delta\, e^{i\,\phi} \\ 0 & -\Omega_2^* & -\Delta^*\, e^{i\,\phi} & 0 \\ 0 & -\Delta^*\, e^{-i\,\phi} & -\Omega_1^* & 0 \\ \Delta\, e^{-i\,\phi} & 0 & 0 & \Omega_2 \end{pmatrix} \end{array}.$$

Essentially, for each couple of fixed indices (k, k') we have a 4×4 matrix in the Nambu $\otimes$ spin space, which presents a block structure, as illustrated in Fig.2.7 (a), describing the electron-hole processes $(G, -G^\dagger)$ and Cooper pair correlations $(F, -F^\dagger)$. Therefore, in the basis chosen to describe our system, every stripe (considering both the superconducting leads and barrier) has a well defined matrix structure, as shown in Appendix A (Fig.2), where we explained in detail the process of dividing the system in stripes. Thus, for the construction of the surface GFs of the S leads, we have to recover such matrix form, rearranging the various blocks composing the different GF matrices with (k, k') fixed.
Let us consider, for example, the left S lead surface stripe with only two

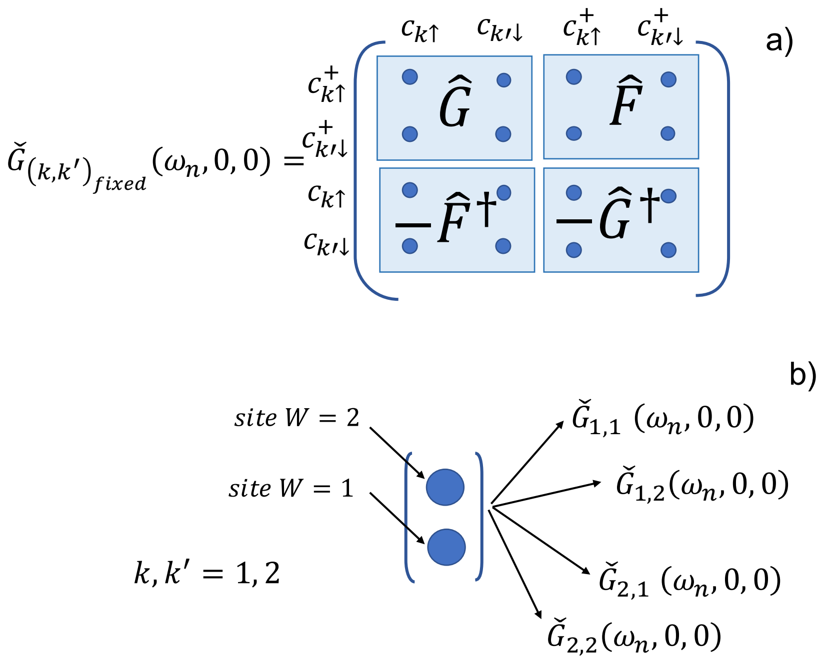

Figure 2.7: (a): Schematic representation of GF matrix structure for fixed (k, k') within the left S stripe, in the Nambu $\otimes$ spin space. In (b) we illustrate the possible four different propagators $\check{G}_{k,k'}$ that we obtain in the case of a stripe with only two sites ($W = 2$), needed for the construction of the surface GF.

sites in the y-direction, $W = 2$. In this case, the indices (k, k') run from 1 to 2. Thus, in principle, we find four different 4×4 matrices in the Nambu $\otimes$ spin space (Fig.2.7 (b)), describing the propagation between the sites k and k' within the left S stripe: $\check{G}_{1,1}(\omega_n, 0, 0)$, $\check{G}_{1,2}(\omega_n, 0, 0)$, $\check{G}_{2,1}(\omega_n, 0, 0)$, $\check{G}_{2,2}(\omega_n, 0, 0)$, where each of them has the matrix structure illustrated in Fig.2.7 (a). Therefore, we can reconstruct the whole stripe matrix of the left surface GF by separating each block $\check{G}_{k,k'}(\omega_n, 0, 0)$ in four blocks $(\hat{G}, \hat{F}, -\hat{F}^\dagger, -\hat{G}^\dagger)$ and then, rearranging them as in Fig.2.8.
The same procedure can be applied for the calculation of the right lead surface GF, $\check{G}_{L+1,L+1}(\omega_n)$. Consequently, by generalizing this process to W-sites stripes, we obtain the leads GFs ready to use as the starting input in the recursive algorithm of the RGF technique.

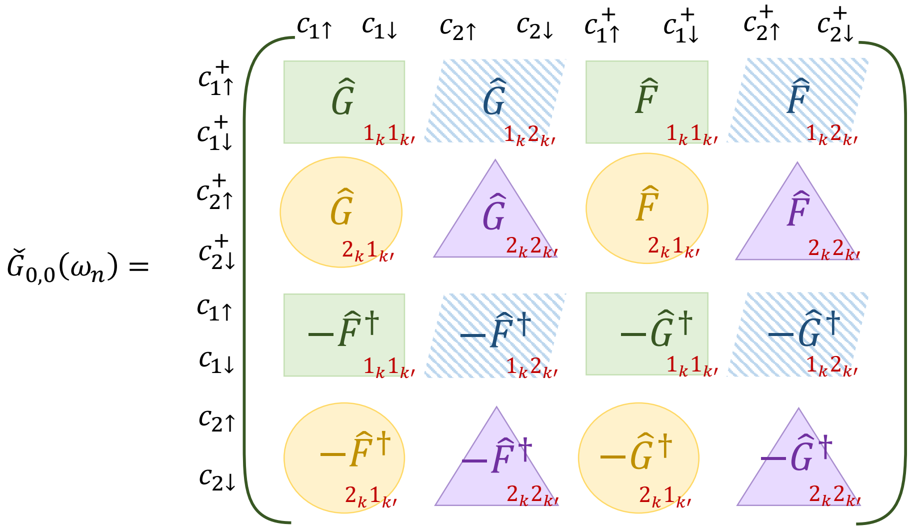

Figure 2.8: Schematic representation of the left S surface GF matrix structure (for $W = 2$), in the Nambu $\otimes$ spin space.

Chapter 3

Realization of 0-π states in SFIS JJs: the role of spin-orbit interaction and lattice impurities

The interest in proximity structures made of superconducting and ferromagnetic layers in contact with each other, such as Josephson devices with ferromagnetic barrier, has been recently renewed due to their potential applications to superconducting spintronics [47, 86, 87, 155] and to quantum computing [36, 79]. However, much less is known when the ferromagnetic layer is insulating.
In this chapter we aim to investigate, from a purely theoretical point of view, the transport properties of SFIS junctions with particular attention paid to the temperature behavior of the critical current, $I_c(T)$, that may be used as a fingerprint of the junction. Specifically, we theoretically study the role that impurities and spin-mixing mechanisms due to the SOC may have on the appearance of the 0 and π phases, as well as on the controlled switching between these two states.
Moreover, to enrich and complete our analysis we also calculate the correlation functions in these SFIS JJs in the presence of SOC and impurities, for s-wave and p-wave symmetries, recovering both the long and short range pairing components.
This chapter is inspired by the work presented in Ref. [148] and is organized as follows.
In the first section, we briefly recall the 2D BdG model Hamiltonian and the RGF approach presented in detail in Chapter 2, used to describe the SFIS JJ and calculate currents and correlation functions. Thus we report the main model parameters used in the simulations. Then, we consider the clean regime and discuss the appearance of the 0 and π states, firstly by

varying the exchange field strength and, secondly, by adding the SOC, analyzing how these two effects influence the $I_c(T)$ behavior. Subsequently, we show a detailed investigation on the critical current in the presence of lattice impurities and their effect, combined with the SOC, on the switching between 0, 0-π, and π regimes. At last, we present the correlation functions calculated in these systems.

3.1 Introduction

As we introduced in Chapter 1, the supercurrent flowing across a JJ is usually described by the sinusoidal relation $I = I_c \sin\varphi$, where I_c is the critical current and φ the phase difference between superconductors. In conventional JJs the ground state occurs at $\varphi = 0$ ($I_c > 0$), by contrast in π junctions the minimum energy corresponds to $\varphi = \pi$ ($I_c < 0$).
According to the literature, SFS JJs are promising platforms to implement π junctions [15, 17, 19, 28]. Indeed, as a consequence of the phase change of the Cooper pair wave function which extends from S to F layer due to the proximity effect, they show an oscillating behavior of the critical current as a function of the length of the F region [26, 27], thus providing the necessary sign change of I_c to switch from 0 to π. The so-called π JJs are currently subject to intense research activity due to their applicability as architectural elements for the development and the improvement of nanostructures, since they are considered to be very promising ingredients to engineer superconducting circuits, nanoelectronics, spintronics and quantum computing devices [36–38]. Among these applications, for example, we can mention the possible integration of such π junctions in quantum circuits for superconducting qubits, considered quite promising due to increased robustness against noise and electromagnetic interference induced by magnetic field sources and a more compact and simple design, opening the way to scalable devices [39, 40, 78–81].
The 0-π transitions between the 0 and the π state have been experimentally measured in SFS JJs by varying the thickness of the ferromagnet in different kinds of samples [34, 131, 156] or the temperature [30, 35, 157]. In particular, the temperature induced 0-π crossover is characterized by a peculiar cusp in the $I_c(T)$ behavior at the transition temperature, giving the first chance to realize both the 0 and π state in a single device. However, since SFS JJs are affected by dissipation effects due to their coupling to the environment [58, 59], JJs with a nonmetallic barrier result to be a good option for obtaining 0-π transitions and π states. Indeed, these systems show features similar to SFS JJs with the advantage of having a less dissipative nature which makes ferromagnetic insulator JJs well suited for these kinds of applications. As a matter of fact, transport properties through SFIS JJs have been investigated both theoretically [63, 82] and experimentally [66], display-

ing temperature induced 0-π transitions together with unconventional $I_c(T)$ behaviors [67,68]. Therefore, the possibility to arrange an equilibrium superconducting phase difference of π across JJ has been theoretically predicted also in this case [69, 82].

In this intriguing scenario, one of the most challenging issues is to find an effective way of controlling the occurrence of 0-π transitions in SFIS JJs, through a direct action on their $I_c(T)$ behavior, which is one of the main quantities reachable experimentally.

It is well known that tuning the exchange field of the barrier is an available technique to manipulate the critical current [68], thus driving the switching between 0, 0-π and π regimes. However, this approach does not provide an easy engineering of ferromagnetic JJs based devices, since the exchange field is an intrinsic property of the magnetic barrier and experimental procedures required for its manipulation may induce decoherence and magnetic noise. For this reason, it would be extremely useful to find alternative and more accessible mechanisms that can be exploited to drive the 0-π transition in such devices. In this context, we recognize spin-mixing effects (SOC) and lattice impurities as good tools that offer the possibility to control the tuning of 0-π transitions in SFIS JJs. Spin-orbit coupling (SOC) [136, 158–166] has already been studied as a source of intriguing anomalous Josephson effect [167–175]. Moreover, it has been investigated in previous works [90] to induce the $\pi - 0$ transition in SFS JJs. However a thorough study of the SOC effect on the $I_c(T)$ behavior in these $0 - \pi$ junctions is lacking. On the other hand, while previous works investigated the $0 - \pi$ transition induced in SIS JJs by magnetic impurities [29, 176–178], the chance of controlling the $0 - \pi$ transition by means of lattice non-magnetic impurities is not yet well explored.

Here, we present how the interplay between SOC and nonmagnetic disorder may be exploited for the engineering of fully tunable 0-π JJs which can be switched between the 0, 0-π and π regimes.

Furthermore, since S/F hybrid systems are presumed to host triplet superconductivity induced by the proximity effect [15, 17, 19, 41–43], as a supplementary analysis we also calculate the correlation functions in these SFIS JJs in the presence of SOC and impurities, both for s-wave and p-wave symmetry. Indeed, in addition to the short-range singlet and triplet pairings with total spin projection $S_z = 0$, in our system we also find the equal spin-triplet long-range correlation pairs with total spin projection $S_z = \pm 1$ in the direction of the exchange field due to the presence of SOC, which allows the spin symmetry breaking at S/FI interfaces. In particular, we show that intensifying the impurities strength results in an enhancement of the odd-frequency correlations (i.e., s-wave equal-spin triplet and p-wave singlet, respectively). Therefore, we identify SFIS JJs as sources of unconventional odd-frequency superconductivity and equal-spin triplet pairings when spin-mixing and disorder effects are involved [19, 41–43, 90, 143, 179–181].

3.2 Formalism and model parameters

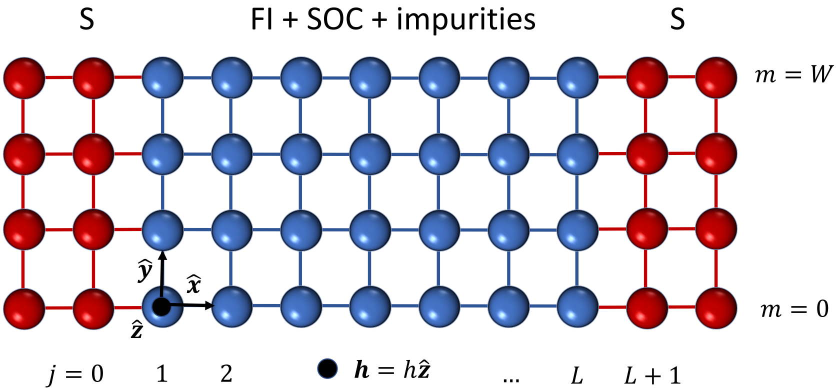

Figure 3.1: Schematic representation of the SFIS junction geometry with a ferromagnetic insulator barrier in the presence of SOC and impurities. The exchange field **h** is taken parallel to the z-axis, thus perpendicular to the junction plane (i.e., the xy-plane).

We study the Josephson effect in SFIS JJs by using the numerical calculation method based on the RGF technique [89–91] presented in Chapter 2. We describe the junction by using the 2D Bogolioubov de Gennes (BdG) tight-binding model [68,89–91] shown in Fig.3.1. As we have seen, the normal-state Hamiltonian of the junction $\hat{H} = \hat{H}_s + \hat{H}_{FI}$, can be separated in two parts referring to the S leads and FI barrier, respectively. In $\hat{H}_{FI}$ we include all the interactions present in the barrier, namely the exchange field, SOC and lattice impurities, described by the corresponding terms and parameters, as defined in Chapter 2.

The Josephson current at finite temperature T is derived from the Matsubara GF of the FI barrier, calculated with the RGF technique, whose application requires to divide the 2D lattice in transverse stripes labeled by the index j. Thus, remembering that we indicate with $\check{\ }$ the full $4W \times 4W$ matrix in Nambu $\otimes$ spin space, the barrier GF $\check{G}_{j,j}$ of the stripe j-th along the x-direction solves the Gor'kov equation Eq.(2.31). Therefore, the Josephson current $I(j)$ originates from the GFs connecting two adjacent stripes (namely the j-th and $j+1$-th), $\check{G}_{j,j+1}$ and $\check{G}_{j+1,j}$, and reads

$$I(j) = -\frac{ie}{2} T \sum_{\omega_n} Tr\left[\hat{\tau}_3 \check{T}_+ \check{G}_{j,j+1} - \hat{\tau}_3 \check{T}_- \check{G}_{j+1,j}\right], \tag{3.1}$$

where Tr stands for the trace over the Nambu $\otimes$ spin space and we consider that the different neighbor stripes composing the system are connected by

the $\check{T}^{\pm}$ matrices defined by Eq.(2.33).
Lastly, the s- and p-wave correlation functions at each stripe j along the x-direction are extracted from the anomalous GF $\hat{F}_{\omega_n}$ by using Eqs.(2.43) and (2.44), respectively, that we report here by making explicit the right-hand side for convenience

$$\frac{1}{W}\sum_{\omega_n}\sum_{m=1}^{W}\hat{F}_{\omega_n}(\mathbf{r},\mathbf{r}) = \begin{pmatrix} -f_1+if_2 & f_0+f_3 \\ -f_0+f_3 & f_1+if_2 \end{pmatrix}\,, \tag{3.2}$$

and

$$\begin{aligned} &\frac{1}{4W}\sum_{\omega_n}\sum_{m=1}^{W}\hat{F}_{\omega_n}(\mathbf{r}+\mathbf{x},\mathbf{r})+\hat{F}_{\omega_n}(\mathbf{r},\mathbf{r}-\mathbf{x}) \\ -\hat{F}_{\omega_n}(\mathbf{r},\mathbf{r}+\mathbf{x})-\hat{F}_{\omega_n}(\mathbf{r}-\mathbf{x},\mathbf{r}) &= \begin{pmatrix} -f_1+if_2 & f_0+f_3 \\ -f_0+f_3 & f_1+if_2 \end{pmatrix}\,. \end{aligned} \tag{3.3}$$

where the vector $\mathbf{r} = j\mathbf{x} + m\mathbf{y}$ points a lattice position. The above equations allow to obtain the four paring components: f_0, f_3 (short-range spin singlet and triplet pairings with $S_z = 0$), $f_\uparrow$, $f_\downarrow$ (long-range spin triplets with $S_z = \pm 1$, obtained as linear combination of f_1 and f_2).
Here, we report the choice of the model parameters used for all the results discussed in the following. Henceforth, we adopt units with $\hbar = c = k_B = 1$, where c is the speed of light and k_B is the Boltzmann constant.
All the energies are, thus, scaled by t and the magnitude of the spin-orbit coupling α is scaled by ta, where the lattice constant is set $a = 1$, while the Josephson current is calculated in units of $I_0 = e\Delta$.
We recall here that we denote with L and W the length and width of the barrier, while SOC, exchange field and impurity potential strength are respectively described through the parameters α, h and V_{imp}.
Further, we fix several parameters as: the barrier width $W = 32$ sites in the y direction, the FI and superconductors hoppings $t_s = t = 1$, the chemical potentials $\mu_{FI} = 0$, $\mu_s = 3$, and the order parameter $\Delta = 0.005$. In particular, the chosen chemical potential mismatch at FI and S interfaces allows to describe the insulating regime in our model. Finally, the exchange field is assumed to be slightly disordered and is modeled as $\mathbf{h}' = \mathbf{h} + \delta_{\mathbf{h}}$, where $\delta_{\mathbf{h}}$ are small on-site fluctuations given randomly in the range $-h/10 \le \delta_h \le h/10$ (along the $\mathbf{h}$-direction). Here, $\mathbf{h}'$ is taken parallel to the z-axis, thus perpendicular to the junction plane (i.e., the xy-plane). In the numerical simulations, both the temperature dependence of the critical Josephson current (i.e. $I_c(T)$) and correlations functions are averaged over N_s samples with different random impurity configurations. We choose $N_s = 80 - 100$ for the $I_c(T)$ curves and $N_s = 300$ for the pairing correlation functions. In particular, the ensemble average of the Josephson current (Eq.(2.42)) over

a number of different samples is obtained as: $< I >= \frac{1}{N_s}\sum_{n=1}^{N_s} I_n$, where I_n is the Josephson current in the n-th sample. Then, evaluating the average Josephson current by varying ϕ in the range from 0 to π we obtain the average current-phase relation (CPR) at fixed T (i.e. $I(\phi, T)$). Finally, the averaged critical current $I_c(T)$ is estimated from the CPR at different temperatures between 0 and T_c, by taking its maximum in absolute value ($I_c(T) = \max_\phi[|I(\phi, T)|]$). In this work, each $I_c(T)$ curve together with the corresponding CPRs ($I(\phi, T)$) has been normalized to the maximum value of the critical current with respect to the temperature, i.e. $I_{max} = \max_T[I_c(T)]$.

3.3 Tuning of 0, 0-π and π regimes in SFIS JJs in the clean limit, by varying the exchange field h

To begin with, first of all, in this section we want to illustrate that, as reported in the literature [30, 34, 35, 131, 156, 157], it is possible to switch between the 0, 0-π and π regimes in SFIS JJs by varying the exchange field. This is reflected in particular features of the $I_c(T)$ behavior, such as the presence of a peculiar cusp at the transition temperature ($T_{0-\pi}$) in temperature induced 0-π transitions, which we can observe by varying the corresponding parameter h in our model. In this part, we consider a clean situation, in which both lattice impurities and small exchange field fluctuations in the FI barrier are absent ($V_{imp} = 0$, $\delta_h = 0$). Furthermore, here and in the following, we consider the short junction regime, typical of tunnel junctions, where the length of the FI barrier is fixed at $L = 8$ sites in the x direction, unless otherwise specified.

Thus, in Fig.3.2 (a) we show the temperature dependence of the critical current, obtained for increasing values of h in the clean limit. For these simulations we fixed the SOC strength $\alpha = 0.04$. All the other parameters are the same as those defined in the previous section 3.2. As we can see, the non-monotonic dependence of $I_c(T)$ is visible. In particular, we can notice that, starting from the Ambegaokar-Baratoff (AB) [182] type behavior ($h = 0.10$, red curve), I_c is strongly modified with increasing the exchange field h in the ferromagnetic layer, causing the system to move towards 0-π and π regimes. Then, undergoing some oscillations, the AB trend is established again when h increases ($h = 0.60$, blue curve). Moreover, the cusp-minimum of the 0-π transition appears to be shifted in temperature as h varies. We also report in Figs.3.2 (b-d) the current-phase relation (CPR) corresponding to the $I_c(T)$ curves obtained for $h = 0.10, 0.25, 0.40$, respectively. As can be seen, the AB-type curves shown in (a) correspond to pure 0 (b) and π (d) JJs, stable over the whole range of temperatures.

Specifically, it is worth noting that varying h significantly influences the $I_c(T)$ behavior of these systems, producing an even more considerable effect in the short junction regime, namely the situation we are considering in this thesis. For this reason, manipulating the exchange field of the barrier is effectively a difficult operation to manage experimentally. Conversely, as we will see in the next sections, the 0, 0-π and π switching can be more easily attained by acting on the SOC and nonmagnetic impurities.

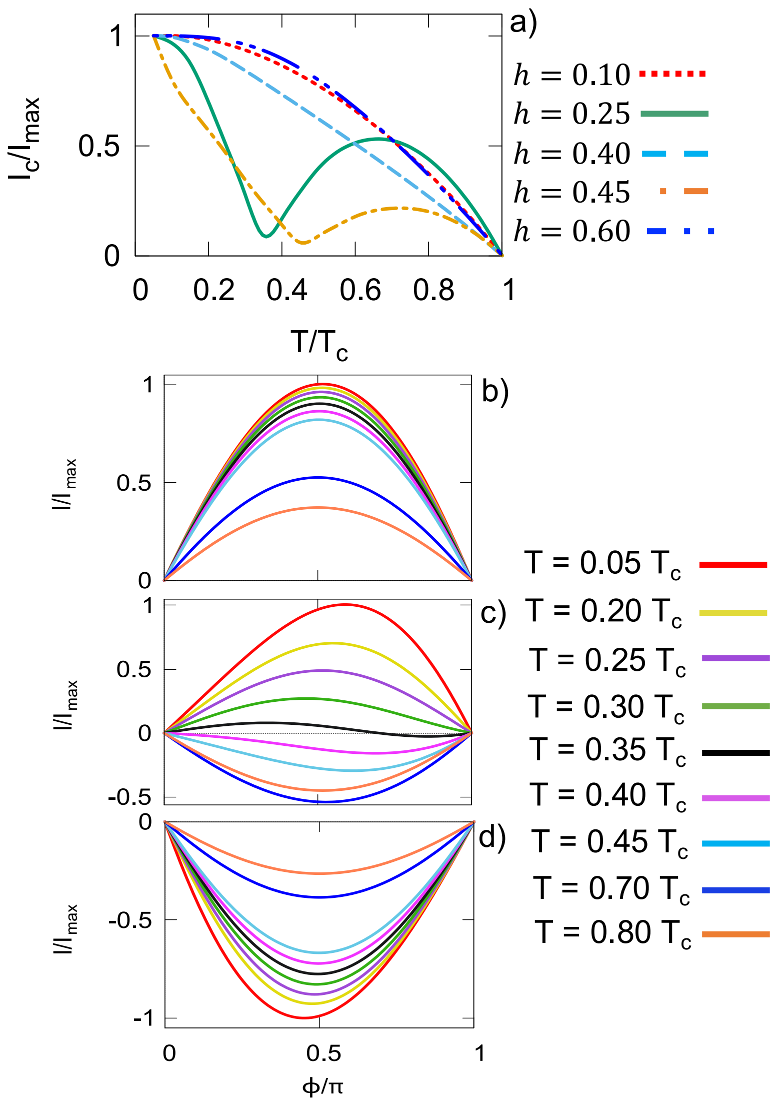

Figure 3.2: (a): $I_c(T)$ for different values of h. For these simulations we used $\alpha = 0.04$, $L = 8$ and $W = 32$ sites in the x and y direction. CPR, at selected temperatures, of a 0 (b), 0-π (c) and π (d) JJ, obtained for $h = 0.10$, 0.25, 0.40, respectively.

3.4 The role of spin-orbit coupling (SOC) on the switching between 0 and π state in the clean limit

In this section, we consider the case of SFIS JJ which presents temperature induced 0-π transitions and analyze the effect of SOC on its $I_c(T)$ behavior. As in the previous section, we still look at a clean situation with a uniform distribution of the exchange field in the 2D lattice ($V_{imp} = 0$, $\delta_h = 0$).
All the results discussed in the following are obtained with the model parameter describing the exchange field fixed at $h = 0.45$.
In Fig.3.3 (a) we can see that, starting from a 0-π transition corresponding to $\alpha = 0$, we recover the AB behavior for $\alpha = 0.20$. For larger α the critical current is always of AB type. We can also notice that the second lobe of the $I_c(T)$ curve is reduced in height and its (cusp-like) minimum is shifted toward higher temperatures when α increases, until the $I_c(T)$ behavior visibly changes and it completely disappears in the AB regime. In Figs.3.3 (b-d), the characteristic CPRs corresponding to $I_c(T)$ curves for $\alpha = 0$, 0.07, 0.20 are shown. We can notice that the 0-π transition is well evident for $\alpha = 0$ and only slightly appreciable for $\alpha = 0.07$, while it is completely washed out for $\alpha = 0.20$. Hence, by increasing α, we induce a shift in the transition temperature $T_{0-\pi}$ towards higher values, until the 0-π transition cancels out. Further, we observe visible contributions due to the second and higher order harmonics in the CPRs at $T_{0-\pi}$, when the first order harmonic appears strongly weakened [183, 184]. Our results confirm the fact that SOC stabilizes the 0 state rather than the π state [90] in these devices.
To better illustrate this mechanism, in Fig.3.4 we show the critical Josephson current as a function of the length of the ferromagnetic-insulator layer (with L from $L = 3$ to $L = 50$), i.e. current-length relation (CLR). In these simulations we used $T = 0.1T_c$ and $\phi = \pi/2$. Furthermore, we set $h = 0.45$ and $\alpha = 0, 0.07, 0.20$.
The change in sign of Josephson current, indicating the corresponding 0-π transitions at fixed lengths of the FI layer due to the presence of the exchange potential, is more frequent in the cases with $\alpha = 0$ and $\alpha = 0.07$. The effect of SOC increasing is the suppression of the above-mentioned 0-π transitions and consequently a mostly always positive Josephson current for $\alpha = 0.20$. Indeed, the SOC produces a shift of the CLR curve from lower to higher current values; negative critical currents are representative of π states while, when I_c becomes positive (at fixed length L), the $\pi - 0$ transition occurred and the system reaches the 0 final-state under the SOC growth. Taking h and L fixed, there is no possibility that, by further increasing α, the system will return to the π state experiencing another 0-π transition.
We can provide a qualitative explanation of this effect as follows. As we have seen in Chapter 1, the short-range spin-triplet component $S_z = 0$ appears

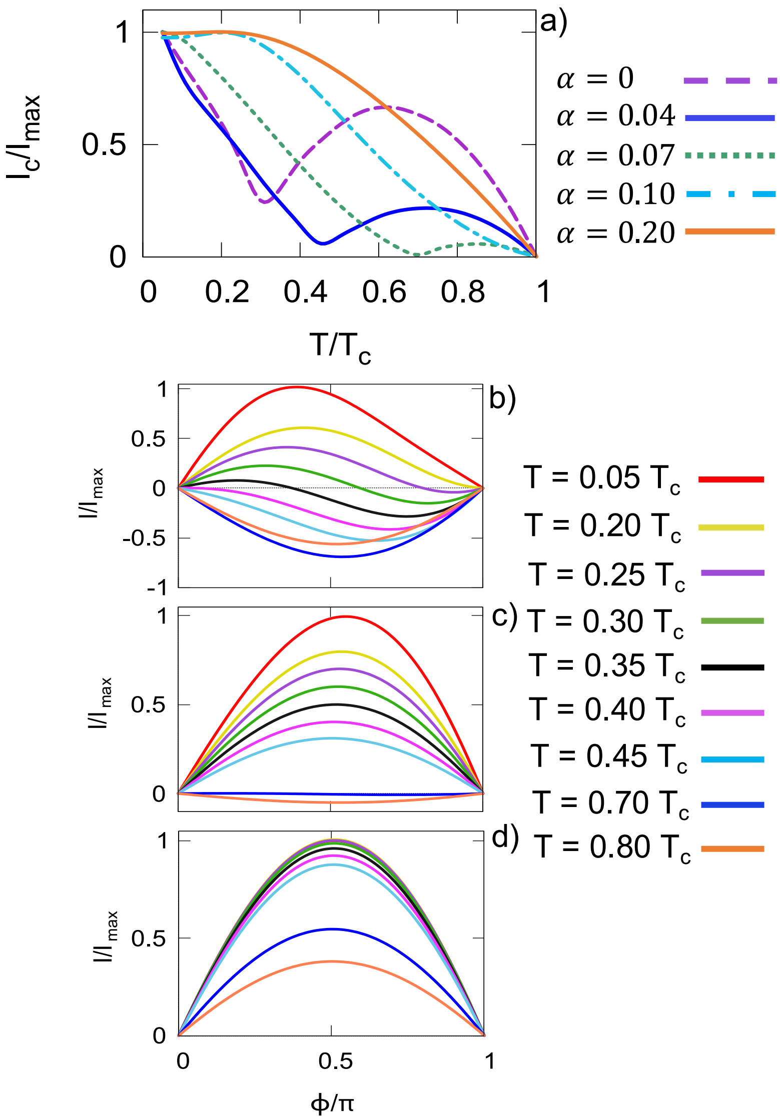

Figure 3.3: Effect of SOC increasing on the $I_c(T)$ (a). We set the exchange field $h = 0.45$, while the dimensions of the lattice are $L = 8$ and $W = 32$, along the x and y-direction, respectively. In (b-d), the CPRs, at selected temperatures, relative to the simulations in (a) for $\alpha = 0, 0.07, 0.2$ are shown.

in S/FI systems due to exchange field breaking time-reversal symmetry in the F layer. In the presence of spin-orbit interaction, the spin-mixing effect at S/FI interfaces allows for long-range equal spin-triplet components $S_z = \pm 1$ inside the ferromagnetic region. The $S_z = 0$ components (singlet and zero-spin triplet) show an oscillating behavior due to the different phase

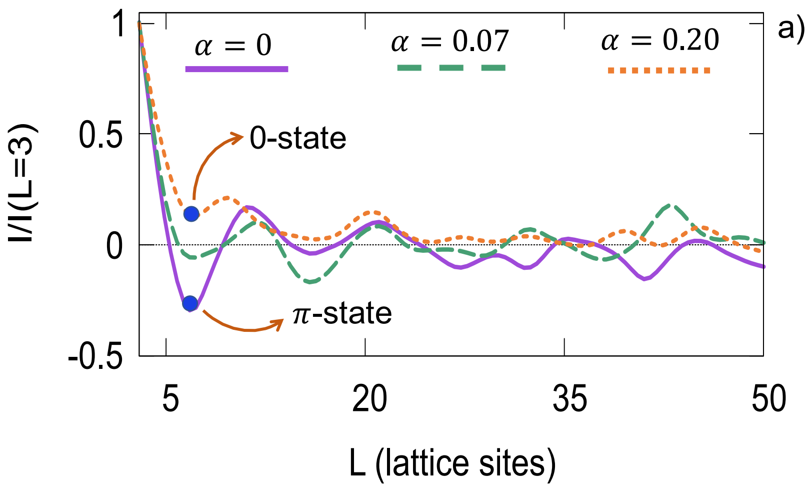

Figure 3.4: CLR computed by varying the length of the junction from $L = 3$ to $L = 50$, with $\phi = \pi/2$, $T = 0.1T_c$ and $W = 32$, for $\alpha = 0, 0.07, 0.2$. The CLR curves are normalized to the value of their current at $L = 3$.

shifts acquired by the up and down-spin electrons of the Cooper pair, as they propagate in F, while the $S_z = \pm 1$ pairing components show a long-range decay, since the exchange field h has the same effect on the two equal spin electrons [19, 26, 27, 185]. In the long junction limit all the pairing functions decay exponentially over the temperature dependent coherence length $\xi_{f1} = \frac{v_F}{2\pi T}$, whereas the oscillation period of the zero-spin pairing components is given by $\xi_{f2} = \frac{v_F}{2h}$ [15, 41, 42, 90]. Therefore, for $x >> \xi_{f1}$, heuristically, the Josephson current can be considered as consisting of two contributions:

$$I \sim I_{S_{z=\pm 1}} \, e^{-x/\xi_{f1}} + I_{S_{z=0}} \, e^{-x/\xi_{f1}} \, \cos\left(\frac{x}{\xi_{f2}}\right) ,$$

where $I_{S_{z=0}}$ and $I_{S_{z=\pm 1}}$ are the amplitudes of the opposite spin and parallel spin components, respectively. Increasing the SOC results in an enhancement of the non-oscillating part of the Josephson current, whose superposition with the oscillating term produces, in turn, an enlarged total current and, thus, may prevent that I_c vanishes in the 0-π transition.

To complete our analysis in the presence of SOC in the FI barrier and illustrate what we explained in terms of the $I_c(T)$ behavior, in Fig.3.5 we additionally report the density plot of Josephson current, calculated at $T = 0.1T_c$ and $\phi = \pi/2$, as a function of the exchange field h and SOC strength, α, for a wider range of these latter parameters. The black/dark-violet regions indicate negative values of the current, where the JJ is π. In particular, we can notice a well-defined π-*island* that in our simulations appear stable in

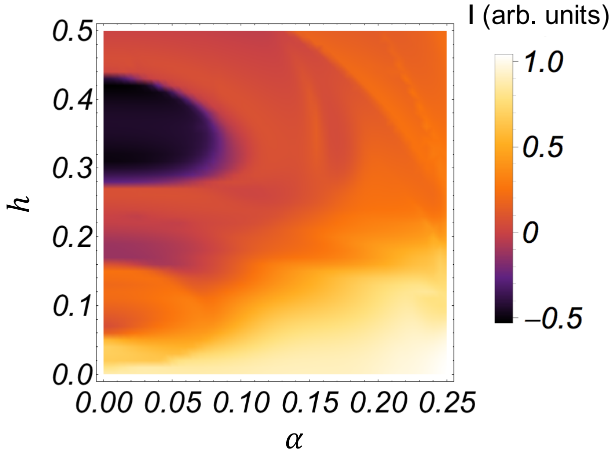

Figure 3.5: Josephson current, calculated at $T = 0.1T_c$ and $\phi = \pi/2$, as a function of the exchange field h and SOC strength α, for a wider range of these latter parameters.

temperature. The white/light-yellow regions, where $I > 0$, indicate conventional 0 JJs, with a mostly constant occurrence at low values of the exchange field ($h < 0.05$) for any value of α. Intermediate orange-red areas represent JJs which show a good probability to undergo a 0-π transition, since the critical current is very low. Our outcomes, obtained for SFIS JJs, are in accordance and extend those previously demonstrated in [90,91] in the case of SFS JJs in the non-insulating regime.
In conclusion, we can claim that our results lead to regarding SOC as a useful tool for driving the evolution of the $I_c(T)$ of SFIS JJs from 0-π to 0 regime.

3.5 The dirty regime: the role of lattice impurities in the formation of π JJs

At this point, it become legitimate to ask under which conditions the junction displays a stable π state over the whole temperature range, similar to what happens in the case of the 0 state with strong SOC. Real systems are affected by the unavoidable presence of impurities and in this section, we show that interesting features for the existence of π states in SFIS JJs can be detected in the presence of nonmagnetic impurities, modeled as scalar on-site potentials.
In what follows, we focus on the effect of disorder on the $I_c(T)$ curves exhibiting a 0-π transition and on the corresponding CPR. In particular, firstly we consider the case of a SFIS JJ in the presence of disorder, secondly we analyze the combined effect of impurities and SOC on the $I_c(T)$ of these devices. As a matter of fact, the influence of increasing V_{imp} results in different

scenarios.

In the following simulations, we use $L = 8$, $W = 32$ as for the analysis of the clean system, and $\alpha = 0.04$ (for the case with SOC), while the following four different values of the impurity potential are chosen: $V_{imp} = 0.025, 0.125, 0.150, 0.250$. Moreover, here, small on-site exchange field fluctuations are considered ($\delta_h \neq 0$) to model a more realistic scenario in which the exchange field may be non-uniform in the whole barrier.

In Fig.3.6 (a) we show the $I_c(T)$ curve at $\alpha = 0$, calculated as the impurity potential increases. We notice that for high values of V_{imp} the system changes its $I_c(T)$ behavior leaving the 0-π regime and reaching a stable π state almost over the whole temperature range, as it is evident in the corresponding CPRs (Figs.3.6 (c-e)). Precisely, for $V_{imp} = 0.025$ (green curve) both the maximum of the second lobe and the dip of the 0-π transition settle at higher values of current with respect to the clean regime (black line in Fig.3.6 (a)). Consequently, the clear effect of increasing V_{imp} is the filling of the minimum of the 0-π transition and its shifting toward very low temperatures (red and blue curves), leading to the AB-like behavior for the highest disorder configuration (orange curve), corresponding to a pure π regime (Fig.3.6 (e)). The presence of impurities seems to be a driving force for the conversion of a 0-π JJ into a pure π one. As it is shown, in the absence of SOC the realization of an almost pure π JJ is feasible even for small values of the impurity potential (Fig.3.6 (c, d)).

In the presence of SOC (Fig.3.6 (f)) the clean $I_c(T)$ curve (black line) exhibits a 0-π transition occurring at $T \sim 0.45T_c$, characterized by a lower value of the current in the π state. In this case, we can notice that enhancing the impurity strength produces a more gradual filling of the 0-π dip together with its broadening (Fig.3.6 (f), red and blue curves), shifting it toward higher critical current values and lower temperatures. When passing from the 0-π regime to the π one, with $\alpha \neq 0$, the system also shows a peculiar plateau region in the $I_c(T)$ extended over a wide range of temperatures, for intermediate values of V_{imp} (Fig.3.6 (f), red curve). The combined effect of SOC and impurities allows to stabilize the 0-π transition over a wide range of temperatures. However, for $V_{imp} = 0.250$, we observe a sharp change in the $I_c(T)$ behavior, where neither the plateau nor the 0-π dip are no longer visible, suggesting that the 0-π transition may occur at very low temperatures and that the pure π regime may be reached at larger values of V_{imp}.

We may further analyze the system response to the presence of disorder by looking at the CPRs (Figs.3.6 (b-e), (g-l)), corresponding to the $I_c(T)$ curves in Figs.3.6 (a) and (b), respectively.

For the first scenario (Figs.3.6 (a, b-e)), the increase of V_{imp} produces strong modifications in the CPRs, characterized by an enhanced contribution of higher order harmonics at low temperatures, reflecting the lowering of the 0-π transition temperature ($T_{0-\pi}$). Further, for $V_{imp} = 0.250$ the CPRs are opposite in sign with respect to the typical $\sin\phi$ behavior, indicating that a

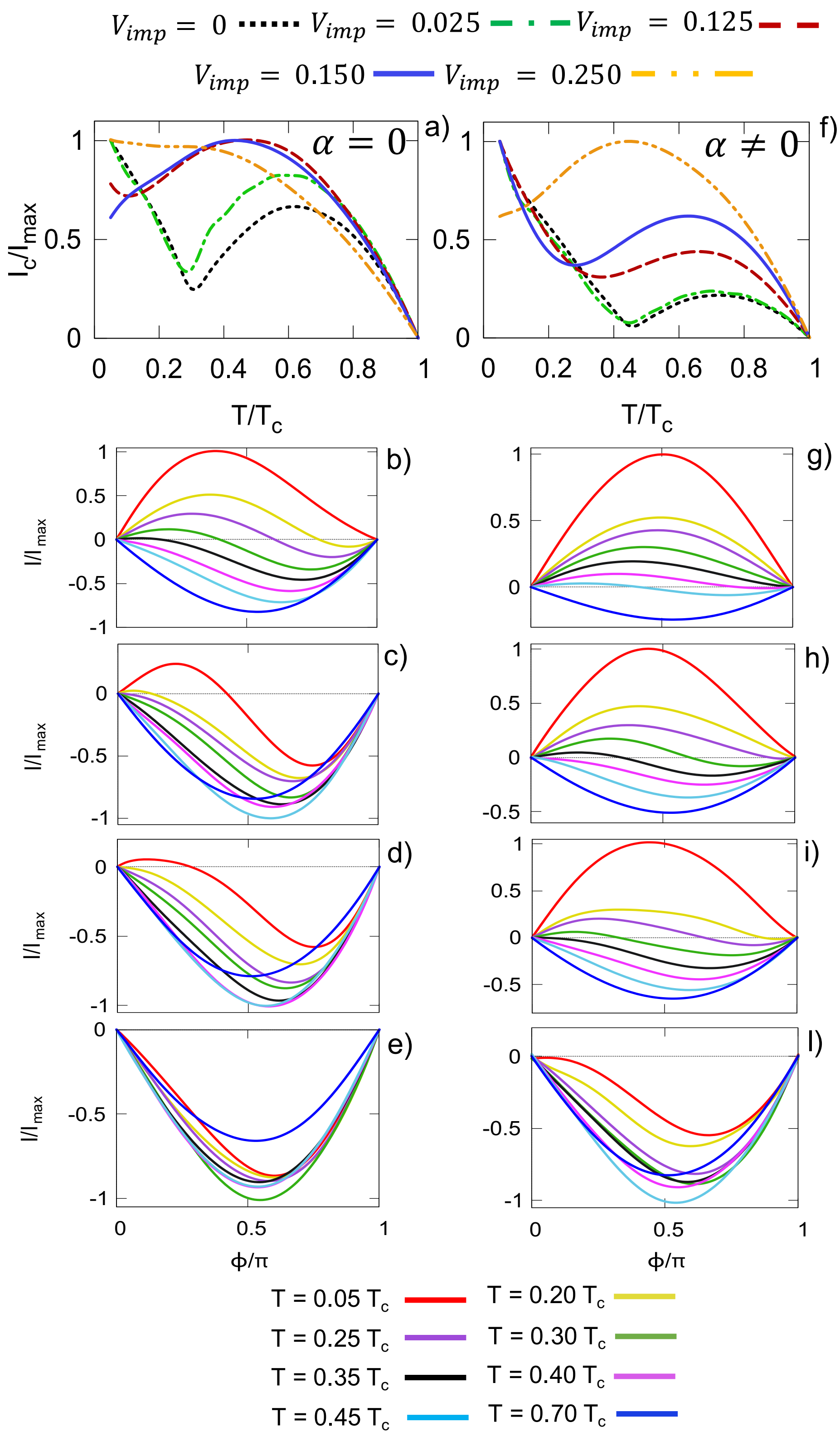

Figure 3.6: Effect of increasing V_{imp} in the cases without and with SOC (a, f). Corresponding calculated CPRs (b-e, g-l), at selected temperatures, and formation of π state (see text for details on the used parameters).

phase difference of π is established across the junction.
On the other hand, in Figs.3.6 (f, g-l) we present the CPRs in the case of $\alpha \neq 0$. Here, the 0-π transition gradually moves to lower temperatures as V_{imp} increases, until the junction is totally π for the highest value of V_{imp} (Fig.3.6 (l)). In Fig.3.6 (f) we observe that the influence of the SOC on the dirty SFIS JJs consists in stabilizing the 0-π regime even for moderately high values of the impurity potential. Here, the result of the coexistence of two competing effects, namely the spin-orbit and the disorder, is noticeable. Indeed, as for the clean regime, also in the dirty case the SOC tends to bring the system toward the 0 state; whereas the non-magnetic on-site impurities encourage it to turn toward the π state. This results in the slowdown of the switching from 0-π to π $I_c(T)$ behavior, which, thus, takes place more gradually as V_{imp} is enlarged. For this reason, the system goes through an intermediate regime involving a widened 0-π transition characterized by the plateau in the critical current, before reaching the π regime. In this situation, we can better visualize how the impurities drive the transformation of the $I_c(T)$ from that of a 0-π JJ to the one of a π JJ. Indeed, this mechanism is only slightly perceivable when $\alpha = 0$ and the entire process happens almost suddenly.
We can provide a qualitative picture of this phenomenon in the following.

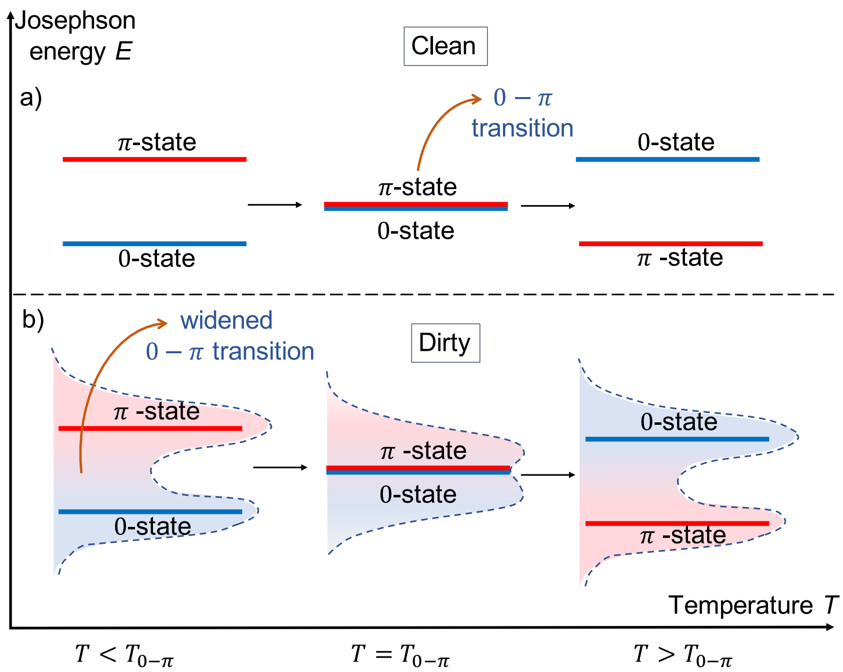

Figure 3.7: Schematic representation of 0 and π energy levels in the clean (a) and dirty (b) regime. In the latter case, the broadening in energy, due to the presence of on-site non-magnetic impurities, is shown.

In the clean case, for temperatures lower than the 0-π transition one ($T < T_{0-\pi}$) the lower energy level is the 0 state. When $T = T_{0-\pi}$ the 0 and π energy levels are coinciding; finally, for $T > T_{0-\pi}$ the 0-π transition has occurred and the Josephson energy minimum is reached at $\phi = \pi$ (Fig.3.7 (a)). On the other hand, the presence of on-site non-magnetic impurities produces a broadening in energy (and, therefore, in temperature) of the 0 and π energy levels (Fig.3.7 (b)). The broadening of the levels gives rise to an overlap region in which the JJ comes to be in a "hybrid 0-π state" over a more or less extended range of temperatures. When the impurities strength is enhanced, the overlapping between the levels grows together with the probability that, for $T < T_{0-\pi}$ (where $T_{0-\pi}$ is the transition temperature in the clean limit), the system prefers to stabilize in the π energy state.
Finally, in Fig.3.8 we illustrate the possibility to build up a controllable device that can host all the $I_c(T)$ regimes. Here, we show that, once we fix the impurity potential strength in such a way to have an almost pure π JJ in the $\alpha = 0$ configuration (Fig.3.8 (a)), by adding the spin-orbit interaction and modifying its coupling strength, we manage to drive the junction toward 0-π (Figs.3.8 (b-c)) and 0 (Fig.3.8 (d)) regimes. This happens in a reversible manner, in the sense that decreasing the SOC would bring back the system in the initial π state.

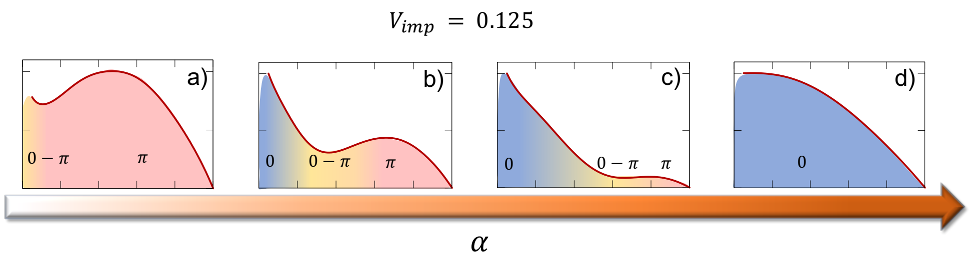

Figure 3.8: Effect of SOC strength (α) increasing on the $I_c(T)$ behavior, at fixed value of the impurity potential ($V_{imp} = 0.125$). The $I_c(T)$ curves are calculated for the following values of $\alpha = 0$, 0.04, 0.07, 0.20. The $I_c(T)$ curves in (a) and (b) correspond to the ones in Fig.3.6 (a) and (f), respectively, for $V_{imp} = 0.125$.

3.6 Analysis of pairing functions

In this paragraph, for sake of completeness, we look at the possible pairing mechanisms that can take place in the devices analyzed in the previous section. In SFIS JJs, the exchange field breaks the time-reversal symmetry, giving rise to the zero-spin triplet pairing correlations. However, when we consider systems with impurities and SOC the chance to have more exotic

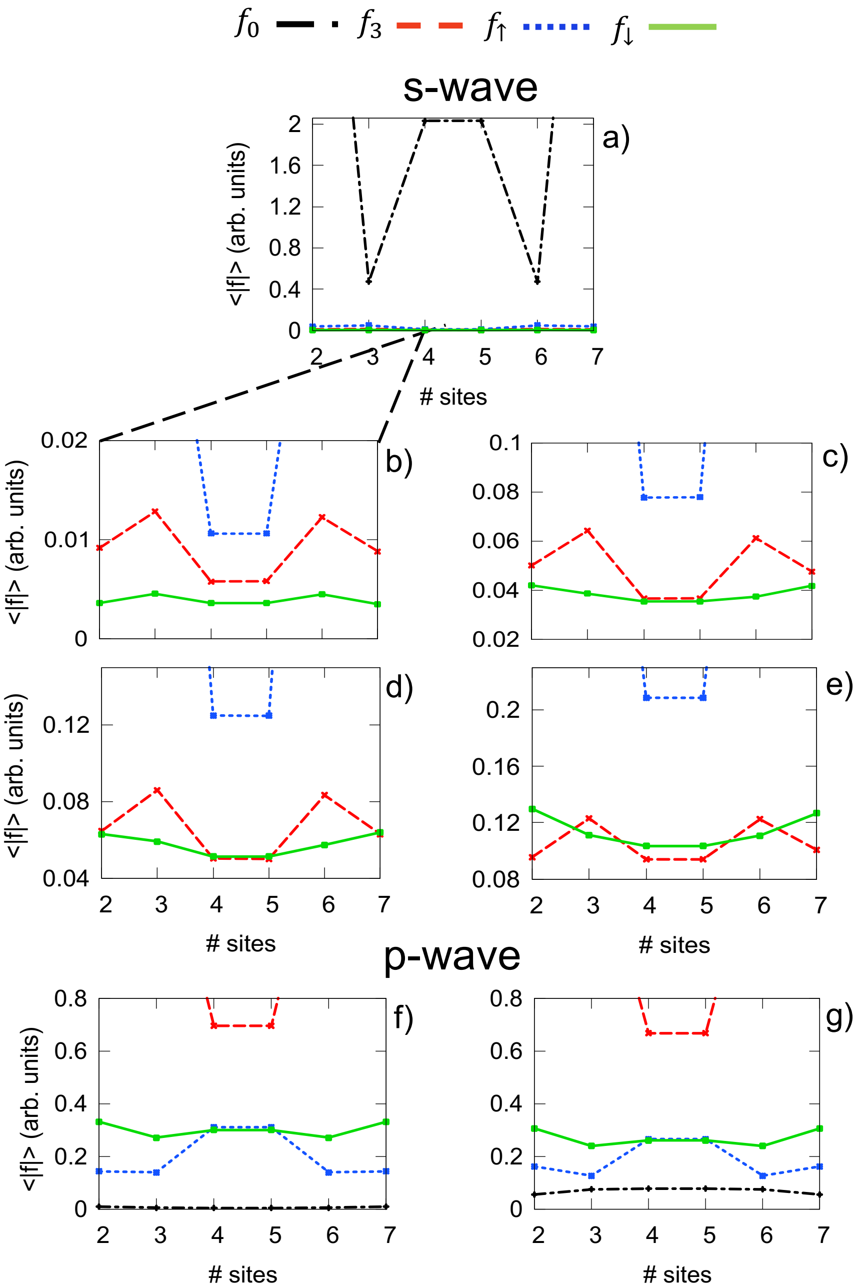

Figure 3.9: Module of spatial profile of s and p-wave pairing components, calculated at $h = 0.45$, $\alpha = 0.04$, $T = 0.025T_c$ and $\phi = 0$, for $V_{imp} = 0.025$ (a, b, f), $V_{imp} = 0.125$ (c), $V_{imp} = 0.150$ (d) and $V_{imp} = 0.250$ (e, g).

pairing components becomes relevant. In particular, as we illustrated in Chapter 1, in the presence of SOC triplet pairings with parallel spins (with

$S_z = \pm 1$ projection) emerge. Indeed, the generation of equal-spin triplet correlations via SOC is provided by the fact that, at interfaces, spin-orbit interaction breaks the spin symmetry, leading to a mixing of spin-up and spin-down channels in such a way that the total spin S is no longer a good quantum number. As a result, the proximity amplitudes in the ferromagnet will intrinsically be a mixture of singlet and triplet pair correlations.

Moreover, we notice that SOC breaks also the inversion symmetry at the S/FI interfaces, thus, all four types of pair amplitudes (i.e., s-wave singlet, s-wave triplets, p-wave singlet, p-wave triplets) can be found in the F region [41–43]. Since the Pauli's principle requires the pairing correlations to be totally antisymmetric, as we have seen in Chapter 1, the possible types of pairing functions have to fulfill specific symmetry properties with respect to spin, momentum, and frequency [41–43, 143, 179–181]. For this reason, the s-wave singlet as well as the p-wave triplets are even functions of the Matsubara frequencies ω_n (even-frequency), while the s-wave triplets and p-wave singlet are odd-frequency.

In Fig.3.9 we show the amplitude of the spatial profile of the calculated s- and p-wave correlation functions, as a function of the position inside the FI barrier (expressed in terms of the number # of sites), corresponding to the system configurations analyzed in the previous section in the presence of SOC and disorder, Figs.3.6 (f), and (g) to (l). In the following calculations we set $h = 0.45$, $\alpha = 0.04$, $T = 0.025\,T_c$ and $\phi = 0$. The other parameters are set as in the previous sections. As well as for the systems in Figs.3.6 (f), and (g) to (l), we choose the following values of the on-site impurity potential: $V_{imp} = 0.025$ (Figs.3.9 (a, b, f)), $V_{imp} = 0.125$ (Fig.3.9 (c)), $V_{imp} = 0.150$ (Fig.3.9 (d)) and $V_{imp} = 0.250$ (Figs.3.9 (e, g)). The plots in Figs. (b) to (e) represent a zoomed-in view of the s-wave spin-triplet components, while in Figs. (f) and (g) we show a zoomed-in view of the p-wave correlations for the configurations with the lowest and highest value of V_{imp}.

In the s-wave symmetry, the majority component is the spin-singlet one f_0 (for simplicity only shown in Fig.3.9 (a)); nevertheless, this is to be expected since we are considering a short-FI barrier directly coupled to conventional s-wave singlet SCs. Furthermore, f_0 is an even-frequency function and in the Matsubara summation it is reinforced. We observe that the s-wave spin-triplet pairings, initially generated by SOC at interfaces, survive throughout the FI region and intriguingly appear remarkably enhanced by the effect of increasing the impurity potential V_{imp}. In the middle of the FI barrier (site # 4) we obtain that, passing from $V_{imp} = 0.025$ to $V_{imp} = 0.250$ (Figs.3.9 (b) and (e)), the s-wave singlet f_0 (even-frequency) remains almost unchanged, while the s-wave spin-triplets (odd-frequency) f_3, $f_\uparrow$ and $f_\downarrow$ result increased by factors of ~ 15, ~ 21, ~ 33, respectively. Further, in Figs.3.9 (f) and (g), it is shown that a sizable p-wave pairing is already induced in the FI layer in the nearly clean situation ($V_{imp} = 0.025$). In this case, the majority contribution is provided by the zero-spin triplet (f_3). However, the spin-singlet f_0 (odd-frequency) results enlarged by the influence of nonmagnetic disorder, while the triplet correlations (even frequency), contrary to s-wave ones, appear rather stable with respect to the increment of lattice impurities. Finally, at site # 4 comparing the p-wave pairings with the s-wave ones corresponding to the highest value of impurities strength, we find that the equal-spin components $f_\uparrow$ and $f_\downarrow$ are almost of the same order of magnitude in both the s- and p-wave cases.

Our results highlight the importance of SFIS JJs with SOC and tuned impurities as promising platforms hosting unconventional odd-frequency superconductivity and showing sizable equal-spin triplet pairings, thus verifying the predictions in Refs. [67,68].

3.7 Conclusion

In this chapter, we focused our attention on the problem of the tunability of 0-π transitions in SFIS JJs. Using a Bogoliubov de Gennes 2D tight-binding model we managed to study the temperature-dependent transport properties of these devices. Here, we extended the analysis carried out in Ref. [90] to the case of 0-π junctions with ferromagnetic insulator barriers. In particular, we analyzed the influence of spin-mixing (due to SOC) and nonmagnetic disorder effects on SFIS JJs, focusing on the $I_c(T)$ behavior. We pointed out the role of SOC in driving the switching between 0-π and 0 regimes and the capability to induce 0-π to π conversions by adding disorder to the system. In particular, the engineering of the impurity concentration (that is strongly linked with the model parameter V_{imp}) could lead to the realization of stable π junctions, highly desired for superconducting circuits. Moreover, we figured out the opportunity to obtain a fully tunable system, starting from a π JJ and tuning the spin-orbit field by external means.

In this context, the SFIS JJs analyzed here could represent an intriguing and unexplored platform which can be switched among the three different regimes. Finally, we complete our analysis by studying the correlation functions in the presence of SOC and impurities. In particular, we observed an enhanced contribution of the odd-frequency pairings, i.e. s-wave triplets and p-wave singlet due to the increasing of nonmagnetic disorder. Therefore, we recognized these tunable SFIS JJs as good candidates to host unconventional superconducting pairing mechanisms and the source of sizable spin-triplet superconductivity, confirming the results of the authors of Refs. [68,90].

Chapter 4

Coexistence and tuning of spin-singlet and triplet transport in spin-filter Josephson junctions

The increased capabilities of coupling more and more materials through functional interfaces are paving the way to a series of exciting experiments and extremely advanced devices. Here we focus on the capability of magnetically inhomogeneous superconductor/ferromagnet (S/F) interfaces to generate spin-polarized triplet pairs. In particular, we apply the theoretical 2D tight-binding model described in the previous sections to experimental systems characterized by spin-filter ferromagnetic Josephson junctions (JJs), finding unique correspondence between neat experimental benchmarks in the temperature behavior of the critical current $I_c(T)$ and the theoretical model based on microscopic calculations. In this chapter, we focus on studying the induced pairing correlations in these devices, and their possible connection with the $I_c(T)$ behavior. As a matter of fact, this kind of combined analysis provides accurate proof of the coexistence and tunability of singlet and triplet transport in such systems. From a theoretical point of view, we consider ferromagnetic insulator JJs (SFIS JJs) in the presence of spin-mixing effects (due to SOC) and nonmagnetic disorder, where the possibility to model these interactions allows to enlarge the space of parameters that regulate the phenomenology of the Josephson effect, thus offering the opportunity to extend the application to a variety of hybrid types of JJs.
This chapter is inspired by the work presented in Ref. [68] and is organized as follows.
In the first section, we briefly recall the theoretical formalism used in this analysis and discuss the choice of the model parameters, in relation with the experimental values found in the literature, regarding these systems. Then

we apply the 2D tight-binding model and the RGF technique to calculate the $I_c(T)$ and correlation functions, where the former will be the benchmark for the comparison with the experimental data and the starting point for the discussion on the possible singlet and triplet proximity effect arising in in these structures. Subsequently, we proceed proposing an investigation on the possible analogy existing between the response of spin-filter JJs to the application of a weak external magnetic field, and the role of SOC and impurities in the model. Lastly, we complete our analysis illustrating how the $I_c(T)$ behavior can be modified by the combined effect of SOC and impurities, by expanding the range of parameters describing these effects.

4.1 Introduction

Ferromagnetic (SFS) JJs are a unique platform to integrate the coherent quantum nature of superconductors and ferromagnets into unconventional mechanisms and smart tunable functionalities. The rich literature has established several key elements, which arise when superconducting pair correlations traverse the exchange field of a ferromagnet [15, 17, 19, 30, 57]. JJs with multiple F-layer barriers have been theoretically and experimentally studied in connection to unconventional triplet superconductivity with equal-spin Cooper pairs, characterized by total spin momentum $S = 1$ and spin z-component $S_z = \pm 1$ ($|11\rangle_{S,S_z} = |\uparrow\uparrow\rangle$ and $|1-1\rangle_{S,S_z} = |\downarrow\downarrow\rangle$), which can be artificially generated in these structures [15, 19, 47, 48, 54, 85–88, 186]. Compared to spin-singlet Cooper pairs ($|00\rangle_{S,S_z} = 1/\sqrt{2}(|\uparrow\downarrow\rangle - |\downarrow\uparrow\rangle)$) and opposite-spin triplet Cooper pairs ($|10\rangle_{S,S_z} = 1/\sqrt{2}(|\uparrow\downarrow\rangle + |\downarrow\uparrow\rangle)$), the spin-aligned triplet Cooper pairs are immune to the exchange field of the F layer and can carry a non-dissipative spin current. Therefore, spin-triplet Cooper pairs constitute the essential element for the emerging field of superconducting spintronics [47, 48, 85–88].
It is well established that spin-polarized triplet pairs are generated via spin-mixing and spin-rotation processes at magnetically inhomogeneous S/F interfaces [19, 46, 47, 86, 87, 187], as we have seen in Chapter 1. Recently, theoretical and experimental studies have been dedicated to an alternative mechanism for triplet pair generation involving spin-orbit coupling (SOC) in combination with a magnetic exchange field [188, 189]. These systems may benefit from the capability to generate controllable spin-polarized supercurrents with a single ferromagnetic layer, compared to magnetically textured JJs.
A conclusive evidence for the spin-triplet nature of the supercurrent could be supported by the capability to distinguish singlet and triplet components. The capability of quantifying the amount of spin-polarized supercurrents remains a fundamental benchmark to further prove triplet correlations and a key step towards real applications.

In this scenario, superconducting tunnel junctions with ferromagnetic insulator (FI) barriers (SFIS), namely spin-filter NbN/GdN/NbN JJs, have revealed unique transport properties, such as spin-polarization phenomena [66, 83, 190], an interfacial exchange field in the superconducting layer [65, 191], macroscopic quantum tunneling [192] and an unconventional incipient 0-π transition [67]. In particular, with spin-filter JJs [66] we indicate those junctions in which the flowing current is highly spin polarized because of the different tunneling probability experienced by spin-up and spin-down electrons, due to the exchange splitting produced by the FI barrier [7, 193] which gives rise to a lower barrier height for spin-up electrons and a higher barrier height for spin-down electrons, thus, acting as efficient filter for spin-polarized carriers.

Such SFIS JJs are especially well-suited for the implementation in superconducting circuits in which a very low dissipation is required [60–62, 64, 82, 194]. Furthermore, in these systems, evidence of spin-triplet transport has been reported [57, 67, 83, 84].

Here we build on a study of the critical current I_c as a function of temperature T in NbN-GdN-NbN JJs [67], to demonstrate coexistence and tuning of singlet and triplet components. By using a 2D tight-binding Bogolioubov de Gennes (BdG) approach [89–91], we model the $I_c(T)$ curves in the whole temperature range, along with the corresponding current-phase relation (CPR) as a function of the temperature T . It turns out that measurements of the temperature behavior of the critical current along with microscopic modeling approach provide an alternative accurate method to assess the spin-triplet transport, which can be extended to different types of JJs: the amount of spin-singlet and -triplet correlations can be quantified and parameterized in terms of disorder parameter and spin-mixing (SOC) mechanisms through a fitting of experimental data.

The large variety of materials and configurations employed in diffusive SFS JJs in the literature allows to access a wide range of behaviors for the thermal dependence of the critical current [15, 71]. Particularly relevant in this context is the non-monotonic behavior for the $I_c(T)$ in systems in which a 0-π transition occurs, characterized by a peculiar cusp at the transition temperature $T_{0-\pi}$ [15, 30]. In this chapter, we focus on the peculiar behavior of the $I_c(T)$ in tunnel ferromagnetic spin-filter JJs, in which an unconventional 0-π transition occurs. Specifically, in the devices discussed here, the $I_c(T)$ curve shows a region in which the I_c is constant in a wide range of temperatures, i.e. it shows a *plateau*, or it shows a non-monotonic trend characterized by a non-zero local minimum, i.e. the $I_c(T)$ exhibits an *incipient* 0-π transition. Such unconventional $I_c(T)$ behavior turns out to be the benchmark for the coexistence of spin-singlet and spin-triplet superconductivity in SFIS junctions. As we will see, when the $I_c(T)$ curve is characterized by a plateau over a wide range of temperatures, the competition between the singlet and triplet pairing amplitudes becomes significant, in both s-wave and p-wave symmetries. This behavior sets in due to the combined effects of impurities and spin-mixing mechanisms. On the other hand, when the $I_c(T)$ curve exhibits an incipient 0-π transition, the equal-spin triplet component is gradually suppressed, becoming irrelevant in the limit case of a more standard cusp-like 0-π transition. This last situation corresponds to relative low values of disorder and spin-mixing effects.

4.2 Formalism and model parameters

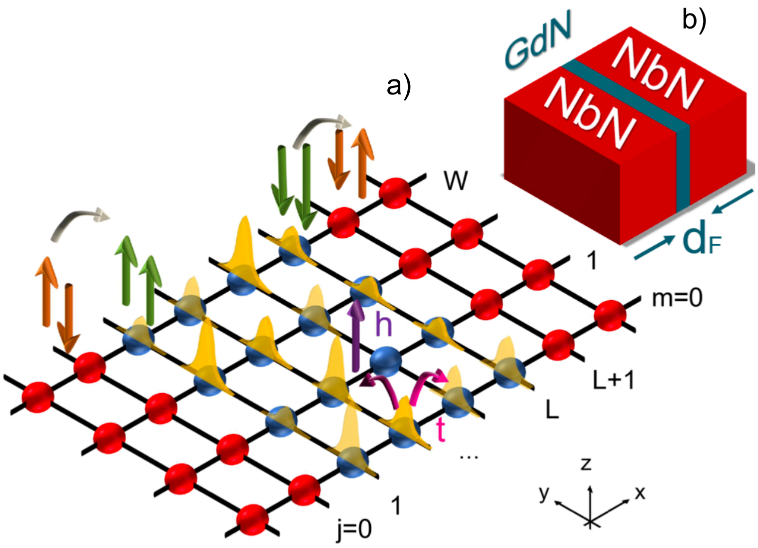

Figure 4.1: (a): Picture of the SFIS JJs 2D lattice model. The barrier (highlighted in blue) has a total thickness L along $\mathbf{x}$. The junction width is W along $\mathbf{y}$. The spin-mixing mechanism due to SOC is depicted by the spin-flipping process highlighted at the interface between the superconducting boundaries (red sites) and the barrier. The impurities, with random strength depicted by the height of the yellow potential peaks, are represented on each site of the lattice. The exchange field h (violet arrow) is parallel to the z-axis, while the hopping t between nearest-neighbor sites is here represented by pink arrows. (b): Sketch of the experimental NbN/GdN/NbN JJs analyzed.

In this paragraph we briefly discuss the spirit of our lattice modeling that we want to use for the description of the experimental systems considered, consisting of NbN/GdN/NbN JJs.
Also in this case, the Josephson current at finite temperature and the pairing correlation functions in s- and p-wave symmetry are derived from the

Matsubara GF of the FI barrier (Eqs.(2.42)-(2.44)), calculated with the recursive RGF technique [89–91], as illustrated in Chapter 2, where the SFIS junctions are modeled by using a BdG Hamiltonian on a two-dimensional (2D) lattice [68, 89–91]. A schematic representation of the 2D lattice model, in comparison with the sketch illustrating the structure of real experimental systems, is reported in Fig.4.1; as usual we indicate with L the length of the FI barrier and W the width of the junction expressed in lattice units, along the x and y directions, respectively.

The Hamiltonian of the S leads is described by the parameters t_s and μ_s, denoting the hopping integral among nearest-neighbor lattice sites and the chemical potential, respectively. Relevant parameters of the barrier Hamiltonian $\hat{H}_{FI}$, instead, are the hopping integral t, the Fermi energy μ_{FI} and the amplitude of the spin-orbit interaction α, used to introduce a spin-symmetry breaking [195, 196], through the spin-mixing mechanism. Furthermore, we include on-site random impurity potential with strength $v_{\mathbf{r}}$ uniformly distributed in the range $-V_{imp} \leq v_{\mathbf{r}} \leq V_{imp}$. Finally, the exchange field is assumed to be slightly disordered; we take it oriented along the z-axis, together with the corresponding small on-site fluctuations δ_h, given randomly in the range $-h/10 \leq \delta_h \leq h/10$. Details on Hamiltonian parameters used in the simulations can be found in Chapter 2.

However, here we explain the choice of parameters used in the theoretical model, in comparison with the real experimental values found in the literature, typical of the systems analyzed.

All the energy parameters are expressed in dimensionless units where the energy scale is the hopping t in the FI. The strength of the SOC, α, is scaled by ta (with a lattice constant), while the Josephson current is calculated in units of $I_0 = e\Delta$.

Further, the presence of disorder requires the need to perform ensemble averages over several samples to obtain the final $I_c(T)$ curves and correlations. In particular, we use $N_s = 50 - 100$ samples to compute the average $I_c(T)$ and $N_s = 200 - 300$ samples for the average correlation functions, depending on the strength of V_{imp}.

In our simulations, we fix $t = 1$, $\mu_{FI} = 0$, $\mu_s = 3$, $\Delta = 0.005$, $h = 0.25$. Further, we note that NbN (S leads) and GdN (FI barrier) are characterized by almost equal hopping parameters [197–199], which are set equal $t_s = t$ for the sake of simplicity. The choice of assuming different chemical potentials for the S and FI regions is made in order to model the experimental devices as tunnel junctions with a ferromagnetic half-metallic GdN barrier, as experimentally observed [200] and predicted by full atomistic simulations [201, 202]. The estimate for the exchange energy h is chosen in agreement to the exchange field measured in several materials and is kept fixed to that of the bulk GdN [187, 191, 198, 199, 203]. This is consistent with $t \sim 3eV$ and the experimental constant lattice of GdN is $a_{GdN} = 4.974$ Å [197–199].

In Tab.4.1 and Tab.4.2 we summarize the parameters used in simulations

and the ones characterizing real systems, respectively.
When modeling the experiments, we use α as a measure of the spin-mixing (i.e. the SOC strength) and it is chosen to be $\alpha = 0.04$, unless otherwise indicated. Although we choose a small spin-orbit field so that $\alpha \ll h$, it breaks the spin symmetry at interfaces and is sufficient to cause the generation of long-range equal triplet-correlation pairs with total spin projection $S_z = \pm 1$.
The experimental JJs under study are characterized by a transverse area of $\sim 50 \mu m^2$ and by a thickness varying from 2 nm to 4 nm [67]. In our simulations, this is taken into account by considering systems with a width larger than the length of the barrier ($W > L$). The numerical simulations are performed on lattices characterized by $L = 8$ sites along the x-direction and different values of width W of the junction, in the y direction, both expressed in units of lattice sites. Tunnel junctions experience an exponential suppression of the critical current when increasing the barrier thickness [71]. In our model, this implies dealing with systems of few lattice sites, hence, we choose $L = 8$ and keep it fixed in all the numerical simulations, in agreement with the short-junction limit. However, the main effect of increasing the experimental sample thickness (and so the magnetic area of the FI) consists in enhancing the magnetic activity of the junction [66, 67, 83, 194]. In our model, we manage to mimic this effect by changing the flux of the exchange field $\Phi(h) = LWh$ through the JJ (by the means of the width of the barrier W) and by tuning the impurity potential strength V_{imp} (thus, changing the influence of disorder effects in the system). Therefore, we use these quantities as effective control parameters when modeling the peculiar behavior of the $I_c(T)$ curve in each experimental device.

Table 4.1: Values of the parameters used in simulations.

Parameter	Value (in units of t)
hopping in FI t	1
hopping in SC $t_s = t$	1
SC gap Δ	5×10^{-3}
exchange energy h	2.5×10^{-1}
exchange field fluctuations δ_h	$-h/10 \leq \delta_h \leq h/10$
spin-orbit coupling energy α	4×10^{-2}
chemical potential of FI μ_n	0
chemical potential of SC μ_s	3

Table 4.2: Main experimental values, reported in the literature, describing the analyzed systems.

Parameter	Experimental value
junction area	$\sim 50\,\mu m^2$
barrier thickness	$2-4\,nm$
hopping GdN	$\sim 3\,eV$
hopping NbN	$\sim 3\,eV$
exchange energy h	$0.5\,eV - 1\,eV$
constant lattice of GdN	$a_{GdN} = 4.974\,\text{Å}$

4.3 2D tight-binding model applied to spin-filter JJs

In this section we present our results where, in particular, the simulated $I_c(T)$ will be the benchmark for the comparison with the experimental data. We focus our analysis on the NbN/GdN/NbN JJs with FI thicknesses of: $d_F = 3.0$ nm, 3.5 nm and 4.0 nm. A sketch of the experimental samples is reported in Fig.4.1 (b).
In the theoretical model, the combined effect of SOC and impurities in the FI region efficiently mimics the presence of magnetic inhomogeneities in the barrier, which are more likely to occur in devices with large areas [47, 57], as the junctions under study. This approach is meant to include all possible effects occurring in the FI barrier, and it is a powerful platform to describe a large variety of JJs.
In Figs.4.2 (a) to (c) we show the comparison between the experimental thermal dependence of the critical current $I_c(T)$ for the junctions with GdN barriers $d_F = 3.0$ nm, 3.5 nm and 4.0 nm (black points), respectively, and the simulations obtained with the tight-binding BdG lattice model (red lines). In the insets, the measured saturation of the $I_c(T)$ down to 20 mK is also reported. The error bars on the measured I_c are of the order of 1% and represent the statistical error due to thermally-induced critical current fluctuations [192]. The amplitude of the simulated critical current has been multiplied by the experimental I_c measured at 20 mK.
As we can see, the experimental data evolve from a plateau over a wide range of temperatures (a few Kelvins) observed for the junctions with GdN thickness $d_F = 3.0$ nm and $d_F = 3.5$ nm into a non-monotonic $I_c(T)$ curve for the junction with $d_F = 4.0$ nm. The agreement between numerical outcomes and experimental data is certified by the capability to reproduce the unconventional plateau (Figs.4.2 (a) and (b)) and the non-monotonic behavior (Fig.4.2 (c)). For the $I_c(T)$ simulations in Fig.4.2 we chose: (a) $L = 8$,

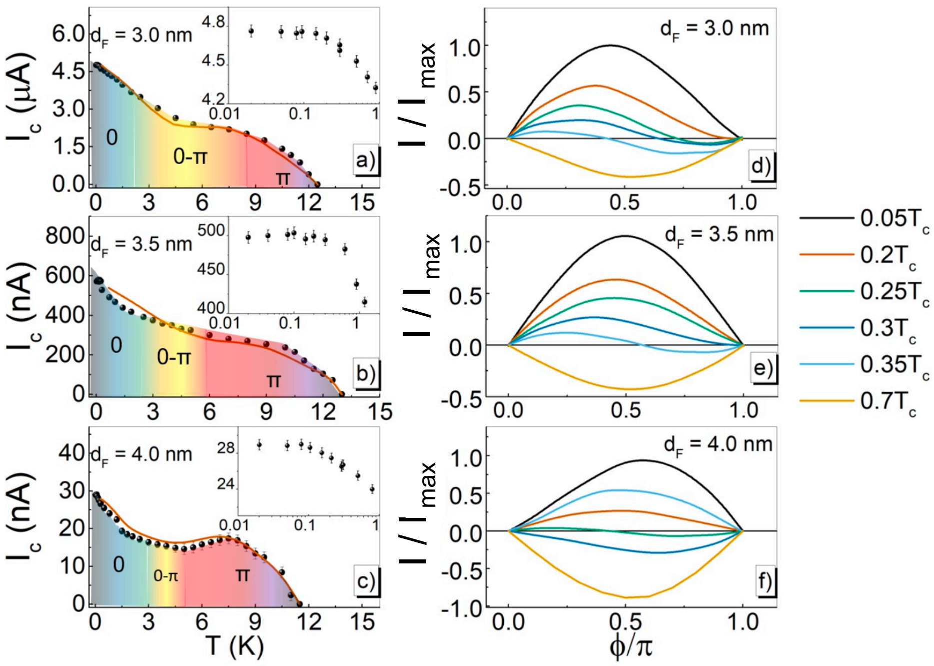

Figure 4.2: Comparison between the experimental $I_c(T)$ for spin-filter junctions with GdN barriers $d_F = 3.0$ nm (a), 3.5 nm (b) and 4.0 nm (c) (black points), and the simulations obtained with the tight-binding BdG lattice model (red straight lines). In the insets of figures (a-c): measured saturation of the $I_c(T)$ down to $20mK$. In (d-f) the corresponding calculated CPRs, at selected temperatures, are shown. The CPRs have been normalized to the maximum value of the current at $0.05T_c$. The red lines in (a), (b) and (c) are the best $I_c(T)$ curves obtained from the maximum of the CPRs calculated with the 2D lattice model, with simulations parameters as reported in the text. The color-gradient in (a), (b) and (c) depicts the temperature range for the 0 state (light blue), the π state (light red), and the width of the 0-π transition region (yellow region), obtained from the CPRs in (d), (e) and (f).

$W = 24$, (b) $L = 8$, $W = 28$, (c) $L = 8$, $W = 32$ (expressed in units of lattice sites); moreover, we set $V_{imp} = 0.150$ for the simulated curve in (a), $V_{imp} = 0.185$ in (b), and $V_{imp} = 0.115$ in (c). Here, the presence of random on-site impurities requires the need to perform ensemble averages over several samples.
We notice that the Hamiltonian parameters, as well as the lattice size, have no atomistic origin and are chosen to describe the main mechanisms that are expected to occur in the experimental devices. Even though the lattice size is scaled down compared to the experimental system, we think that our

theoretical model gives qualitatively an accordance with the experimental results as long as the model parameters are adjusted accordingly.
The main feature we can appreciate is that it is possible to relate the plateau in the $I_c(T)$ curve to an overall broadening of a 0-π transition in temperature. To make this aspect clearer, we also calculate the corresponding CPRs, as illustrated in Figs.4.2 (d) to (f), where they have been normalized to the maximum value of the current ($I_{max} = max_T[I_c(T)]$) at $T = 0.05\,T_c$. The CPRs indicate that, at low temperatures, the JJs are in the 0 state (light blue gradient region in Figs.4.2 (a), (b) and (c)), while at temperatures above $T = 0.7\,T_c$ the JJs are in the π state (red gradient region). Compared to what has been theoretically and experimentally observed in 0-π SFS and SFIS JJs [30, 60, 61, 64], when the plateau is measured in the JJs with $d_F = 3.0$ nm and 3.5 nm in Figs.4.2 (a) and (b), the CPRs exhibit the presence of higher order harmonics in the Josephson current for a wide range of temperatures (yellow gradient region). The transition region is reduced when the $I_c(T)$ curve gradually points towards a non-monotonic behavior, as shown in Fig.4.2 (c). In all the cases reported in Fig.4.2, the 0-π transition extends over a few Kelvins in temperature around 4.2 K, in agreement with previous findings [83].

4.4 Analysis of pairing functions: the $I_c(T)$ as the hallmark of singlet and triplet pairings weight

Let us now discuss the superconducting pairing correlations arising in the systems analyzed in the previous paragraph.
In Fig.4.3, we show the amplitude of the correlation functions $< |f| >$ determined from numerical simulations for the three devices at $T = 0.025\,T_c$ (corresponding to 0.3 K) and $\phi = 0$, where ϕ is the phase-difference across the device. The correlation functions are determined for the spin-singlet (f_0), spin-triplet with opposite spins (f_3) and equal-spin triplet functions ($f_\uparrow$ and $f_\downarrow$), both in s-wave (Figs.4.3 (a), (b) and (c)) and p-wave symmetries (Figs.4.3 (d), (e) and (f)), as a function of the position in the lattice along the x-direction, with index $j = 1, \cdots, L$. In order to assure the total antisymmetry of the fermionic wave function, triplet superconductivity for even-frequency pairing is conventionally of p-wave type [41, 47, 143].
As shown in the following, for symmetry reasons here the dominant orbital part in the triplet pairing channel happens to be of s-wave type. We use $<>$ to indicate the ensemble average, due to the presence of random onsite impurities in the 2D lattice. All the cases show a dominant s-wave singlet component f_0 at the superconductor/barrier interface that strongly decays toward the middle of the barrier thickness. This is reasonable be-

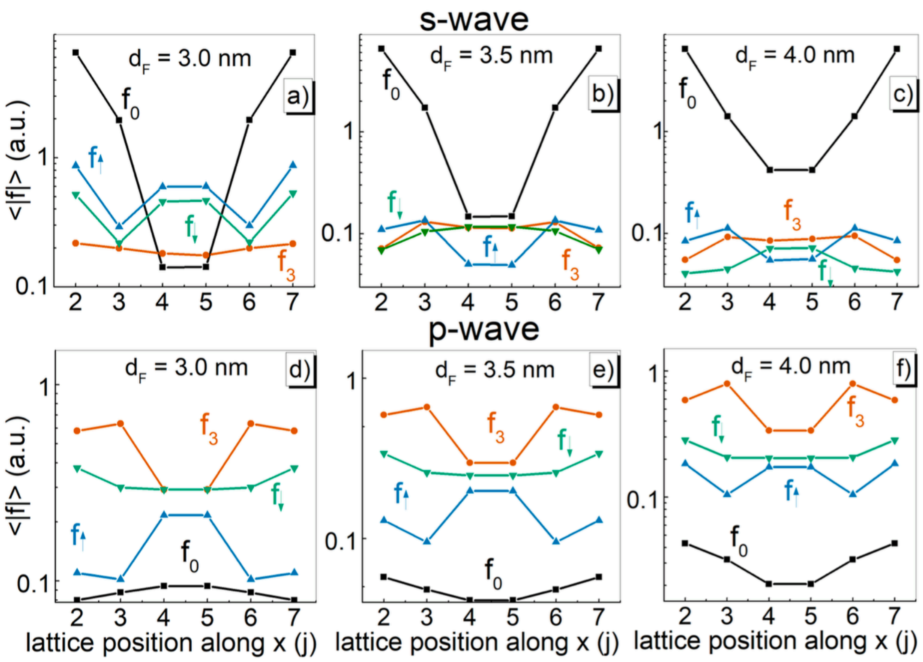

Figure 4.3: In (a), (b) and (c), the amplitudes of the ensemble average of the s-wave correlation functions $< |f| >$, determined by numerical simulations at temperature $T = 0.025\,T_c$, are shown as a function of the lattice position in the barrier along the x direction (with index j) for the junctions with GdN thickness $d_F = 3.0$ nm, 3.5 nm and 4.0 nm, respectively. f_0 is the spin-singlet (black line and square symbols), f_3 is the opposite-spin triplet (red line and circles) and $f_\uparrow$ ($f_\downarrow$) is the equal-spin triplet with up (down) S_z projection (blue line and up-triangle symbols, and green line and down-triangle symbols, respectively). In (d), (e) and (f), we show the same correlation functions components for the p-wave symmetry. Both s- and p-wave data are reported on a log-scale.

cause the sides of the FI-layer are attached to the superconducting leads with a usual Bardeen-Cooper-Schrieffer (BCS) s-wave symmetry [182] and, due to the proximity effect, the singlet pair wave function enters the barrier. In the middle of the barrier (lattice position $j = 4$), where the spin mixing and the exchange field effects take place, a competition between the s-wave triplet and singlet pair amplitudes arises. On the contrary, for the p-wave case, the singlet component f_0 turns out to be much lower than the corresponding s-wave one. At the same time, we may observe a prevalence of the zero-spin p-wave triplet component f_3 at the superconductor/barrier interface, while in the middle of the barrier thickness the spin-aligned triplet correlations become relevant. These results are justified by symmetry considerations [19,47,87,143]. Indeed, for the s-wave symmetry, the singlet is an

Table 4.3: S- and p-wave symmetry spin-correlations. Ensemble average of the pair-correlation amplitudes $\langle |f| \rangle$ in both s- and p-wave symmetry for JJs with GdN thickness d_F in units of the major zero-spin component: the spin-singlet f_0 for the s-wave correlations (A) and the zero-spin triplet f_3 for the p-wave correlations (B).

(A)	s-wave			(B)	p-wave		
d_F (nm)	$f_\uparrow/f_0$	$f_\downarrow/f_0$	f_3/f_0		$f_\uparrow/f_3$	$f_\downarrow/f_3$	f_0/f_3
3.0	4.21	3.23	1.28		0.74	1.00	0.32
3.5	0.34	0.80	0.78		0.67	0.84	0.14
4.0	0.11	0.15	0.20		0.51	0.60	0.06

even-frequency function, while the triplets are odd-frequency. The viceversa is valid for the p-wave case.
The $d_F = 3.0$ nm-thick barrier junction exhibits s-wave triplet correlations functions larger than the singlet one, with a major contribution provided by the equal-spin triplet component with $S_z = +1$, $f_\uparrow$ (Fig.4.3 (a)).
For what concerns the p-wave spin-correlation functions for this device, f_3 provides the main contribution at the borders, while $f_\downarrow$ competes with f_3 in the middle of the barrier (lattice position $j = 4$), as shown in Fig.4.3 (d). Moreover, the opposite and equal-spin p-wave triplet components are nearly a factor 2 larger than the corresponding s-wave singlet component.
By increasing the thickness of the barrier, thus gradually pointing towards an incipient 0-π transition with a non-monotonic behavior in the $I_c(T)$ curve, in the s-wave cases we can observe a progressive suppression of the equal-spin triplet components and a dominant spin-singlet channel. At the same time, in the p-wave case, we observe a slight reduction of the ratio between the equal-spin triplets ($f_\uparrow$ and $f_\downarrow$) and the major zero-spin component (f_3). Thus, the p-wave opposite spin-triplet components are of the same order of magnitude compared to the corresponding s-wave spin-singlet component, while the equal-spin triplet components are instead reduced.
In Tab.4.3, we summarize the values of the pair-correlations in the middle of the barrier thickness (lattice position $j = 4$), in units of the majority zero-spin component, i. e. f_0 for the s-wave (Tab.4.3 A) and f_3 for the p-wave cases (Tab.4.3 B), respectively.

The analysis of the superconducting pairings induced in these systems shows that a connection between the amplitude of the different correlation functions, especially those with s-wave symmetry, and the $I_c(T)$ behavior can be observed. In particular, we found that the characteristic plateau structure can be noticed only when considering a combined effect of SOC and impurities, once fixed the dimensions of the system. As it is shown for the SFIS JJ with $d_F = 3.0$ nm in Fig.4.2 (a) and Fig.4.3 (a), the formation of the plateau goes along with the coexistence of comparable spin-singlet and

triplet superconductivity.
Thus, in this perspective, fitting of experimental $I_c(T)$ curves allows to identify the coexistence of spin-singlet and triplet transport and quantify the weight between the different transport channels.

4.5 Analogy between the effect of an external magnetic field applied to the experimental samples, and the compresence of SOC and impurities in the model

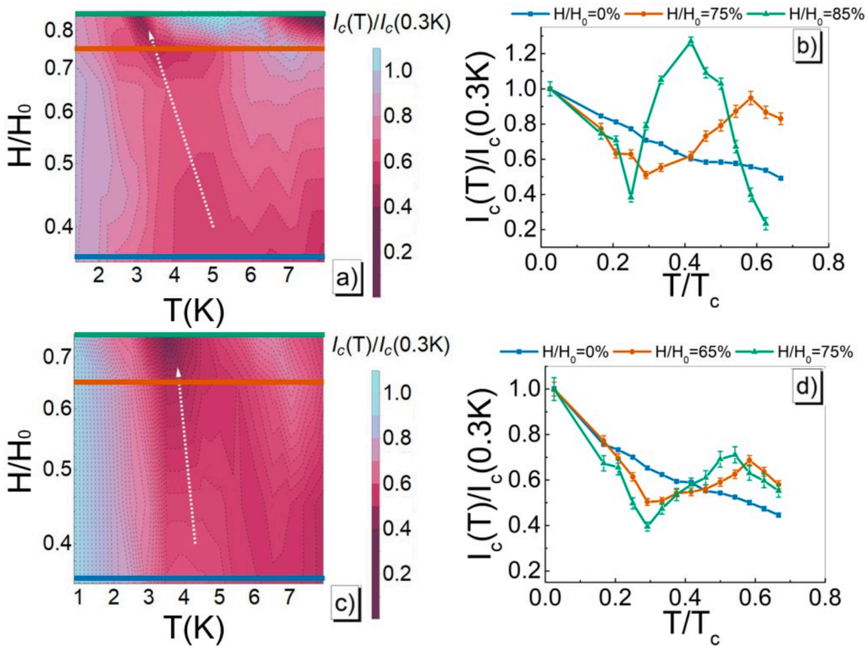

Figure 4.4: Tuning of the thermal behavior of the critical current in the presence of an external magnetic field. Normalized critical current $I_c(T, H/H_0)/I_c(0.3\,K, H/H_0)$ density plots as a function of the percentage of magnetic field periodicity H/H_0 and the temperature T , for the JJs with GdN thickness (a) $d_F = 3.0$ and (c) $d_F = 3.5$ nm. Blue, red and green lines refer to the cross sections reported in (b) and (d). The white dashed arrows in (a) and (c) are a guide for the eye and highlight the shift of the minimum in the $I_c(T, H/H_0)/I_c(0.3\,K, H/H_0)$ by increasing H/H_0.

In order to investigate the peculiar transport properties characterizing these systems, in this paragraph we propose a study on possible analogy be-

tween the effect of an external magnetic field applied to the experimental NbN/GdN/NbN junctions and the combined presence of SOC and nonmagnetic lattice impurities in the theoretical model.
From the experimental side, the $I_c(T)$ response to an external magnetic field applied to the samples in the plane of the JJs (specifically along the z direction) has been probed. In Fig.4.4 the evolution of the normalized critical current $I_c(T, H/H_0)/I_c(0.3\,K, H/H_0)$ as a function of a weak magnetic field H/H_0 is shown, where H_0 is the amplitude of the first lobe of the Fraunhofer pattern curve, acquired by applying the magnetic field from $+2.4$ mT to -2.4 mT. H_0 is estimated at each investigated temperature T (from $T = 0.3$ K to $T = 8$ K). The results are reported in Fig.4.4 in the two density-plots (a) and (c) for the junctions with $d_F = 3.0$ nm and 3.5 nm, respectively.
We can notice that, increasing the field H/H_0, the plateau structure at zero field previously illustrated in Figs.4.2 (a) and (b) evolves into a non-monotonic behavior with a minimum (dark region around 70-80% H_0 and between 2 and 4 K) and a maximum (bright region around 70-80% H_0 and between 4 and 6 K). The effect appears more pronounced for the JJ with $d_F = 3.0$ nm (a). The blue, green and red dashed line cuts are related to the cross-section curves reported in Figs.4.4 (b) and (d), where the gradual appearance of an enhanced dip and a non-monotonic behavior in the normalized $I_c(T)$ curves can be observed by increasing H/H_0. The error bar on each measured point is of the order of few percents and it is due to thermally-induced I_c fluctuations [192].
Even if the strength of the external magnetic field is not enough to generate a complete magnetic ordering, slight modifications in the microscopic structure of the barrier arise [204], which has been already predicted to occur in systems with tunable domain walls [205], intrinsic SOC [206] and magnetic impurities [176]. At zero field, the magnetic disorder is maximum and likely introduces electronic defect states in the barrier [207]. As the field increases, the system undergoes towards a more ordered phase, and hence defect states density reduces. Therefore, the tunability of the $I_c(T)$ shape from the plateau towards a non-monotonic curve by applying an external magnetic field can be related to a reduction of the disorder in the barrier.

This picture exhibits an analogy with numerical simulations obtained when changing the strength of the impurity potential in the 2D lattice model while keeping fixed all the other parameters. In particular, it is worth to notice that, in the model, we do not include the Peierls phase in the hopping parameters due to the external magnetic field, nor we study the dynamics of the magnetization in barrier. It would include extra complications that are not justified in this analysis. The main point here is that our samples have a ferromagnetic tunnel (FI) barrier. Qualitatively, the main role of the external field in these samples is to trigger the magnetic ordering in the GdN layer. Within our model, this effect is qualitatively accounted

by reducing the impurity scattering in FI layer in the presence of SOC. Local impurity potentials in the FI barrier are assumed to induce small site-dependent fluctuations of the chemical potential. In our approach, the coexistence of spin-mixing mechanisms, promoted by SOC-like interactions, and on-site impurities, model the magnetic disorder.
We show the result of the interplay of these effects in Fig.4.5 (a), illustrating the simulated $I_c(T)$ for different V_{imp} values. Here, the current is normalized to the maximum of the CPR at the lowest investigated temperature T, while T is normalized to the critical temperature T_c.
We can notice that the characteristic 0-π behavior is modified by increasing the impurity potential V_{imp}. The enhancement of the impurity strength produces a shift of the minimum of the curve towards lower temperatures and higher critical current values, with a consequent broadening of the typical 0-π cusp that progressively gives rise to the plateau. Viceversa, decreasing V_{imp}, one can recover the 0-π transition.
In Figs.4.5 (b)-(g) we finally report the s- and p-wave correlation functions corresponding to simulated $I_c(T)$ curves for different impurity potentials V_{imp} in (a): $V_{imp} = 0.150$, $V_{imp} = 0.115$ and $V_{imp} = 0.025$. We here take as a reference the JJ with $d_F = 4.0$ nm, i.e. the simulations for lattice dimensions $L = 8$, $W = 32$. While the p-wave components appear to be approximately unaffected by disorder (Figs. 4.5 (e)-(g)), for the s-wave symmetry the effect of increasing the impurity strength V_{imp} results in a pronounced enhancement of the equal-spin triplet pairing correlations, $f_\uparrow$ and $f_\downarrow$ (Figs.4.5 (b)-(d)).

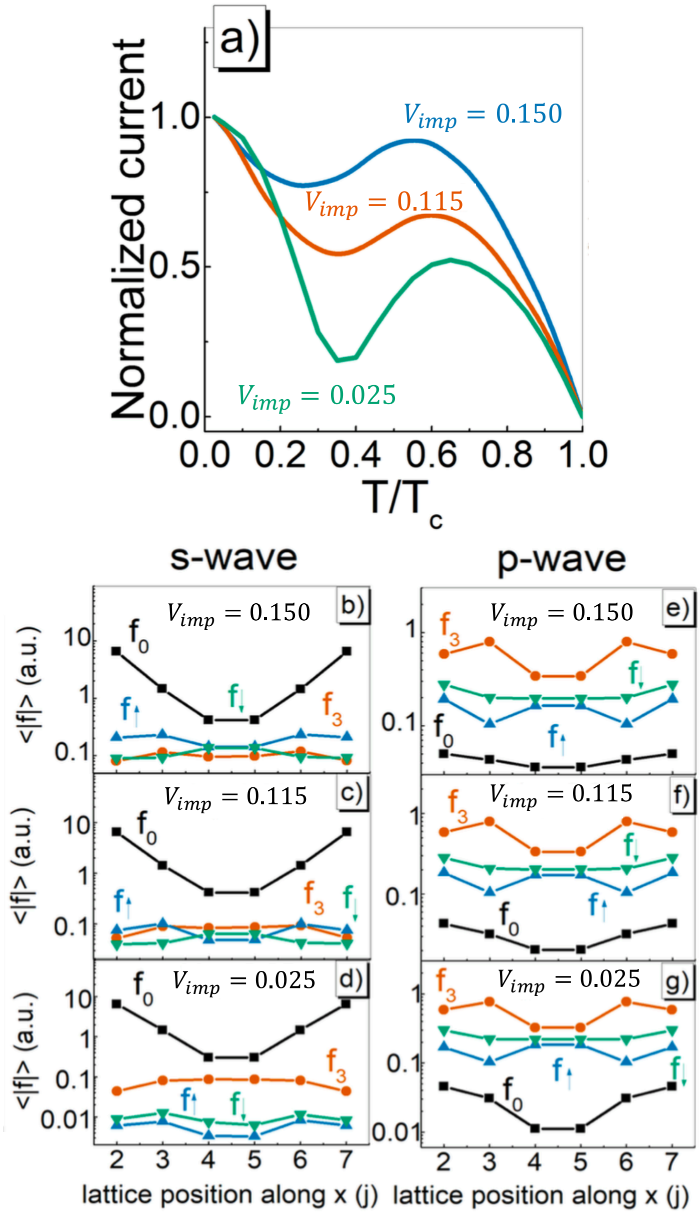

Figure 4.5: (a): Simulated $I_c(T)$ for three different impurity potential V_{imp} values: $V_{imp} = 0.025$ (green curve), $V_{imp} = 0.115$ (red curve) and $V_{imp} = 0.150$ (blue curve). The current is normalized to the maximum of the current-phase relation at the lowest investigated temperature T, while T is normalized to the critical temperature T_c. Calculated s-wave ((b), (c) and (d)) and p-wave ((e), (f) and (g)) ensemble average of the pair amplitude $< |f| >$ in arbitrary units for different impurity potential values V_{imp} in (a). f_0 is the spin-singlet component (black line and square symbols), f_3 is the opposite-spin triplet component (red line and circle symbols), $f_\uparrow (f_\downarrow)$ is the up (down) equal-spin triplet component (blue lines and up-triangle symbols, and green lines and down-triangle symbols, respectively). Both s- and p-wave data are reported on a log-scale.

Expanding the range of parameters describing the SOC and impurities strength

To get a deeper understanding of the combined effect of impurities and the SOC in these systems, here we show how they affect the $I_c(T)$ shape, expanding the range of values of these parameters in our simulations. The results are presented in Fig.4.6. Lattice dimensions are $L = 8$, $W = 32$, i.e. they refer to the JJ with $d_F = 4.0$ nm. To accomplish the $I_c(T)$ diagram, we select the following values for α and V_{imp}: from panels (a) to (d), (e) to (h), (i) to (l) and (m) to (p), $V_{imp} = 0.025, 0.115, 0.150, 0.250$, respectively, and from panels (a) to (m), (b) to (n), (c) to (o) and (d) to (p), $\alpha = 0.2, 0.1, 0.07, 0.04$. In all the panels, the I_c (y-axis) is normalized to its value at the lowest temperature, i. e. $T = 300$ mK, while the T (x-axis) is normalized to the critical temperature T_c of the device. The scale on the y-axis on each plot ranges from 0 to 1.1, as on the x-axis. Minor ticks represent an increment of 0.1.

In Fig.4.6 we can notice that for small values of α and V_{imp} (bright red- and blue-scales), the simulated $I_c(T)$ curve shows a cusp-like 0-π transition, provided that the exchange field h in the junction is non-zero, as it occurs in SFS JJs tipically reported in the literature [30,60,61,64]. By increasing α (dark red-scale), the main effect is to reduce the height of the second maximum in the $I_c(T)$ curve, without recovering the plateau structure observed in SFIS JJs. At very large α (see panel (a) in Fig.4.6), the 0-π transition is washed out and an AB-like shape sets in, stabilizing a 0 phase. In this case the main contribution is expected from the spin-singlet, though the spin-triplet correlations are increased compared to the cases with smaller α. At the same time, by keeping the spin-orbit field weak and by increasing V_{imp} (dark blue-scale), the minimum of the 0-π transition occurs at higher critical current values and it is broadened in temperature, but always showing a non-monotonic trend for the $I_c(T)$. In the limit of large V_{imp} (see panel (p) in Fig.4.6), the 0-π transition is shifted towards very low T values, stabilizing a π phase almost over the whole temperature range. This evidence is given by the sharp decrease of I_c when the temperature drops. In this regime, in agreement with Fig.4.5, we predict an enhanced contribution of the s-wave spin-triplet components due to the interplay of SOC and disorder. In the limit of large V_{imp} and α (see panel (d) in Fig.4.6), an AB-like behavior is recovered. This latter corresponds to a stable 0 phase, reflecting the fact that, in the competition between SOC and impurity scattering, the equilibrium state is dominated by α. This also confirms the presence of a threshold value of α (at fixed value of h), above which the JJ is always in the 0 phase [90,148].

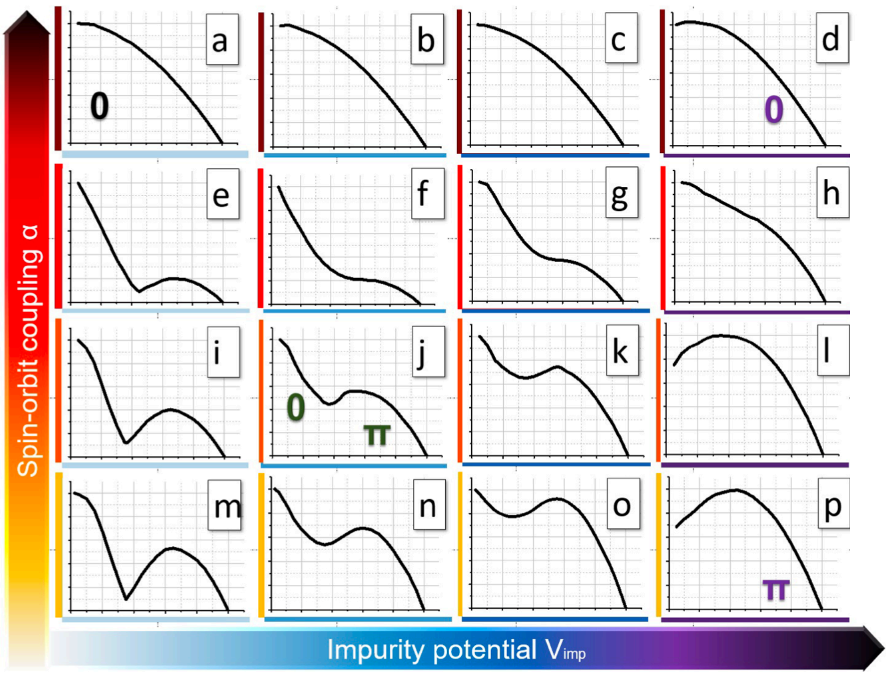

Figure 4.6: Competition between the SOC and the impurity potential and their effect on the temperature behavior of the critical current. Normalized I_c vs. temperature T curves as a function of the SOC strength α and the on-site impurity potential V_{imp}. Red-color scale refers to increasing values of α, while blue-color scale refers to increasing V_{imp} values. In (a) $\alpha = 0.2$, $V_{imp} = 0.025$; (b) $\alpha = 0.2$, $V_{imp} = 0.115$; (c) $\alpha = 0.2$, $V_{imp} = 0.150$; (d) $\alpha = 0.2$, $V_{imp} = 0.250$; (e) $\alpha = 0.1$, $V_{imp} = 0.025$; (f) $\alpha = 0.1$, $V_{imp} = 0.115$; (g) $\alpha = 0.1$, $V_{imp} = 0.150$; (h) $\alpha = 0.1$, $V_{imp} = 0.250$; (i) $\alpha = 0.07$, $V_{imp} = 0.025$; (j) $\alpha = 0.07$, $V_{imp} = 0.115$; (k) $\alpha = 0.07$, $V_{imp} = 0.150$; (l) $\alpha = 0.07$, $V_{imp} = 0.250$; (m) $\alpha = 0.04$, $V_{imp} = 0.025$; (n) $\alpha = 0.04$, $V_{imp} = 0.115$; (o) $\alpha = 0.04$, $V_{imp} = 0.150$; and (p) $\alpha = 0.04$, $V_{imp} = 0.250$. In all the panels, the I_c (y-axis) is normalized to its value at the lowest temperature, i.e. $T = 300mK$, while the T (x-axis) is normalized to the critical temperature of the device T_c. We also highlight in panels (a), (d), (j) and (p) the state of the Josephson junction: 0, 0-π or π.

4.6 Conclusion

In this chapter we have investigated on the occurrence of the unconventional thermal dependence of the critical current $I_c(T)$ observed in spin-filter JJs, in order to achieve a deeper comprehension of singlet and triplet transport phenomena that can take place in these devices.
In particular, the theoretical results show that the characteristic behavior of the $I_c(T)$ is related to the amplitude of the different spin-correlation functions, especially those with s-wave symmetry. We found that the presence of a plateau extended over a wide range of temperatures and the peculiar non-monotonic behavior in the $I_c(T)$ when increasing the thickness of the barrier can be explained in terms of the coexistence of spin-singlet and triplet superconductivity, whose correlation functions have been calculated by using a 2D tight-binding BdG description of the system [89–91].
Specifically, we observe a general decrease in the relative weight of the s-wave equal-spin triplet components ($f_\uparrow$ and $f_\downarrow$) in the junctions that show an increasing non-monotonicity of the $I_c(T)$ curves. Hence, the more $I_c(T)$ exhibits a behavior approaching the 0-π regime, the lower is the weight of the s-wave equal-spin correlations. This is in agreement with the fact that spin-aligned supercurrents are insensitive to exchange field and, thus, cannot give rise to 0-π transitions.
In addition, this approach highlighted also the role played by the disorder in the barrier. At the same time, the presence of a spin-mixing effect, in this context provided by the spin-orbit interaction, is crucial to reproduce the characteristic plateau in the $I_c(T)$ curves.
As further analysis, we proposed a study on the analogy observed between the response of the experimental samples to the application of an external weak magnetic field, and the role of SOC and impurities in the theoretical model. We have shown that a transition between the peculiar plateau-shape of the $I_c(T)$ curve towards an incipient 0-π curve is experimentally observed when increasing the strength of the external magnetic field. In this analysis, qualitatively we assume that the main role of the external field in these samples is to trigger the magnetic order in the GdN layer. Although in our model we do not include the Peierls phase in the hopping parameters, nor we study the dynamics of the magnetization in barrier, we qualitatively mimic the role of the external magnetic field by reducing the impurity scattering in the FI barrier in the presence of SOC.
In our investigation, by exploring a wider range of α and V_{imp} parameters, we found that the position in temperature of the $I_c(T)$ dip turns out to be an important benchmark relating the 0-π transition induced by the applied magnetic field, to the combined effect of impurities, exchange field fluctuations and spin-orbit coupling in the simulations. We found that for weak on-site impurity potential V_{imp}, by increasing α, the minimum of the $I_c(T)$ curve occurs at the same temperature. Instead, when increasing V_{imp}, the

minimum is shifted in temperature, as it occurs in the experimental $I_c(T)$ curves at a finite external magnetic field.
In conclusion, this jointed experimental/theoretical analysis provides a good description of the coexistence and tunability of singlet and triplet transport, where the ability to describe the combined effect of magnetic inhomogeneities and disorder in complex barriers, with clear benchmarks on the phenomenology of the junctions, can be of reference for a variety of structures.

Chapter 5

General conclusion

This dissertation has been devoted to the analysis of transport properties and novel aspects of proximity effect in Josephson junctions made of ferromagnetic insulator barrier in the presence of spin-orbit interaction, exchange field fluctuations and nonmagnetic disorder. We consider tunneling through a spin filtering ferromagnetic barrier in the insulating regime [62, 63, 66–69, 148], while most of experiments and theoretical studies carried out so far have been limited to systems containing metallic ferromagnets [15,17,19,47,56,57]. From an applied perspective, the advantage of using such SFIS junctions in superconducting circuits resides in the intrinsically non-dissipative nature of the tunnelling process in these systems, which can led to overcome issues of dissipation-driven decoherence [60–65].
The numerical studies carried out in this work were performed by using a two-dimensional (2D) Bogolioubov de Gennes (BdG) tight-binding model [68, 89–91], where the induced superconducting correlations and the Josephson current are extracted from the Green's function of the barrier, which was constructed by using the recursive Green's function procedure [89–91, 94]. This approach is particularly suitable to obtain information about transport properties of the system under consideration on the atomic scale, thus providing a site-by-site description of the order parameter inside the barrier and near the interfaces.
Due to spin-triplet character of the Cooper pairs formed in such heterostructures, the physical mechanisms at interfaces offer a rich scenario of phenomena, including the observation of transitions between the 0 and π phase [15, 17, 19, 28, 69, 82] and the formation of long-range triplet superconductivity [15, 19, 47, 48, 54, 85–88, 186].
The first part of the work collocates in the wide scenario of possibilities offered by the promising application of the π junctions, as key ingredients that open up new horizons in superconducting electronics [39, 40, 64, 76–81].
A description as close as possible to the nature of the real samples allows analyzing new ways to control the realization of π junctions and the switching

between the 0 and π state. In particular, in this work we have theoretically shown how the interplay between spin-orbit coupling and nonmagnetic disorder may be exploited for the engineering of fully tunable 0-π SFIS JJs which can be switched between the 0, 0-π , and π regimes. By analyzing the critical current behavior as a function of temperature and the corresponding current-phase relation, we pointed out the role of SOC in driving the switching between 0-π and 0 regimes and the capability to induce 0-π to π conversions by adding disorder to the system, illustrating the possibility to build up a fully controllable device [148]. This features are highly desirable in many applications and may provide physical and technical bases for realizing novel superconducting quantum circuits, as memory elements [72–75] and superconducting qubits [39, 40, 64, 76–81].
In the second part of this work, we focused on the pairing mechanisms arising in such SFIS junctions and used the microscopic theoretical model to study real NbN/GdN/NbN samples [68]. On the latter, measurements of the critical current as a function of temperature were performed. The measured $I_c(T)$ showed a peculiar behavior, characterized by uncommon plateaus or local minima in the curves, which led us to ask whether these characteristic trends could be a possible manifestation of the triplet nature of transport phenomena. The joint theoretical analysis has provided a better and more complete understanding of the physics governing these systems, allowing to find the relevant parameters and identifying the presence of possible spin-sensitive proximity effect in such SFIS JJs, by comparing the simulated thermal behavior of the critical current with the experimental outcomes and then, by calculating the corresponding correlations functions in the simulated devices. Specifically, we have shown that the presence of a plateau extended over a wide range of temperatures and the peculiar non-monotonic behavior in the $I_c(T)$ is due to the combined effect of impurities and spin-mixing mechanisms, and can be explained in terms of a non-negligible triplet superconductivity contribution in these systems, which coexists with the conventional singlet-type one. These results suggest that these kinds of junctions may work as spin filtering devices, benefiting from the capability to generate controllable spin-polarized supercurrents with a single ferromagnetic layer, compared to magnetically textured JJs.
To deepen our analysis, we have also compared the outcomes deriving from the application of an external magnetic field to the experimental samples and the role of spin-mixing and disorder effect in the theoretical model. In our case, these latter mimic the magnetic ordering provided by the external magnetic field, allowing to find a relation between the effects resulting from the slight modifications arising in the microscopic structure of the barrier [176, 204–206] and the compresence of impurities, exchange field fluctuations, and spin-orbit coupling in the simulations.
Therefore, these systems may be used as a reference to classify peculiar features in a variety of structures and help orient experiments. Our study, in

fact, provides a more complex and realistic description of the thin ferromagnetic insulator barrier, which is necessary to progress towards the realization of functional interfaces for extremely advanced devices.

Appendix A

Hamiltonian and GF of the striped system

In this section we illustrate the preliminary steps preceding the application of the RGF technique for the solution of Gor'kov equation (Eq.(2.31)), that we can summarize as follows:

- definition of the Hamiltonian matrix of a single stripe;
- definition of the Hamiltonian matrix of the whole barrier (once all the single stripes have been defined);
- calculation of the GF matrix structure of the single stripe;
- calculation of the GF matrix structure of the whole barrier;
- definition of the surface GFs of the left and right superconducting leads.

We recall here that we denote with L the length of the barrier (along the x-direction) and with W its width (along y), as defined in Chapter 2.
Thus, we begin by defining the Hamiltonian of a single stripe. For simplicity, we can take as an example a generic two-site stripe, i.e. when the width of the lattice is $W = 2$, in the clean situation. By using the following representation $\psi^\dagger = \left[c^\dagger_{1\uparrow}, c^\dagger_{1\downarrow}, c^\dagger_{2\uparrow}, c^\dagger_{2\downarrow}, c_{1\uparrow}, c_{1\downarrow}, c_{2\uparrow}, c_{2\downarrow}\right]$, we can write the $4W \times 4W$ stripe matrix Hamiltonian in the Nambu $\otimes$ spin space as

$$\check{H}_{stripe\,j} = \begin{pmatrix} -\mu+h & 0 & -t_y & i\alpha_y & 0 & -\Delta & 0 & 0 \\ 0 & -\mu-h & i\alpha_y & -t_y & \Delta & 0 & 0 & 0 \\ -t_y & -i\alpha_y & -\mu+h & 0 & 0 & 0 & 0 & -\Delta \\ -i\alpha_y & -t_y & 0 & -\mu-h & 0 & 0 & \Delta & 0 \\ 0 & \Delta^* & 0 & 0 & \mu-h & 0 & t_y & i\alpha_y \\ -\Delta^* & 0 & 0 & 0 & 0 & \mu+h & i\alpha_y & t_y \\ 0 & 0 & 0 & \Delta^* & t_y & -i\alpha_y & \mu-h & 0 \\ 0 & 0 & -\Delta^* & 0 & -i\alpha_y & t_y & 0 & \mu+h \end{pmatrix} \tag{A.1}$$

where t_y and α_y are, respectively, the hopping and SOC parameters between sites in the same stripe; t_y provides the particle a non-zero probability of hopping from one site to one of the nearest neighbors. At the same time α_y provides the hopping from one site to one of the nearest neighbors with a change in its spin. Hence, the spin-orbit interaction generates spin-mixing effects. Note that in the description of the model presented in the Chapter 2 we considered the hopping and SOC constants equal for both x and y directions (i.e. $\alpha_x = \alpha_y = \alpha$ and $t_x = t_y = t$).
From the general form of the stripe Hamiltonian expressed by Eq.(A.1), we can deduce that the Hamiltonian describing a superconducting stripe (under the assumption of having no magnetization neither SOC within S) can be obtained by setting $h = 0$ and $\alpha_y = 0$, while for a normal stripe in the presence of exchange field and SOC we choose $\Delta = 0$.
The next step consists of the introduction of the Hamiltonian describing the whole barrier. In particular, this requires taking into account the interactions that couple sites belonging to different stripes, between nearest-neighbor sites along the x-direction. Since this is a nearest-neighbor tight-binding model, only "horizontal" hoppings are allowed. In our description of the barrier in terms of stripes, we include all these scattering processes by using the $4W \times 4W$ matrix $\check{T}^{\pm}$ connecting adjacent stripes and defined by Eq.(2.33), that we report here for convenience

$$\check{T}^{\pm} = \begin{pmatrix} -t & \mp\alpha & 0 & 0 & \dots \\ \pm\alpha & -t & 0 & 0 & \dots \\ \dots & \dots & \dots & \dots & \dots \\ 0 & 0 & \dots & t & \pm\alpha \\ 0 & 0 & \dots & \mp\alpha & t \end{pmatrix}, \tag{A.2}$$

meaning that the $\check{T}^{\pm}$ matrices couple in the same way all the adjacent stripes, from the left- and right-hand side, respectively.

At this point, we can define the Hamiltonian matrix of the whole barrier as

$$\mathcal{H} = \begin{pmatrix} \check{H}_{stripe\,1} & \check{T}^{+} & 0 & 0 & \dots \\ \check{T}^{-} & \check{H}_{stripe\,2} & \check{T}^{+} & 0 & \dots \\ 0 & \check{T}^{-} & \check{H}_{stripe\,3} & \check{T}^{+} & \dots \\ \dots & \dots & \dots & \dots & \dots \end{pmatrix} . \tag{A.3}$$

In particular, since the length of the barrier is L, $\mathcal{H}$ consists of L rows and L columns. Each element is a $4W \times 4W$ matrix, hence, $\mathcal{H}$ results to be a $4WL \times 4WL$ matrix.
Therefore, in order to model the barrier of a Josephson junction, we will use Eq.(A.3) by setting $\Delta = 0$.

Let us now discuss the third point of the list we have mentioned at the beginning of this section, namely the definition of the structure of the GF matrices, by starting from the GF of the single stripes.
We can formally define the GF of the single isolated stripe in the Matsubara representation as $\check{G}^0_{j,j}(\omega_n) = \left[i\omega_n \check{1} - \check{H}^0_{j,j}\right]^{-1}$, where $\check{H}^0_{j,j} = \check{H}_{stripe\,j}$ is the

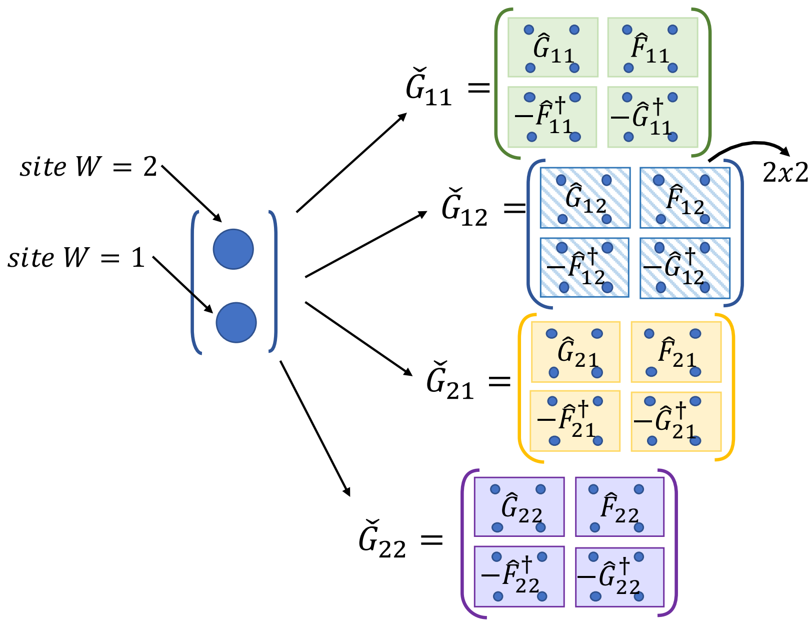

Figure 1: Schematic representation of propagators that will be used to construct the GFs of the stripe. This example refers to the case of 2 sites within the stripe ($W = 2$).

Hamiltonian of the j-th stripe, i.e. the j-th diagonal element of the Hamiltonian in Eq.(A.3). $\check{G}^0_{j,j}$ consists in a $4W \times 4W$ matrix in the Nambu $\otimes$ spin space. With a similar notation, we indicate with $\check{G}_{j,j}$ the GF of the j-th stripe when connected to both the S leads.
Furthermore, for our explanation, we indicate with $\check{G}_{k,k'}$ (with $k, k' = 1, \cdots, W$) the possible different propagators between sites within the considered stripe. As before, let us consider as an example a single stripe formed by 2 sites along the y-direction (i.e. $W = 2$). In this case, as schematically illustrated in Fig.1, we can identify four different propagators $\check{G}_{k,k'}$ (with $k, k' = 1, 2$): $\check{G}_{1,1}$, $\check{G}_{1,2}$, $\check{G}_{2,1}$, $\check{G}_{2,2}$. Each of these has a 2×2 block structure, where, in particular, we can identify four different principal blocks: $\hat{G}$, $\hat{F}$, $-\hat{F}^\dagger$, $-\hat{G}^\dagger$. Then, in turn, each block is a 2×2 GF matrix in the spin space.
At this point, by rearranging the 2×2 blocks, we can proceed with the construction of the GF describing the whole stripe, whose schematic representation is illustrated in Fig.2; here, the constituent 2×2 blocks of each certain $\check{G}_{k,k'}$ matrix are represented by elements with the same colors.
In this context, it is interesting to notice that both the GFs representing the propagators $\check{G}_{k,k'}$ and the whole stripe exhibit the same structure in terms of the four principal blocks G, F, $-F^\dagger$, $-G^\dagger$. Indeed, for the GF matrix describing the stripe, we can distinguish four $2W \times 2W$ macro-blocks (depicted by the grey areas in Fig.2).
This way of representing the GFs is useful in the calculation of the correlations functions at a certain stripe within the barrier and, at the same time,

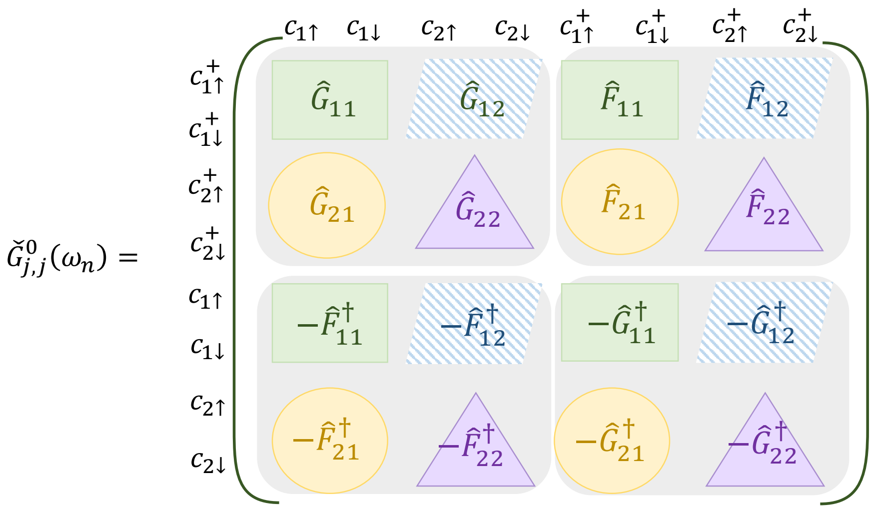

Figure 2: Block representation of the single-stripe Green's function for a stripe with 2 sites along y-direction. Different colors stand for different propagators $\check{G}_{1,1}$, $\check{G}_{1,2}$, $\check{G}_{2,1}$, $\check{G}_{2,2}$, whose structure is depicted in Fig.1. This scheme shows how we construct the GF of the single stripe.

provides a graphical explanation of the application of RGF method.
Once we have the GF of the stripes, we can reconstruct the GF of the whole barrier, by applying the RGF technique and using as input the surface GFs of the left and right superconducting lead, as illustrated in Chapter 2.
The GF of the barrier will be represented by a tridiagonal matrix with the GFs of the stripes $\check{G}_{j,j}$ as diagonal elements and the GFs that connect each stripe with the adjacent ones $\check{G}_{j,j\pm1}$ on the lower and upper diagonal.
In Fig.3, we give a pictorial representation of the GF structure of the whole junction, where the two highlighted blocks represent the surface GFs describing the S leads, which we calculate separately as illustrated in Chapter 2.

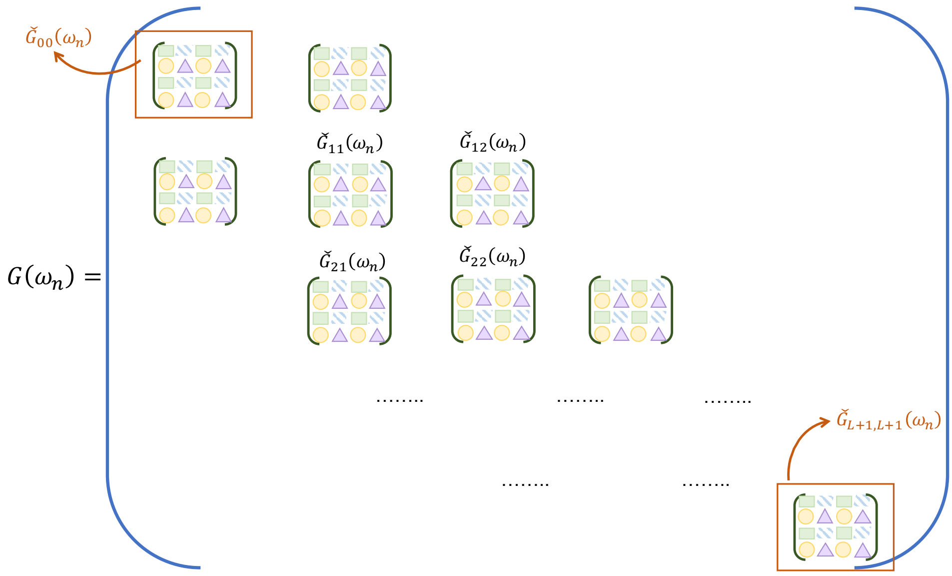

Figure 3: Block representation of the SFS junction GF. Each block consists in a $4W \times 4W$ matrix. With $\check{G}_{0,0}$ and $\check{G}_{L+1,L+1}$ we indicate the surface GF of the left and right S lead, respectively.

Appendix B

Surface Green's function of a semi-infinite normal lead

Green's functions of certain lattice systems can be obtained in analytical form, as in the case of semi-infinite lattices [94]. In the study of systems made up of two leads and one central device, e.g. the Josephson junctions, the two electrodes are usually modeled by semi-infinite lattices. In view of this, to be thorough, in this section we give a derivation of the surface GF of a semi-infinite normal lead, following the Ref. [94]. The extension of these calculations to the superconducting case is rather complicated and, therefore, in this work we only reported the results of Ref. [89].

The 1D chain

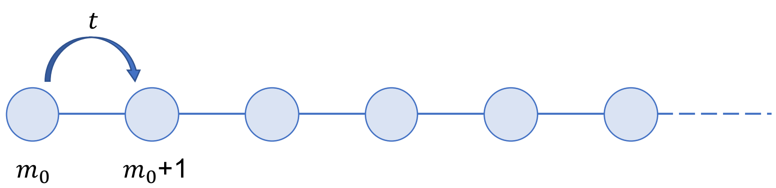

Figure 4: The semi-infinite 1D linear chain, starting at site m_0 and extending infinitely to the right. t is the hopping parameter between nearest-neighbor sites.

Let us start by considering the case of one dimensional (1D) tight-binding Hamiltonian of a semi-infinite linear chain including nearest neighbor hopping; here we consider that the chain terminates at longitudinal site m_0, and extends infinitely to the right, along the x direction, as illustrated in Fig.4. Thus, we define the Hamiltonian of the semi-infinite 1D chain as

$$H_{1D}^{semi} = \sum_{m=m_0}^{\infty} \epsilon_m c_m^\dagger c_m + t_x^m c_m^\dagger c_{m+1} + (t_x^{m-1})^* c_m^\dagger c_{m-1} \tag{B.4}$$

where ϵ_m is the on-site energy and $t_x^m = t = \frac{-\hbar^2}{2m^*}\frac{1}{a_x^2}$ is the hopping parameter between nearest-neighbor sites, considered the same all along the chain. Here, a_x is the lattice constant in the x direction and m^* is the electron effective mass; in particular, such a form of the hopping parameter ensures to recover the free-particle case in the continuum limit.
The Hamiltonian in Eq.(B.4) is written in second quantization using the fermionic site creation (annihilation) operator c_m ($c_m^\dagger$), obeying the following anticommutation relations: $\{c_m, c_{m'}^\dagger\} = \delta_{mm'}$, $\{c_m^\dagger, c_{m'}^\dagger\} = \{c_m, c_{m'}\} = 0$.
For the Hamiltonian in Eq.(B.4) the eigenvalue problem may be written as $H_{1D}^{semi}\phi_m^\mu = E^\mu \phi_m^\mu$, which substituted in Eq.(B.4) gives

$$t^*\phi_{m-1}^\mu + t\phi_{m+1}^\mu - (E^\mu - 2t)\,\phi_m^\mu = 0\,. \tag{B.5}$$

We can choose as solutions the normalized real-space eigenstates

$$\phi_m^\mu = \sqrt{\frac{2}{\pi}}\sin(\mu(m - m_0 + 1))\,, \tag{B.6}$$

obtained by imposing the hard-wall boundary condition at the left end of the chain: $\phi_{m_0-1}^\mu \equiv 0$.
Then, substituting Eq.(B.6) into Eq.(B.5) we obtain the energy dispersion relation relative to Eq.(B.4)

$$E^\mu = -2t(1 - \cos\mu) = \epsilon_m + 2t\cos\mu\,, \tag{B.7}$$

where we introduced the variable $\mu = k_x^\mu \cdot a_x$, as the product between the wave vector and the lattice constant in the longitudinal direction.
At this point, we can define the Green's function of the semi-infinite 1D linear chain as

$$G(m, m', E) = \int_0^\pi d\mu\, \frac{\phi_m^\mu (\phi_{m'}^\mu)^*}{E - E^\mu + i\eta}\,, \tag{B.8}$$

where η is an infinitesimal real positive quantity which is needed for convergence reasons.
Considering that we want to calculate the surface GF at site $m = m' = m_0$, the Eq.(B.8) becomes

$$G_{m_0}(E) = \frac{2}{\pi}\int_0^{\pi} d\mu\, \frac{\sin^2\mu}{E - E^{\mu} + i\eta}\,. \tag{B.9}$$

The elliptical integral in Eq.(B.9) can be solved by application of the residue theorem in the complex plane, integrating on the unitary circle. To do this, we firstly perform the following change of variables

$$e^{i\mu} = w\;, \qquad d\mu = \frac{1}{iw}dw\;, \tag{B.10}$$

which allows us to write the Eq.(B.9) as

$$G_{m_0} = \frac{1}{2\pi i t}\int dw \frac{(w^2-1)^2}{w^2}\frac{1}{w^2-2bw+1}\,, \tag{B.11}$$

where we have defined $b = \frac{(E+i\eta-\epsilon_m)}{2t}$.
The integrating function in Eq.(B.11) has a double pole at $w_0 = 0$ and two single poles at $w_{1,2} = b \mp \sqrt{b^2-1}$. Because only w_1 is within the chosen integration path (i.e. the unitary circle), we can apply the residue theorem as follows:

$$G_{m_0} = \frac{1}{2\pi i t}\,2\pi i\left[Res(f, w_1) + Res(f, w_0)\right]\,, \tag{B.12}$$

where

$$\begin{aligned} Res(f, w_1) &= \lim_{w\longrightarrow w_1}\frac{(w^2-1)^2}{w^2}\frac{1}{w-w_2} = \frac{(w_1^2-1)^2}{w_1^2(w_1-w_2)} \\ Res(f, w_0) &= \lim_{w\longrightarrow w_0}\frac{d}{dw}\frac{(w^2-1)^2}{(w-w_1)(w-w_2)} = \frac{w_1+w_2}{w_1^2+w_2^2}\,. \end{aligned} \tag{B.13}$$

Therefore, after substituting $w_{1,2}$ and a few algebraic steps, we obtain

$$G_{m_0} = \frac{1}{t}\left(b - \sqrt{b^2-1}\right)\,. \tag{B.14}$$

Since we are mainly interested in retarded Green's functions, when expressing G_{m_0} in Eq.(B.14) in terms of energy we have to take into account the requirement $Im\, G(E) \leqslant 0$ in the limit of $\eta \longrightarrow 0^+$. Thus, after substituting $b = \dfrac{E-\epsilon_m}{2t}$, we can rewrite the surface GF of the 1D semi-infinite chain as

$$G_{m_0}(E) = \begin{cases} \dfrac{(E-\epsilon_m)}{2t^2} + \dfrac{1}{2t^2}\sqrt{(E-\epsilon_m)^2 - 4t^2}, & \text{for } E-\epsilon_m \leq -2t \\[2ex] \dfrac{(E-\epsilon_m)}{2t^2} - \dfrac{i}{2t^2}\sqrt{4t^2 - (E-\epsilon_m)^2}, & \text{for } |E-\epsilon_m| < 2t \\[2ex] \dfrac{(E-\epsilon_m)}{2t^2} - \dfrac{1}{2t^2}\sqrt{(E-\epsilon_m)^2 - 4t^2}, & \text{for } E-\epsilon_m \geq 2t \quad . \end{cases} \tag{B.15}$$

The 2D lattice

We can generalize the procedure explained in the case of the 1D semi-infinite chain to the 2D tight-binding lattice (Fig.5). Thus, denoting with x the longitudinal direction, parallel to transport, and with y the transverse one, the general form of the lead Hamiltonian is then given as [94]

$$\begin{aligned} H_{2D}^{semi}(m_0) = \sum_{m=m_0}^{\infty}\sum_{n=1}^{N} [\varepsilon_{mn} c_{mn}^{\dagger} c_{mn} + t_x^{mn} c_{mn}^{\dagger} c_{m+1,n} + \\ t_y^{mn} c_{mn}^{\dagger} c_{m,n+1} + \left(t_x^{m-1,n}\right)^* c_{mn}^{\dagger} c_{m-1,n} + \left(t_y^{m,n-1}\right)^* c_{mn}^{\dagger} c_{m,n-1}] \end{aligned} \tag{B.16}$$

where m and n are, respectively, the indices of the lattice position in the longitudinal and transverse direction, t_x^{mn} (t_y^{mn}) is the hopping energy onto site (m, n) from its longitudinal x (transverse y) neighbor and, lastly, ϵ_{mn} represents the on-site energy [94]. As for the 1D case, we properly define the hopping energies as

$$\begin{cases} t_x = \frac{-\hbar^2}{2m^*}\frac{1}{a_x^2} \\[2ex] t_y = \frac{-\hbar^2}{2m^*}\frac{1}{a_y^2}, \end{cases} \tag{B.17}$$

where a_x (a_y) is the lattice constant in the x (y) direction and m^* is the electron effective mass.

Again, we consider the hopping energy uniform along each direction, namely $t_x^{mn} = t_x$ ($t_y^{mn} = t_y$). This choice corresponds to consider an equally spaced grid in both directions.

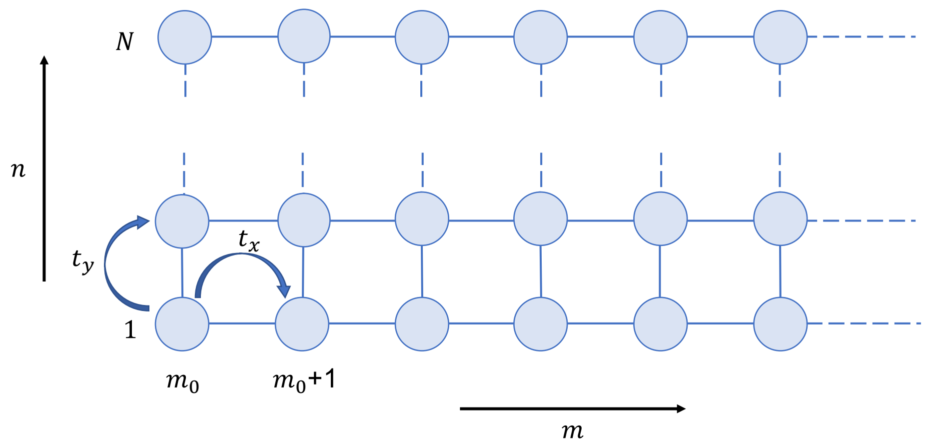

Figure 5: The semi-infinite 2D lattice, with site indices $n = 1, \cdots, N$ and $m = m_0, \cdots, \infty$. t_x and t_y are the hopping parameters between nearest-neighbor sites in the x and y direction, respectively.

At this point, we start solving the time-independent Schrödinger equation to obtain eigenvalues and eigenstates of our system. For the Hamiltonian in Eq.(B.16) the eigenvalue problem may be written as :

$$H^{semi} |\Psi^{\mu\nu}\rangle = E^{\mu\nu} |\Psi^{\mu\nu}\rangle , \tag{B.18}$$

where μ and ν are respectively the longitudinal and transverse quantum numbers of the system, and $E^{\mu\nu}$ is the energy measured with respect to the bottom of the conduction band.
The eigenstates may be expanded as follow

$$|\Psi^{\mu\nu}\rangle = \sum_{mn} u^{\mu\nu}_{mn} c^{\dagger}_{mn} |0\rangle , \tag{B.19}$$

where $|0\rangle$ is the vacuum state and the expansion coefficients are given by: $u^{\mu\nu}_{mn} = \langle 0| c_{mn} |\Psi^{\mu\nu}\rangle$. Substituting Eq.(B.19) in the Eq.(B.18), we find a set of coupled equations for the coefficients $u^{\mu\nu}_{mn}$

$$t^*_x u^{\mu\nu}_{m-1,n} + t_x u^{\mu\nu}_{m+1,n} + t^*_y u^{\mu\nu}_{m,n-1} + t_x u^{\mu\nu}_{m,n+1} = \left(E^{\mu\nu} - \varepsilon_{mn}\right) u^{\mu\nu}_{mn} , \tag{B.20}$$

where we are we implicitly assuming $m > m_0$. As a further simplification, we suppose that the eigenvalue problem has a separable solution. Hence, we can divide the dependence on the indices (m,n) and (μ,ν) in the expressions for the eigenvalue energies $E^{\mu\nu}$ and coefficients $u^{\mu\nu}_{mn}$

$$u^{\mu\nu}_{mn} = \phi^{\mu}_{m} \cdot \chi^{\nu}_{n}, \qquad E^{\mu\nu} = E^{\mu} + E^{\nu}, \tag{B.21}$$

where ϕ^{μ}_{m} and χ^{ν}_{n} represent the longitudinal and transverse wave function, respectively.

Therefore, the Eq.(B.20) splits into longitudinal and transverse parts:

$$\begin{aligned} t_x^*\phi_{m-1}^{\mu} + t_x\phi_{m+1}^{\mu} - (E^{\mu} - 2t_x)\,\phi_m^{\mu} = 0 \\ t_y^*\chi_{n-1}^{\nu} + t_y\chi_{n+1}^{\nu} - (E^{\nu} - 2t_y)\,\chi_n^{\nu} = 0. \end{aligned} \tag{B.22}$$

As for the 1D chain, also for the 2D semi-infinite lattice, in order to find a solution for ϕ_m^{μ} and χ_n^{ν}, we choose functions that satisfy the hard-wall boundary conditions, i.e. the wave-functions must vanish at the left-end $m = m_0 - 1$ and at the lateral edges of the lead $n = 0$, $n = N + 1$. Hence, in addition to the longitudinal wave function we have also used in the 1D case $\phi_m^{\mu} = \sqrt{\frac{2}{\pi}} \cdot \sin\left(\mu\left(m - m_0 + 1\right)\right)$, with $\mu = k_x^{\mu} \cdot a_x$ and longitudinal energy dispersion relation $E^{\mu} = -2t_x \cdot (1 - \cos\mu)$, in the generalization to the 2D lattice we have to add the conditions for the transverse wave function $\chi_0^{\nu} \equiv \chi_{N+1}^{\nu} \equiv 0$, yielding

$$\chi_n^{\nu} = \sqrt{\frac{2}{N+1}} \cdot \sin\left(\frac{\pi\nu n}{N+1}\right); \tag{B.23}$$

with $\nu = 1, \ldots, N$ as discrete mode number of the transverse wave function. For the energy dispersion relation, after substituting the Eq.(B.23) into the second of Eqs.(B.22), we obtain

$$E^{\nu} = -2t_y \cdot \left(1 - \cos\left(\frac{\pi\nu}{N+1}\right)\right). \tag{B.24}$$

Therefore, the total energy dispersion relation reads:

$$E^{\mu\nu} = -2\left(t_x + t_y\right) + 2t_x\cos\mu + 2t_y\cos\left(\frac{\pi\nu}{N+1}\right), \tag{B.25}$$

and the solutions of the time-independent Schrödinger equation are:

$$\left|\Psi^{\mu\nu}\right\rangle = \sum_{mn} \phi_m^{\mu}\,\chi_n^{\nu}\,c_{mn}^{\dagger}\left|0\right\rangle. \tag{B.26}$$

With the above definition of the eigenstates, the retarded Green's function of the system can be written as

$$G\left(m, n, m', n'; E\right) = G_{m,m'}\left(n, n'\right) = \sum_{\mu\nu} \frac{c_{mn}^{\dagger}\left|\Psi^{\mu\nu}\right\rangle\left\langle\Psi^{\mu\nu}\right| c_{m',n'}}{E - E^{\mu\nu} + i\eta}. \tag{B.27}$$

Inserting the known eigenstates in Eq.(B.26) into Eq.(B.27), the GF becomes

$$G_{m,m'}\left(n, n', E\right) = \int_0^{\pi} d\mu \sum_{\nu=1}^{N} \frac{\phi_m^{\mu}\left(\phi_{m'}^{\mu}\right)^*\chi_n^{\nu}\left(\chi_{n'}^{\nu}\right)^*}{E - E^{\mu\nu} + i\eta}. \tag{B.28}$$

Since we are interested in calculating the surface Green's function of the lead, we only look at GF obtained for $m = m' = m_0$

$$G_{m_0}\left(n, n', E\right) = \sum_{\nu=1}^{N} \chi_n^{\nu} \left(\chi_{n'}^{\nu}\right)^* \cdot \frac{2}{\pi} \int_0^{\pi} d\mu \, \frac{\sin^2 \mu}{E - \left(E^{\mu} + E^{\nu}\right) + i\eta} = G^{semi} \,. \tag{B.29}$$

Defining the parameters p and q as follows

$$p = E + i\eta + 2\left(t_x + t_y\right) - 2t_y \cos\left(\frac{\pi\nu}{N+1}\right), \tag{B.30}$$
$$q = -2t_x \,,$$

the integral over the continuous variable μ in Eq.(B.29) has the same form as that calculated for the 1D chain (Eq.(B.9)) and may be evaluated analogously, obtaining

$$\frac{2}{\pi} \int_0^{\pi} d\mu \frac{\sin^2\left(\mu\right)}{p + q\cos\mu} = \frac{2p}{q^2}\left(1 - \sqrt{1 - \frac{q^2}{p^2}}\right) = \tilde{G}(\nu) \,. \tag{B.31}$$

Hence, the final expression for the surface Green's function of the lead is obtained by substituting $\tilde{G}(\nu)$ in the Eq.(B.29)

$$G^{semi} = \frac{2}{N+1} \sum_{\nu=1}^{N} \sin\left(\frac{\pi\nu n}{N+1}\right) \sin\left(\frac{\pi\nu n'}{N+1}\right) \tilde{G}(\nu) \,. \tag{B.32}$$

We can thus notice that, the lattice Green's function in Eq.(B.29) may be written as a transformation of $\tilde{G}(\nu)$ if we introduce a transformation matrix U, whose columns are simply the transverse wave functions χ_n^{ν} [94]

$$U \equiv \left(\chi_n^1 \,|\, \chi_n^2 \,|\, \cdots \,|\, \chi_n^N\right) \,. \tag{B.33}$$

Therefore, the lattice Green's function may then be expressed as

$$G^{semi} = U\tilde{G}(\nu)U^{\dagger} \,, \tag{B.34}$$

where it can be shown that the U matrices are unitary ($UU^{\dagger} = U^{\dagger}U = 1$). Thus, Eq.(B.34) defines the unitary transformation that converts the Green's function $\tilde{G}(\nu)$ in the transverse mode representation into G^{semi} in the site representation (or vice versa, $\tilde{G}(\nu) = U^{\dagger}G^{semi}U$).

We conclude this section by noticing that, by making the parameters p and q (Eqs.(B.30)) explicit, it is possible to re-express the Eq.(B.31) as a function of energy, yielding

$$\tilde{G}(\nu, E) = \frac{\left(E - \epsilon_{\nu}\right)}{2t_x^2} \pm \sqrt{\frac{\left(E - \epsilon_{\nu}\right)^2}{4t_x^4} - \frac{1}{t_x^2}} \,, \tag{B.35}$$

where we defined $\epsilon_\nu = -2(t_x + t_y) + 2t_y \cos\left(\frac{\pi\nu}{N+1}\right)$.
Finally, the condition of considering the imaginary part of the retarded GF as negative, $Im\, G \leq 0$, allows to eliminate the ambiguity in the sign in front of the square root, obtaining

$$\tilde{G}(\nu, E) = \begin{cases} \dfrac{(E-\epsilon_\nu)}{2t_x^2} + \sqrt{\dfrac{(E-\epsilon_\nu)^2}{4t_x^4} - \dfrac{1}{t_x^2}}, & \text{for } E - \epsilon_\nu \leq -2t_x \\[2ex] \dfrac{(E-\epsilon_\nu)}{2t^2} - i\sqrt{\dfrac{1}{t_x^2} - \dfrac{(E-\epsilon_\nu)^2}{4t_x^4}}, & \text{for } |E - \epsilon_\nu| < 2t_x \\[2ex] \dfrac{(E-\epsilon_\nu)}{2t_x^2} - \sqrt{\dfrac{(E-\epsilon_\nu)^2}{4t_x^4} - \dfrac{1}{t_x^2}}, & \text{for } E - \epsilon_\nu \geq 2t_x \quad , \end{cases} \tag{B.36}$$

showing the analogy with Eqs.(B.15) obtained in the 1D case.

Bibliography

[1] J. Bardeen, L. N. Cooper, and J. R. Schrieffer, "Theory of superconductivity," *Phys. Rev.*, vol. 108, pp. 1175–1204, Dec 1957.

[2] J. Bardeen, L. N. Cooper, and J. R. Schrieffer, "Microscopic theory of superconductivity," *Phys. Rev.*, vol. 106, pp. 162–164, Apr 1957.

[3] L. N. Cooper, "Bound electron pairs in a degenerate fermi gas," *Phys. Rev.*, vol. 104, pp. 1189–1190, Nov 1956.

[4] B. T. Matthias, H. Suhl, and E. Corenzwit, "Spin exchange in superconductors," *Phys. Rev. Lett.*, vol. 1, pp. 152–152, Aug 1958.

[5] P. W. Anderson and H. Suhl, "Spin alignment in the superconducting state," *Phys. Rev.*, vol. 116, pp. 898–900, Nov 1959.

[6] H. Suhl and B. T. Matthias, "Impurity scattering in superconductors," *Phys. Rev.*, vol. 114, pp. 977–988, May 1959.

[7] R. Meservey and P. Tedrow, "Spin-polarized electron tunneling," *Physics Reports*, vol. 238, pp. 173–243, Mar. 1994.

[8] A. A. Abrikosov and L. P. Gor'kov, "Contribution to the theory of superconducting alloys with paramagnetic impurities," *Zhur. Eksptl'. i Teoret. Fiz.*, vol. 39, 12 1960.

[9] B. S. Chandrasekhar, "A note on the maximum critical field of high-field superconductors," *Applied Physics Letters*, vol. 1, pp. 7–8, Sept. 1962.

[10] A. M. Clogston, "Upper limit for the critical field in hard superconductors," *Phys. Rev. Lett.*, vol. 9, pp. 266–267, Sep 1962.

[11] G. Sarma, "On the influence of a uniform exchange field acting on the spins of the conduction electrons in a superconductor," *Journal of Physics and Chemistry of Solids*, vol. 24, pp. 1029–1032, Aug. 1963.

[12] K. Maki and T. Tsuneto, "Pauli paramagnetism and superconducting state," *Progress of Theoretical Physics*, vol. 31, pp. 945–956, June 1964.

[13] P. G. De Gennes, "Boundary effects in superconductors," *Rev. Mod. Phys.*, vol. 36, pp. 225–237, Jan 1964.

[14] G. Deutscher and P. G. de Gennes, "Proximity effects," *pp 1005-34 of Superconductivity. Vols. 1 and 2. Parks, R. D. (ed.). New York, Marcel Dekker, Inc., 1969.*, 10 1969.

[15] A. I. Buzdin, "Proximity effects in superconductor-ferromagnet heterostructures," *Rev. Mod. Phys.*, vol. 77, pp. 935–976, Sep 2005.

[16] Y. A. Izyumov, Y. N. Proshin, and M. G. Khusainov, "Competition between superconductivity and magnetism in ferromagnet/superconductor heterostructures," *Physics-Uspekhi*, vol. 45, pp. 109–148, feb 2002.

[17] A. A. Golubov, M. Y. Kupriyanov, and E. Il'ichev, "The current-phase relation in josephson junctions," *Rev. Mod. Phys.*, vol. 76, pp. 411–469, Apr 2004.

[18] I. F. Lyuksyutov and V. L. Pokrovsky, "Ferromagnet-superconductor hybrids," *Advances in Physics*, vol. 54, pp. 67–136, Jan 2005.

[19] F. S. Bergeret, A. F. Volkov, and K. B. Efetov, "Odd triplet superconductivity and related phenomena in superconductor-ferromagnet structures," *Rev. Mod. Phys.*, vol. 77, pp. 1321–1373, Nov 2005.

[20] E. A. Demler, G. B. Arnold, and M. R. Beasley, "Superconducting proximity effects in magnetic metals," *Phys. Rev. B*, vol. 55, pp. 15174–15182, Jun 1997.

[21] F. S. Bergeret, A. F. Volkov, and K. B. Efetov, "Long-range proximity effects in superconductor-ferromagnet structures," *Phys. Rev. Lett.*, vol. 86, pp. 4096–4099, Apr 2001.

[22] A. Bagrets, C. Lacroix, and A. Vedyayev, "Theory of proximity effect in superconductor/ferromagnet heterostructures," *Phys. Rev. B*, vol. 68, p. 054532, Aug 2003.

[23] F. Perez-Willard, J. C. Cuevas, C. Surgers, P. Pfundstein, J. Kopu, M. Eschrig, and H. v. Lohneysen, "Determining the current polarization in al/co nanostructured point contacts," *Phys. Rev. B*, vol. 69, p. 140502, Apr 2004.

[24] V. T. Petrashov, I. A. Sosnin, I. Cox, A. Parsons, and C. Troadec, "Giant mutual proximity effects in ferromagnetic/superconducting nanostructures," *Phys. Rev. Lett.*, vol. 83, pp. 3281–3284, Oct 1999.

[25] T. Kontos, M. Aprili, J. Lesueur, and X. Grison, "Inhomogeneous superconductivity induced in a ferromagnet by proximity effect," *Phys. Rev. Lett.*, vol. 86, pp. 304–307, Jan 2001.

[26] P. Fulde and R. A. Ferrell, "Superconductivity in a strong spin-exchange field," *Phys. Rev.*, vol. 135, pp. A550–A563, Aug 1964.

[27] A. Larkin and Y. Ovchinnikov, "Nonuniform state of superconductors," *Zh.Eksp.Teor.Fiz. 47 (1964) 1136-1146, Sov.Phys.JETP 20 (1965) 762*, 1964.

[28] A. Buzdin, "π-junction realization due to tunneling through a thin ferromagnetic layer," *Journal of Experimental and Theoretical Physics Letters*, vol. 78, p. 583, Nov 2003.

[29] L. Bulaevskii, V. Kuzii, and S. A.A., "Superconducting system with weak coupling to the current in the ground state," *JETP Lett.*, vol. 25, 1977.

[30] V. V. Ryazanov, V. A. Oboznov, A. Y. Rusanov, A. V. Veretennikov, A. A. Golubov, and J. Aarts, "Coupling of two superconductors through a ferromagnet: Evidence for a π junction," *Phys. Rev. Lett.*, vol. 86, pp. 2427–2430, Mar 2001.

[31] V. A. Oboznov, V. V. Bol'ginov, A. K. Feofanov, V. V. Ryazanov, and A. I. Buzdin, "Thickness dependence of the josephson ground states of superconductor-ferromagnet-superconductor junctions," *Phys. Rev. Lett.*, vol. 96, p. 197003, May 2006.

[32] H. Sellier, C. Baraduc, F. m. c. Lefloch, and R. Calemczuk, "Temperature-induced crossover between 0 and π states in s/f/s junctions," *Phys. Rev. B*, vol. 68, p. 054531, Aug 2003.

[33] A. Buzdin and I. Baladie, "Theoretical description of ferromagnetic π junctions near the critical temperature," *Phys. Rev. B*, vol. 67, p. 184519, May 2003.

[34] T. Kontos, M. Aprili, J. Lesueur, F. Genêt, B. Stephanidis, and R. Boursier, "Josephson junction through a thin ferromagnetic layer: Negative coupling," *Phys. Rev. Lett.*, vol. 89, p. 137007, Sep 2002.

[35] H. Sellier, C. Baraduc, F. Lefloch, and R. Calemczuk, "Half-integer shapiro steps at the $0-\pi$ crossover of a ferromagnetic josephson junction," *Phys. Rev. Lett.*, vol. 92, p. 257005, Jun 2004.

[36] L. B. Ioffe, M. V. Feigel'man, A. Ioselevich, D. Ivanov, M. Troyer, and G. Blatter, "Topologically protected quantum bits using josephson junction arrays," *Nature*, vol. 415, pp. 503–506, Jan 2002.

[37] T. Ortlepp, T. Ortlepp, A. Ariando, O. Mielke, C. Verwijs, K. Foo, H. Rogalla, F. Uhlmann, and J. Hilgenkamp, "Flip-flopping fractional flux quanta," *Science*, vol. 312, no. 5779, pp. 1495–, 2006. Originally published in Science Express on 20 April 2006.

[38] J. Baselmans, A. Morpurgo, B. van Wees, and T. Klapwijk, "Tunable supercurrent in superconductor/normal metal/superconductor josephson junctions," *Superlattices and Microstructures*, vol. 25, no. 5, pp. 973–982, 1999.

[39] T. Yamashita, K. Tanikawa, S. Takahashi, and S. Maekawa, "Superconducting π qubit with a ferromagnetic josephson junction," *Phys. Rev. Lett.*, vol. 95, p. 097001, Aug 2005.

[40] T. Yamashita, S. Kim, H. Kato, W. Qiu, K. Semba, A. Fujimaki, and H. Terai, "π phase shifter based on nbn-based ferromagnetic josephson junction on a silicon substrate," *Scientific Reports*, vol. 10, no. 1, p. 13687, 2020.

[41] M. Eschrig, T. Lofwander, T. Champel, J. C. Cuevas, J. Kopu, and G. Schon, "Symmetries of pairing correlations in superconductor-ferromagnet nanostructures," *Journal of Low Temperature Physics*, vol. 147, pp. 457–476, Feb 2007.

[42] M. Eschrig and T. Lofwander, "Triplet supercurrents in clean and disordered half-metallic ferromagnets," *Nature Physics*, vol. 4, p. 138, Jan 2008.

[43] T. Löfwander, R. Grein, and M. Eschrig, "Is cro_2 fully spin polarized? analysis of andreev spectra and excess current," *Phys. Rev. Lett.*, vol. 105, p. 207001, Nov 2010.

[44] A. Kadigrobov, R. I. Shekhter, and M. Jonson, "Triplet superconducting proximity effect in inhomogeneous magnetic materials," *Low Temperature Physics*, vol. 27, no. 9, pp. 760–766, 2001.

[45] A. F. Volkov, F. S. Bergeret, and K. B. Efetov, "Odd triplet superconductivity in superconductor-ferromagnet multilayered structures," *Phys. Rev. Lett.*, vol. 90, p. 117006, Mar 2003.

[46] M. Houzet and A. I. Buzdin, "Long range triplet josephson effect through a ferromagnetic trilayer," *Phys. Rev. B*, vol. 76, p. 060504, Aug 2007.

[47] M. Eschrig, "Spin-polarized supercurrents for spintronics: A marriage between superconductivity and ferromagnetism is opening the door for new spin-based applications," *Physics Today*, vol. 64, pp. 43–49, Jan. 2011.

[48] J. W. A. Robinson, J. D. S. Witt, and M. G. Blamire, “Controlled injection of spin-triplet supercurrents into a strong ferromagnet,” *Science*, vol. 329, pp. 59–61, July 2010.

[49] T. S. Khaire, M. A. Khasawneh, W. P. Pratt, and N. O. Birge, “Observation of spin-triplet superconductivity in co-based josephson junctions,” *Phys. Rev. Lett.*, vol. 104, p. 137002, Mar 2010.

[50] C. Klose, T. S. Khaire, Y. Wang, W. P. Pratt, N. O. Birge, B. J. McMorran, T. P. Ginley, J. A. Borchers, B. J. Kirby, B. B. Maranville, and J. Unguris, “Optimization of spin-triplet supercurrent in ferromagnetic josephson junctions,” *Phys. Rev. Lett.*, vol. 108, Mar. 2012.

[51] J. W. A. Robinson, G. B. Halász, A. I. Buzdin, and M. G. Blamire, “Enhanced supercurrents in josephson junctions containing nonparallel ferromagnetic domains,” *Phys. Rev. Lett.*, vol. 104, p. 207001, May 2010.

[52] P. V. Leksin, N. N. Garif’yanov, I. A. Garifullin, Y. V. Fominov, J. Schumann, Y. Krupskaya, V. Kataev, O. G. Schmidt, and B. Büchner, “Evidence for triplet superconductivity in a superconductor-ferromagnet spin valve,” *Phys. Rev. Lett.*, vol. 109, p. 057005, Aug 2012.

[53] J. D. S. Witt, J. W. A. Robinson, and M. G. Blamire, “Josephson junctions incorporating a conical magnetic holmium interlayer,” *Phys. Rev. B*, vol. 85, p. 184526, May 2012.

[54] N. Banerjee, C. B. Smiet, R. G. J. Smits, A. Ozaeta, F. S. Bergeret, M. G. Blamire, and J. W. A. Robinson, “Evidence for spin selectivity of triplet pairs in superconducting spin valves,” *Nature Communications*, vol. 5, Jan. 2014.

[55] J. W. A. Robinson, N. Banerjee, and M. G. Blamire, “Triplet pair correlations and nonmonotonic supercurrent decay with cr thickness in nb/cr/fe/nb josephson devices,” *Phys. Rev. B*, vol. 89, p. 104505, Mar 2014.

[56] A. I. Buzdin, L. N. Bulaevskii, and S. V. Panyukov, “Critical-current oscillations as a function of the exchange field and thickness of the ferromagnetic metal (f) in an s-f-s josephson junction,” *JETP Lett. (Engl. Transl.); (United States)*, 2 1982.

[57] M. G. Blamire and J. W. A. Robinson, “The interface between superconductivity and magnetism: understanding and device prospects,” *Journal of Physics: Condensed Matter*, vol. 26, p. 453201, oct 2014.

[58] A. Zaikin, “Quantum coherent effects in josephson junctions and granular superconductors,” *Physica B: Condensed Matter*, vol. 152, no. 1, pp. 251–256, 1988.

[59] T. Kato, A. A. Golubov, and Y. Nakamura, “Decoherence in a superconducting flux qubit with a π-junction,” *Phys. Rev. B*, vol. 76, p. 172502, Nov 2007.

[60] A. A. Bannykh, J. Pfeiffer, V. S. Stolyarov, I. E. Batov, V. V. Ryazanov, and M. Weides, “Josephson tunnel junctions with a strong ferromagnetic interlayer,” *Phys. Rev. B*, vol. 79, p. 054501, Feb 2009.

[61] G. Wild, C. Probst, A. Marx, and R. Gross, “Josephson coupling and fiske dynamics in ferromagnetic tunnel junctions,” *The European Physical Journal B*, vol. 78, pp. 509–523, Dec. 2010.

[62] S. Kawabata, S. Kashiwaya, Y. Asano, Y. Tanaka, and A. A. Golubov, “Macroscopic quantum dynamics of π junctions with ferromagnetic insulators,” *Phys. Rev. B*, vol. 74, p. 180502, Nov 2006.

[63] S. Kawabata and Y. Asano, “Theory of quantum transport in josephson junctions with a ferromagnetic insulator,” *Low Temperature Physics*, vol. 36, no. 10, pp. 915–919, 2010.

[64] A. K. Feofanov, V. A. Oboznov, V. V. Bol’ginov, J. Lisenfeld, S. Poletto, V. V. Ryazanov, A. N. Rossolenko, M. Khabipov, D. Balashov, A. B. Zorin, P. N. Dmitriev, V. P. Koshelets, and A. V. Ustinov, “Implementation of superconductor/ferromagnet/ superconductor π-shifters in superconducting digital and quantum circuits,” *Nature Physics*, vol. 6, pp. 593–597, June 2010.

[65] Y. Zhu, A. Pal, M. G. Blamire, and Z. H. Barber, “Superconducting exchange coupling between ferromagnets,” *Nature Materials*, vol. 16, pp. 195–199, Sept. 2016.

[66] K. Senapati, M. G. Blamire, and Z. H. Barber, “Spin-filter josephson junctions,” *Nature Materials*, vol. 10, pp. 849–852, Sept. 2011.

[67] R. Caruso, D. Massarotti, G. Campagnano, A. Pal, H. G. Ahmad, P. Lucignano, M. Eschrig, M. G. Blamire, and F. Tafuri, “Tuning of magnetic activity in spin-filter josephson junctions towards spin-triplet transport,” *Phys. Rev. Lett.*, vol. 122, p. 047002, Feb 2019.

[68] H. G. Ahmad, M. Minutillo, R. Capecelatro, A. Pal, R. Caruso, G. Passarelli, M. G. Blamire, F. Tafuri, P. Lucignano, and D. Massarotti, “Coexistence and tuning of spin-singlet and triplet transport in spin-filter josephson junctions,” *Communications Physics*, vol. 5, Jan. 2022.

[69] Y. Tanaka and S. Kashiwaya, "Theory of josephson effect in superconductor-ferromagnetic-insulator-superconductor junction," *Physica C: Superconductivity*, vol. 274, no. 3, pp. 357–363, 1997.

[70] M. Tinkham, *Introduction to Superconductivity.* Dover Publications, 2 ed., jun 2004.

[71] A. Barone and G. Paternò, *Physics and applications of the Josephson effect.* UMI Out-of-Print Books on Demand, Wiley, 1982.

[72] C. Bell, G. Burnell, C. W. Leung, E. J. Tarte, D.-J. Kang, and M. G. Blamire, "Controllable josephson current through a pseudospin-valve structure," *Applied Physics Letters*, vol. 84, pp. 1153–1155, Feb. 2004.

[73] B. Baek, W. H. Rippard, S. P. Benz, S. E. Russek, and P. D. Dresselhaus, "Hybrid superconducting-magnetic memory device using competing order parameters," *Nature communications*, vol. 5, no. 1, pp. 1–6, 2014.

[74] M. Abd El Qader, R. Singh, S. N. Galvin, L. Yu, J. Rowell, and N. Newman, "Switching at small magnetic fields in josephson junctions fabricated with ferromagnetic barrier layers," *Applied Physics Letters*, vol. 104, no. 2, p. 022602, 2014.

[75] B. Baek, W. H. Rippard, M. R. Pufall, S. P. Benz, S. E. Russek, H. Rogalla, and P. D. Dresselhaus, "Spin-transfer torque switching in nanopillar superconducting-magnetic hybrid josephson junctions," *Physical Review Applied*, vol. 3, no. 1, p. 011001, 2015.

[76] A. Ustinov and V. Kaplunenko, "Rapid single-flux quantum logic using π-shifters," *Journal of Applied Physics*, vol. 94, no. 8, pp. 5405–5407, 2003.

[77] M. Khabipov, D. Balashov, F. Maibaum, A. Zorin, V. Oboznov, V. Bolginov, A. Rossolenko, and V. Ryazanov, "A single flux quantum circuit with a ferromagnet-based josephson π-junction," *Superconductor Science and Technology*, vol. 23, no. 4, p. 045032, 2010.

[78] G. Blatter, V. B. Geshkenbein, and L. B. Ioffe, "Design aspects of superconducting-phase quantum bits," *Phys. Rev. B*, vol. 63, p. 174511, Apr 2001.

[79] L. B. Ioffe, V. B. Geshkenbein, M. V. FeigelâĂŹman, A. L. FauchÃĺre, and G. Blatter, "Environmentally decoupled sds -wave josephson junctions for quantum computing," *Nature*, vol. 398, pp. 679–681, Apr 1999.

[80] J. B. Majer, J. R. Butcher, and J. E. Mooij, “Simple phase bias for superconducting circuits,” *Applied Physics Letters*, vol. 80, no. 19, pp. 3638–3640, 2002.

[81] D. Balashov, B. Dimov, M. Khabipov, T. Ortlepp, D. Hagedorn, A. B. Zorin, F.-I. Buchholz, F. H. Uhlmann, and J. Niemeyer, “Passive phase shifter for superconducting josephson circuits,” *IEEE Transactions on Applied Superconductivity*, vol. 17, no. 2, pp. 142–145, 2007.

[82] S. Kawabata, Y. Asano, Y. Tanaka, A. A. Golubov, and S. Kashiwaya, “Josephson π state in a ferromagnetic insulator,” *Phys. Rev. Lett.*, vol. 104, p. 117002, Mar 2010.

[83] A. Pal, Z. Barber, J. Robinson, and M. Blamire, “Pure second harmonic current-phase relation in spin-filter josephson junctions,” *Nature Communications*, vol. 5, Feb. 2014.

[84] A. Pal, J. A. Ouassou, M. Eschrig, J. Linder, and M. G. Blamire, “Spectroscopic evidence of odd frequency superconducting order,” *Scientific Reports*, vol. 7, Jan. 2017.

[85] T. S. Khaire, M. A. Khasawneh, W. P. Pratt, and N. O. Birge, “Observation of spin-triplet superconductivity in co-based josephson junctions,” *Phys. Rev. Lett.*, vol. 104, p. 137002, Mar 2010.

[86] J. Linder and J. W. A. Robinson, “Superconducting spintronics,” *Nature Physics*, vol. 11, pp. 307–315, Apr. 2015.

[87] M. Eschrig, “Spin-polarized supercurrents for spintronics: a review of current progress,” *Reports on Progress in Physics*, vol. 78, p. 104501, Sep 2015.

[88] W. M. Martinez, W. P. Pratt, and N. O. Birge, “Amplitude control of the spin-triplet supercurrent in $s/f/s$ josephson junctions,” *Phys. Rev. Lett.*, vol. 116, p. 077001, Feb 2016.

[89] A. Furusaki, “Dc josephson effect in dirty sns junctions: Numerical study,” *Physica B: Condensed Matter*, vol. 203, no. 3, pp. 214 – 218, 1994.

[90] T. Yamashita, J. Lee, T. Habe, and Y. Asano, “Proximity effect in a ferromagnetic semiconductor with spin-orbit interactions,” *Phys. Rev. B*, vol. 100, p. 094501, Sep 2019.

[91] Y. Asano, “Numerical method for dc josephson current between d-wave superconductors,” *Phys. Rev. B*, vol. 63, p. 052512, Jan 2001.

[92] W. Belzig, F. K. Wilhelm, C. Bruder, G. SchÃűn, and A. D. Zaikin, "Quasiclassical green's function approach to mesoscopic superconductivity," *Superlattices and Microstructures*, vol. 25, no. 5, pp. 1251–1288, 1999.

[93] C. J. Lambert and R. Raimondi, "Phase-coherent transport in hybrid superconducting nanostructures," *Journal of Physics: Condensed Matter*, vol. 10, pp. 901–941, feb 1998.

[94] D. K. Ferry, S. Goodnick, and J. Bird, *Transport in Nanostructures*. Cambridge University Press, 2009.

[95] A. I. Buzdin and M. Y. Kupriyanov, "Transition temperature of a superconductor-ferromagnet superlattice," *ZhETF Pisma Redaktsiiu*, vol. 52, p. 1089, Nov. 1990.

[96] Z. Radović, M. Ledvij, L. Dobrosavljević-Grujić, A. I. Buzdin, and J. R. Clem, "Transition temperatures of superconductor-ferromagnet superlattices," *Phys. Rev. B*, vol. 44, pp. 759–764, Jul 1991.

[97] J. S. Jiang, D. Davidović, D. H. Reich, and C. L. Chien, "Oscillatory superconducting transition temperature in nb/gd multilayers," *Phys. Rev. Lett.*, vol. 74, pp. 314–317, Jan 1995.

[98] L. V. Mercaldo, C. Attanasio, C. Coccorese, L. Maritato, S. L. Prischepa, and M. Salvato, "Superconducting-critical-temperature oscillations in nb/CuMn multilayers," *Phys. Rev. B*, vol. 53, pp. 14040–14042, 6 1996.

[99] A. Sidorenko, V. Zdravkov, A. Prepelitsa, C. Helbig, Y. Luo, S. Gsell, M. Schreck, S. Klimm, S. Horn, L. Tagirov, and R. Tidecks, "Oscillations of the critical temperature in superconducting nb/ni bilayers," *Annalen der Physik*, vol. 12, pp. 37–50, 3 2003.

[100] I. A. Garifullin, D. A. Tikhonov, N. N. Garif'yanov, L. Lazar, Y. V. Goryunov, S. Y. Khlebnikov, L. R. Tagirov, K. Westerholt, and H. Zabel, "Re-entrant superconductivity in the superconductor/ferromagnet v/fe layered system," *Phys. Rev. B*, vol. 66, p. 020505, Jul 2002.

[101] L. Lazar, K. Westerholt, H. Zabel, L. R. Tagirov, Y. V. Goryunov, N. N. Garif'yanov, and I. A. Garifullin, "Superconductor/ferromagnet proximity effect in fe/pb/fe trilayers," *Phys. Rev. B*, vol. 61, pp. 3711–3722, Feb 2000.

[102] Y. Obi, M. Ikebe, H. Wakou, and H. Fujimori, "Superconducting transition temperature and dimensional crossover in nb/co and v/co mul-

tilayers," *Journal of the Physical Society of Japan*, vol. 68, pp. 2750–2754, Aug. 1999.

[103] L. W. Gruenberg and L. Gunther, "Fulde-ferrell effect in type-ii superconductors," *Phys. Rev. Lett.*, vol. 16, pp. 996–998, May 1966.

[104] Y. Matsuda and H. Shimahara, "Fulde ferrell larkin ovchinnikov state in heavy fermion superconductors," *JPS Journals*, vol. 76, p. 051005, May 2007.

[105] R. Beyer and J. Wosnitza, "Emerging evidence for FFLO states in layered organic superconductors (review article)," *Low Temperature Physics*, vol. 39, pp. 225–231, Mar. 2013.

[106] K. Machida and H. Nakanishi, "Superconductivity under a ferromagnetic molecular field," *Phys. Rev. B*, vol. 30, pp. 122–133, Jul 1984.

[107] H. Shimahara, "Fulde-ferrell state in quasi-two-dimensional superconductors," *Phys. Rev. B*, vol. 50, pp. 12760–12765, Nov 1994.

[108] N. Dupuis, "Larkin-ovchinnikov-fulde-ferrell state in quasi-one-dimensional superconductors," *Phys. Rev. B*, vol. 51, pp. 9074–9083, Apr 1995.

[109] M. D. Croitoru and A. I. Buzdin, "Peculiarities of the orbital effect in the fulde-ferrell-larkin-ovchinnikov state in quasi-one-dimensional superconductors," *Phys. Rev. B*, vol. 89, p. 224506, Jun 2014.

[110] S. Takada, "Superconductivity in a Molecular Field. II: Stability of Fulde-Ferrel Phase," *Progress of Theoretical Physics*, vol. 43, pp. 27–38, 01 1970.

[111] L. Aslamazov, "Influence of impurities on the existence of an inhomogeneous state in a ferromagnetic superconductor," *JETP Lett. (Engl. Transl.)*, vol. 28, pp. 773–775, 1969.

[112] L. Bulaevskii, "Magnetic properties of layered superconductors with weak interaction between the layers," *JETP Lett.*, vol. 37, pp. 1133–1136, 1973.

[113] H. Burkhardt and D. Rainer, "Fulde-ferrell-larkin-ovchinnikov state in layered superconductors," *adp*, vol. 506, no. 3, pp. 181–194, 1994.

[114] Buzdin, A. I. and Brison, J. P., "Non-uniform state in 2d superconductors," *Europhys. Lett.*, vol. 35, no. 9, pp. 707–712, 1996.

[115] A. F. Andreev, "Thermal conductivity of the intermediate state in superconductors," *Soviet Physics-JETP*, vol. 19, pp. 1228–1232, 1964.

[116] G. Blonder, m. M. Tinkham, and k. T. Klapwijk, "Transition from metallic to tunneling regimes in superconducting microconstrictions: Excess current, charge imbalance, and supercurrent conversion," *Physical Review B*, vol. 25, no. 7, p. 4515, 1982.

[117] C. W. J. Beenakker, "Three âĂIJuniversalâĂİ mesoscopic josephson effects," *Transport Phenomena in Mesoscopic Systems*, p. 235âĂŞ253, 1992.

[118] P. De Gennes and E. Guyon, "Superconductivity in" normal" metals," *Phys. Letters*, vol. 3, 1963.

[119] C. W. J. Beenakker and H. van Houten, "Josephson current through a superconducting quantum point contact shorter than the coherence length," *Phys. Rev. Lett.*, vol. 66, pp. 3056–3059, Jun 1991.

[120] A. Zagoskin, *Quantum Theory of Many-Body Systems: Techniques and Applications*. Springer Publishing Company, Incorporated, 2nd ed., 2014.

[121] I. O. Kulik, "Macroscopic Quantization and the Proximity Effect in S-N-S Junctions," *Soviet Journal of Experimental and Theoretical Physics*, vol. 30, p. 944, Jan. 1969.

[122] B. Bujnowski, D. Bercioux, F. Konschelle, J. Cayssol, and F. S. Bergeret, "Andreev spectrum of a josephson junction with spin-split superconductors," *EPL (Europhysics Letters)*, vol. 115, p. 67001, sep 2016.

[123] D. Meschede, *Gerthsen Physik*. Springer, 24. ed., 2010.

[124] C. Kittel and P. McEuen, *Kittel's Introduction to Solid State Physics*. John Wiley & Sons, 2018.

[125] V. V. Ryazanov, V. A. Oboznov, A. S. Prokofiev, V. V. Bolginov, and A. K. Feofanov, "Superconductor—ferromagnet—superconductor -junctions," *Journal of Low Temperature Physics*, vol. 136, pp. 385–400, Sept. 2004.

[126] C. Strunk, C. Sürgers, U. Paschen, and H. v. Löhneysen, "Superconductivity in layered nb/gd films," *Phys. Rev. B*, vol. 49, pp. 4053–4063, Feb 1994.

[127] J. Aarts, J. M. E. Geers, E. Brück, A. A. Golubov, and R. Coehoorn, "Interface transparency of superconductor/ferromagnetic multilayers," *Phys. Rev. B*, vol. 56, pp. 2779–2787, Aug 1997.

[128] Y. V. Fominov, N. M. Chtchelkatchev, and A. A. Golubov, "Nonmonotonic critical temperature in superconductor/ferromagnet bilayers," *Phys. Rev. B*, vol. 66, p. 014507, Jun 2002.

[129] Y. Obi, M. Ikebe, and H. Fujishiro, "Evidence for zero- and π-phase order parameters of superconducting Nb/Co tri- and pentalayers from the oscillatory behavior of the transition temperature," *Phys. Rev. Lett.*, vol. 94, p. 057008, Feb 2005.

[130] S. Oh, Y.-H. Kim, D. Youm, and M. R. Beasley, "Spin-orbit scattering effect on the oscillatory T_c of superconductive/magnetic multilayers," *Phys. Rev. B*, vol. 63, p. 052501, Dec 2000.

[131] Y. Blum, A. Tsukernik, M. Karpovski, and A. Palevski, "Oscillations of the superconducting critical current in nb-cu-ni-cu-nb junctions," *Phys. Rev. Lett.*, vol. 89, p. 187004, Oct 2002.

[132] J. Linder, T. Yokoyama, and A. Sudbø, "Theory of superconducting and magnetic proximity effect in s/f structures with inhomogeneous magnetization textures and spin-active interfaces," *Phys. Rev. B*, vol. 79, p. 054523, Feb 2009.

[133] F. S. Bergeret, A. F. Volkov, and K. B. Efetov, "Josephson current in superconductor-ferromagnet structures with a nonhomogeneous magnetization," *Phys. Rev. B*, vol. 64, p. 134506, Sep 2001.

[134] M. Houzet, "Ferromagnetic josephson junction with precessing magnetization," *Phys. Rev. Lett.*, vol. 101, p. 057009, Aug 2008.

[135] F. S. Bergeret and I. V. Tokatly, "Spin-orbit coupling as a source of long-range triplet proximity effect in superconductor-ferromagnet hybrid structures," *Phys. Rev. B*, vol. 89, p. 134517, Apr 2014.

[136] L. Lepori, D. Giuliano, A. Nava, and C. A. Perroni, "Interplay between singlet and triplet pairings in multiband two-dimensional oxide superconductors," *Phys. Rev. B*, vol. 104, p. 134509, Oct 2021.

[137] V. M. Edelstein, "Triplet superconductivity and magnetoelectric effect near the s-wave-superconductor– normal-metal interface caused by local breaking of mirror symmetry," *Phys. Rev. B*, vol. 67, p. 020505, Jan 2003.

[138] S. Takei and V. Galitski, "Microscopic theory for a ferromagnetic nanowire/superconductor heterostructure: Transport, fluctuations, and topological superconductivity," *Phys. Rev. B*, vol. 86, p. 054521, Aug 2012.

[139] X. Liu, J. K. Jain, and C.-X. Liu, "Long-range spin-triplet helix in proximity induced superconductivity in spin-orbit-coupled systems," *Phys. Rev. Lett.*, vol. 113, p. 227002, Nov 2014.

[140] F. S. Bergeret and I. V. Tokatly, "Singlet-triplet conversion and the long-range proximity effect in superconductor-ferromagnet structures with generic spin dependent fields," *Phys. Rev. Lett.*, vol. 110, p. 117003, Mar 2013.

[141] E. Rashba, "Properties of semiconductors with an extremum loop. cyclotron and combinational resonance in a magnetic field perpendicular to the plane of the loop," *Sov. Phys. Solid. State*, vol. 2, pp. 1109–1122, 1960.

[142] G. Dresselhaus, "Spin-orbit coupling effects in zinc blende structures," *Phys. Rev.*, vol. 100, pp. 580–586, Oct 1955.

[143] J. Linder and A. V. Balatsky, "Odd-frequency superconductivity," *Rev. Mod. Phys.*, vol. 91, p. 045005, Dec 2019.

[144] V. L. Berezinskii, "New model of the anisotropic phase of superfluid he^3," *JETP Lett.*, vol. 20, pp. 287–289, 1974.

[145] A. Balatsky and E. Abrahams, "New class of singlet superconductors which break the time reversal and parity," *Phys. Rev. B*, vol. 45, pp. 13125–13128, Jun 1992.

[146] E. Abrahams, A. Balatsky, D. J. Scalapino, and J. R. Schrieffer, "Properties of odd-gap superconductors," *Phys. Rev. B*, vol. 52, pp. 1271–1278, Jul 1995.

[147] A. J. Leggett, "A theoretical description of the new phases of liquid ^{3}He," *Rev. Mod. Phys.*, vol. 47, pp. 331–414, Apr 1975.

[148] M. Minutillo, R. Capecelatro, and P. Lucignano, "Realization of 0-π states in superconductor/ferromagnetic insulator/superconductor josephson junctions: The role of spin-orbit interaction and lattice impurities," *Phys. Rev. B*, vol. 104, p. 184504, Nov 2021.

[149] L. P. Gor'kov *Sov. Phys. JETP*, vol. 7, no. 505, 1958.

[150] J. Rammer and H. Smith, "Quantum field-theoretical methods in transport theory of metals," *Rev. Mod. Phys.*, vol. 58, pp. 323–359, Apr 1986.

[151] T. Ando, "Quantum point contacts in magnetic fields," *Phys. Rev. B*, vol. 44, pp. 8017–8027, Oct 1991.

[152] S. Datta, *Electronic Transport in Mesoscopic Systems.* Cambridge Studies in Semiconductor Physics and Microelectronic Engineering, Cambridge University Press, 1995.

[153] P. A. Lee and D. S. Fisher, "Anderson localization in two dimensions," *Phys. Rev. Lett.*, vol. 47, pp. 882–885, Sep 1981.

[154] C. H. Lewenkopf and E. R. Mucciolo, "The recursive green's funtion method for graphene," *Journal of Computational Electronics, V. 12*, 2013.

[155] I. Žutić, J. Fabian, and S. Das Sarma, "Spintronics: Fundamentals and applications," *Rev. Mod. Phys.*, vol. 76, pp. 323–410, Apr 2004.

[156] J. W. A. Robinson, S. Piano, G. Burnell, C. Bell, and M. G. Blamire, "Critical current oscillations in strong ferromagnetic π junctions," *Phys. Rev. Lett.*, vol. 97, p. 177003, Oct 2006.

[157] S. M. Frolov, D. J. Van Harlingen, V. A. Oboznov, V. V. Bolginov, and V. V. Ryazanov, "Measurement of the current-phase relation of superconductor/ferromagnet/superconductor π josephson junctions," *Phys. Rev. B*, vol. 70, p. 144505, Oct 2004.

[158] D. Bercioux and P. Lucignano, "Quantum transport in rashba spin–orbit materials: a review," *Reports on Progress in Physics*, vol. 78, p. 106001, sep 2015.

[159] D. Bercioux, M. Governale, V. Cataudella, and V. M. Ramaglia, "Rashba effect in quantum networks," *Phys. Rev. B*, vol. 72, p. 075305, Aug 2005.

[160] C. A. Perroni, D. Bercioux, V. M. Ramaglia, and V. Cataudella, "Rashba quantum wire: exact solution and ballistic transport," *Journal of Physics: Condensed Matter*, vol. 19, p. 186227, Apr. 2007.

[161] I. V. Krive, L. Y. Gorelik, R. I. Shekhter, and M. Jonson, "Chiral symmetry breaking and the josephson current in a ballistic superconductorâĂŞquantum wireâĂŞsuperconductor junction," *Low Temperature Physics*, vol. 30, no. 5, pp. 398–404, 2004.

[162] A. A. Reynoso, G. Usaj, C. A. Balseiro, D. Feinberg, and M. Avignon, "Anomalous josephson current in junctions with spin polarizing quantum point contacts," *Phys. Rev. Lett.*, vol. 101, p. 107001, Sep 2008.

[163] Bergeret, F. S. and Tokatly, I. V., "Theory of diffusive josephson junctions in the presence of spin-orbit coupling," *EPL*, vol. 110, no. 5, p. 57005, 2015.

[164] T. Yokoyama, M. Eto, and Y. V. Nazarov, "Anomalous josephson effect induced by spin-orbit interaction and zeeman effect in semiconductor nanowires," *Phys. Rev. B*, vol. 89, p. 195407, May 2014.

[165] A. Zazunov, R. Egger, T. Jonckheere, and T. Martin, "Anomalous josephson current through a spin-orbit coupled quantum dot," *Phys. Rev. Lett.*, vol. 103, p. 147004, Oct 2009.

[166] M. Alidoust and K. Halterman, "Spontaneous edge accumulation of spin currents in finite-size two-dimensional diffusive spinâĂŞorbit coupledsfsheterostructures," *New Journal of Physics*, vol. 17, p. 033001, Mar 2015.

[167] G. Campagnano, P. Lucignano, D. Giuliano, and A. Tagliacozzo, "Spin–orbit coupling and anomalous josephson effect in nanowires," *Journal of Physics: Condensed Matter*, vol. 27, p. 205301, may 2015.

[168] M. Minutillo, D. Giuliano, P. Lucignano, A. Tagliacozzo, and G. Campagnano, "Anomalous josephson effect in s/so/f/s heterostructures," *Phys. Rev. B*, vol. 98, p. 144510, Oct 2018.

[169] G. Campagnano, P. Lucignano, F. Trani, A. Tagliacozzo, and D. Giuliano, "Anomalous josephson effect in nanowires," in *2017 16th International Superconductive Electronics Conference (ISEC)*, IEEE, June 2017.

[170] M. Alidoust, C. Shen, and I. Zutic, "Cubic spin-orbit coupling and anomalous josephson effect in planar junctions," *Phys. Rev. B*, vol. 103, p. L060503, Feb 2021.

[171] S. Pal and C. Benjamin, "Quantized josephson phase battery," *EPL (Europhysics Letters)*, vol. 126, p. 57002, jul 2019.

[172] A. Brunetti, A. Zazunov, A. Kundu, and R. Egger, "Anomalous josephson current, incipient time-reversal symmetry breaking, and majorana bound states in interacting multilevel dots," *Phys. Rev. B*, vol. 88, p. 144515, Oct 2013.

[173] A. Buzdin, "Direct coupling between magnetism and superconducting current in the josephson φ_0 junction," *Phys. Rev. Lett.*, vol. 101, p. 107005, Sep 2008.

[174] F. Konschelle, I. V. Tokatly, and F. S. Bergeret, "Theory of the spin-galvanic effect and the anomalous phase shift φ_0 in superconductors and josephson junctions with intrinsic spin-orbit coupling," *Phys. Rev. B*, vol. 92, p. 125443, Sep 2015.

[175] K. N. Nesterov, M. Houzet, and J. S. Meyer, "Anomalous josephson effect in semiconducting nanowires as a signature of the topologically nontrivial phase," *Phys. Rev. B*, vol. 93, p. 174502, May 2016.

[176] S. Pal and C. Benjamin, "Tuning the 0 - π josephson junction with a magnetic impurity: Role of tunnel contacts, exchange coupling, e - e interactions and high-spin states," *Scientific Reports*, vol. 8, Mar. 2018.

[177] J.-C. Wang, G.-Q. Zha, and S.-P. Zhou, "$0-\pi$ transitions in mesoscopic josephson junctions with magnetic impurity interlayers," *Physica C: Superconductivity*, vol. 483, pp. 79–81, Dec. 2012.

[178] O. Vavra, S. Gazi, D. S. Golubovic, I. Vavra, J. Derer, J. Verbeeck, G. Van Tendeloo, and V. V. Moshchalkov, "0 and π phase josephson coupling through an insulating barrier with magnetic impurities," *Phys. Rev. B*, vol. 74, p. 020502(R), Jul 2006.

[179] A. M. Black-Schaffer and A. V. Balatsky, "Odd-frequency superconducting pairing in topological insulators," *Phys. Rev. B*, vol. 86, p. 144506, Oct 2012.

[180] J. Cayao, C. Triola, and A. M. Black-Schaffer, "Odd-frequency superconducting pairing in one-dimensional systems," *The European Physical Journal Special Topics*, vol. 229, Feb 2020.

[181] T. Löthman, C. Triola, J. Cayao, and A. M. Black-Schaffer, "Disorder-robust *p*-wave pairing with odd frequency dependence in normal metal-conventional superconductor junctions," 2020.

[182] V. Ambegaokar and A. Baratoff, "Tunneling between superconductors," *Phys. Rev. Lett.*, vol. 10, pp. 486–489, Jun 1963.

[183] E. Goldobin, D. Koelle, R. Kleiner, and A. Buzdin, "Josephson junctions with second harmonic in the current-phase relation: Properties of φ junctions," *Phys. Rev. B*, vol. 76, p. 224523, Dec 2007.

[184] F. Konschelle, J. Cayssol, and A. I. Buzdin, "Nonsinusoidal current-phase relation in strongly ferromagnetic and moderately disordered sfs junctions," *Phys. Rev. B*, vol. 78, p. 134505, Oct 2008.

[185] F. S. Bergeret, A. Verso, and A. F. Volkov, "Spin-polarized josephson and quasiparticle currents in superconducting spin-filter tunnel junctions," *Phys. Rev. B*, vol. 86, p. 060506(R), Aug 2012.

[186] D. Sprungmann, K. Westerholt, H. Zabel, M. Weides, and H. Kohlstedt, "Evidence for triplet superconductivity in josephson junctions with barriers of the ferromagnetic heusler alloy cu_2MnAl," *Phys. Rev. B*, vol. 82, p. 060505, Aug 2010.

[187] J. P. Cascales, Y. Takamura, G. M. Stephen, D. Heiman, F. S. Bergeret, and J. S. Moodera, "Switchable josephson junction based on interfacial exchange field," *Applied Physics Letters*, vol. 114, p. 022601, Jan. 2019.

[188] V. M. Edel'shtein, "Characteristics of the Cooper pairing in two-dimensional noncentrosymmetric electron systems," *Soviet Journal of Experimental and Theoretical Physics*, vol. 68, p. 1244, June 1989.

[189] N. Banerjee, J. A. Ouassou, Y. Zhu, N. A. Stelmashenko, J. Linder, and M. G. Blamire, "Controlling the superconducting transition by spin-orbit coupling," *Phys. Rev. B*, vol. 97, p. 184521, May 2018.

[190] H. G. Ahmad, L. D. Palma, R. Caruso, A. Pal, G. P. Pepe, M. G. Blamire, F. Tafuri, and D. Massarotti, "Critical current suppression in spin-filter josephson junctions," *Journal of Superconductivity and Novel Magnetism*, vol. 33, pp. 3043–3049, July 2020.

[191] A. Pal and M. G. Blamire, "Large interfacial exchange fields in a thick superconducting film coupled to a spin filter tunnel barrier," *Phys. Rev. B 92, 180510(R)*, 2015.

[192] D. Massarotti, A. Pal, G. Rotoli, L. Longobardi, M. G. Blamire, and F. Tafuri, "Macroscopic quantum tunnelling in spin filter ferromagnetic josephson junctions," *Nature Communications*, vol. 6, June 2015.

[193] J. S. Moodera, T. S. Santos, and T. Nagahama, "The phenomena of spin-filter tunnelling," *Journal of Physics: Condensed Matter*, vol. 19, p. 165202, Apr. 2007.

[194] H. G. Ahmad, R. Caruso, A. Pal, G. Rotoli, G. P. Pepe, M. G. Blamire, F. Tafuri, and D. Massarotti, "Electrodynamics of highly spin-polarized tunnel josephson junctions," *Phys. Rev. Applied*, vol. 13, p. 014017, Jan 2020.

[195] O. Madelung and B. Taylor, *Introduction to Solid-State Theory.* Springer Series in Solid-State Sciences, Springer, 1978.

[196] A. und N. D. Mermin, "Solid state physics. von n. w. ashcroft und n. d. mermin holt, rinehart and winston, new york 1976, XXII, 826 seiten, $19, 95," *Physik in unserer Zeit*, vol. 9, no. 1, pp. 33–33, 1978.

[197] L. Litinskii, "The band structure of hexagonal NbN," *Solid State Communications*, vol. 71, pp. 299–305, July 1989.

[198] F. Leuenberger, A. Parge, W. Felsch, K. Fauth, and M. Hessler, "Gdn thin films: Bulk and local electronic and magnetic properties," *Phys. Rev. B*, vol. 72, p. 014427, Jul 2005.

[199] L. E. Marsoner Steinkasserer, B. Paulus, and N. Gaston, "Hybrid density functional calculations of the surface electronic structure of gdn," *Phys. Rev. B*, vol. 91, p. 235148, Jun 2015.

[200] P. Wachter and E. Kaldis, "Magnetic interaction and carrier concentration in GdN and GdN1-xOx," *Solid State Communications*, vol. 34, pp. 241–244, Apr. 1980.

[201] C.-g. Duan, R. F. Sabiryanov, J. Liu, W. N. Mei, P. A. Dowben, and J. R. Hardy, "Strain induced half-metal to semiconductor transition in gdn," *Phys. Rev. Lett.*, vol. 94, p. 237201, Jun 2005.

[202] P. Larson and W. R. L. Lambrecht, "Electronic structure of gd pnictides calculated within the LSDA+U approach," *Phys. Rev. B*, vol. 74, p. 085108, Aug 2006.

[203] A. Manchon, H. C. Koo, J. Nitta, S. M. Frolov, and R. A. Duine, "New perspectives for rashba spin–orbit coupling," *Nature Materials*, vol. 14, pp. 871–882, Aug. 2015.

[204] B. Cullity and C. Graham, *Introduction to Magnetic Materials*. Wiley, 2011.

[205] T. E. Baker, A. Richie-Halford, and A. Bill, "Long range triplet josephson current and 0-πtransitions in tunable domain walls," *New Journal of Physics*, vol. 16, p. 093048, Sept. 2014.

[206] J.-F. Liu, K. S. Chan, and J. Wang, "Tunable 0-π transition by spin precession in josephson junctions," *Applied Physics Letters*, vol. 96, p. 182505, May 2010.

[207] T. Maity, H. J. Trodahl, S. Granville, S. Vézian, F. Natali, and B. J. Ruck, "Magnetoresistance of epitaxial GdN films," *Journal of Applied Physics*, vol. 128, p. 213901, Dec. 2020.